CRANFIELD UNIVERSITY

ANDREW DICKINS

FABRICATION OF MICRO-SCALE FEATURES ON TITANIUM ALLOYS THROUGH MICROMILLING

SCHOOL OF AEROSPACE, TRANSPORT AND MANUFACTURING
Precision Engineering

MRes
Academic Year: 2016 - 2017

Supervisors: Dr Saurav Goel, Dr Claudiu Giusca
April 2018

CRANFIELD UNIVERSITY

SCHOOL OF AEROSPACE, TRANSPORT AND MANUFACTURING
Precision Engineering

MRES

Academic Year 2016 - 2017

ANDREW DICKINS

Fabrication of Micro-scale Features on Titanium Alloys through Micromilling

Supervisors: Dr Saurav Goel, Dr Claudiu Giusca
April 2018

This thesis is submitted in partial fulfilment of the requirements for the degree of MRes in Precision Engineering

ABSTRACT

Structured surfaces are of high interest in the manufacturing world, allowing for functionality to be applied to materials through nothing more than a change in the surface topography or an application of a surface coating. Applications for these surfaces range greatly, including, optical surfaces for antireflective surfaces, thermal structures to assist in heat dispersion and anti-fouling surfaces to reduce organisms from adhering to components. Hydrophobic structures, such as the one that have been examined on the lotus leaf under SEM, generate high droplet contact angles and roll off. The manipulation of surface wettability is of particular interest in areas such as the medical sector for self-cleaning applications or controlling cell adhesion on the surface of an implant.

This work investigates the generation of micron level hydrophobic features on two Titanium alloys, Ti-6Al-4V alpha-beta alloy and Ti-30Nb beta alloy, with the aim of identifying how accurately surface structures can be produced through micromilling as well as experimentally testing how successfully these surfaces function after being fabricated. On each alloy, nine different 5mm x 5mm test pillars are machined using micromilling, half of each pillar is machined with 200μm wide and 30μm deep channels, generating a hydrophobic groove structure, and the other half being flat machined. Across these nine pillars the feedrate, spindle speed, axial depth of cut and tool step over were varied to optimise these parameters in terms of structure generation, channel bottom surface roughness and tool to workpiece interaction in an attempt to determine how effective micromilling is as at structuring the surface of beta Titanium alloys. Tool condition was assessed qualitatively using SEM imaging and an independent assessment was carried out to determine the mechanical properties of the beta Titanium alloy being machined.

Keywords:

Beta Ti, biomedical, hydrophobicity, manufacture, end milling.

ACKNOWLEDGEMENTS

Through the completion of the project and writing of this thesis I have received a great amount of support from many of my peers, all of which have contributed to the completion of my work in varying ways. I would like to express my gratitude to a few individuals in particular who without my work would not have been possible.

First and foremost I would like to extend my thanks to Dr Saurav Goel and Dr Claudiu Giusca who have supervised me throughout the duration of this project. They have provided both technical expertise, valuable opinions, and writing and presentation advice to ensure that I have developed as much as possible both as a professional researcher and as an individual. Their guidance has allowed me to further understand my role throughout this year and has enabled me to better make decisions related my research, allowing me to think more independently and creatively whilst always being there to consult with when needed.

I would like to express my gratitude to Cranfield University for the opportunity to study within the engineering department and for providing financial support through the CDT in Ultraprecision with Cambridge. The CDT has both funded me through my academic needs and personal living expenses throughout the year at Cranfield University and has given me the opportunity to experience professional conferences and industries within the engineering field first hand. These experiences have been an invaluable addition to me going forward with my career.

For their support, expertise and assistance I would like to thank the following people. Christine Kempton, who provided training and gave her time to assist me on the universities SEMs, Dektak profilometer, and X-ray diffractometer on which the majority of my measurements were taken on. John Hedge, for the time dedicated to operating the milling machine on which all of the samples were fabricated, who without none of the experimental work would have been possible. Alan Hueme, whose technical experience and guidance assisted greatly in many decisions made throughout the course of the project. And Quentin Lonne who

gave the training needed to operate the Contact Angle measurement equipment and software, allowing me to test all of the surfaces generated.

To the people I have mentioned, and to the many others who have provided me both professional and personal support during my time studying at Cranfield University I would like to express the deepest of gratitude. Without these people this thesis would not have been possible.

TABLE OF CONTENTS

LIST OF FIGURES

LIST OF TABLES

LIST OF EQUATIONS

LIST OF ABBREVIATIONS

BCC	Body Centred Cubic
EDS	Energy Dispersive X-ray Spectroscopy
ESEM	Environmental Scanning Electron Microscope
HCP	Hexagonal Close Packed
NHS	National Health Service
RPM	Revolutions Per Minute
SEM	Scanning Electron Microscope
XRD	X-ray Diffraction
CA	Contact Angle
ST DEV	Standard Deviation
CMM	Co-ordinate Measuring Machine

LIST OF NOMENCLATURES

Surface Wettability

γ_{ab}	Surface tension between medium a and b
θ	Contact angle
r	Roughness factor
f_s	Surface fraction

Nanoindentation

S	Experimentally measured stiffness
E	Elastic modulus
H	Hardness
v	Poisson’s ratio
A	Indentation area
h	Displacement
P	Load

Milling

DOC	Axial depth of cut
f	Feedrate
v	Spindle speed
MMR	Material removal rate
d	Tool diameter

1 INTRODUCTION

Titanium and its alloys are used in a wide range of engineering fields for many different applications due to preferable mechanical properties such as specific strength and corrosion resistance when compared with other metals such as steels or aluminium. Although popular in the aerospace and medical worlds, Titanium alloys are renowned as being difficult to machine materials due to their high fatigue strength, fracture toughness and low thermal conductivity. Because of this they are used more sparingly in some cases due to high manufacturing costs caused by rapid tool wear in machining (Long & Rack, 1998).

Recent new beta Titanium alloys have been developed and have gained attention in the medical field as they exhibit improved mechanical properties over current Titanium alloys commonly used as well as a higher level of biocompatibility for implants (Nishino, 2003). Although there is little known about the machinability of these alloys to currently implement them cost effectively on a large scale.

This project aims to provide a set of optimised parameters that favours minimal tool wear, surface quality, feature generation and machining time in the micromilling of a beta Titanium alloy to test the machinability of the alloy. This will be conducted through the manufacture of microscale features using Tungsten Carbide end mills. Machining trials have been conducted to generate flat surfaces and grooves to determine how cost effective micromilling can be as a method of processing beta Titanium alloys. The functionality of these surfaces will also be tested in terms of surface wettability with the motivation of biomedical application.

1.1 Motivation

Osteoarthritis affects millions of people throughout the UK (number of people affected by knee or hip arthritis shown in Figure 1.1.A). It impacts joints of those suffering with the condition, causing them to become painful, stiff and often tender or swollen around the affected area as a result of cartilage loss between the associated bones (NICE, 2014). The condition can develop in any joint in the body but is most commonly found to occur in hips, knees and the smaller joints in the hands. In most cases the condition can be easily treated by pain medication

or daily exercises of the joint but in more severe cases of the condition can occur where the patient experiences regular and severe pain in the affected joint. When severe arthritis occurs in high load bearing joints such as the hips or knees this can result in a serious impact on the patient's mobility due to it causing pain when placing weight onto the joint, even from smaller actions such as standing, walking and climbing stairs (NHS, Osteoarthritis, 2016). As the condition develops the joints range of motion can become drastically reduced to the point where surgery is often suggested to either relieve pain and disability in the joint (NICE, 2014).

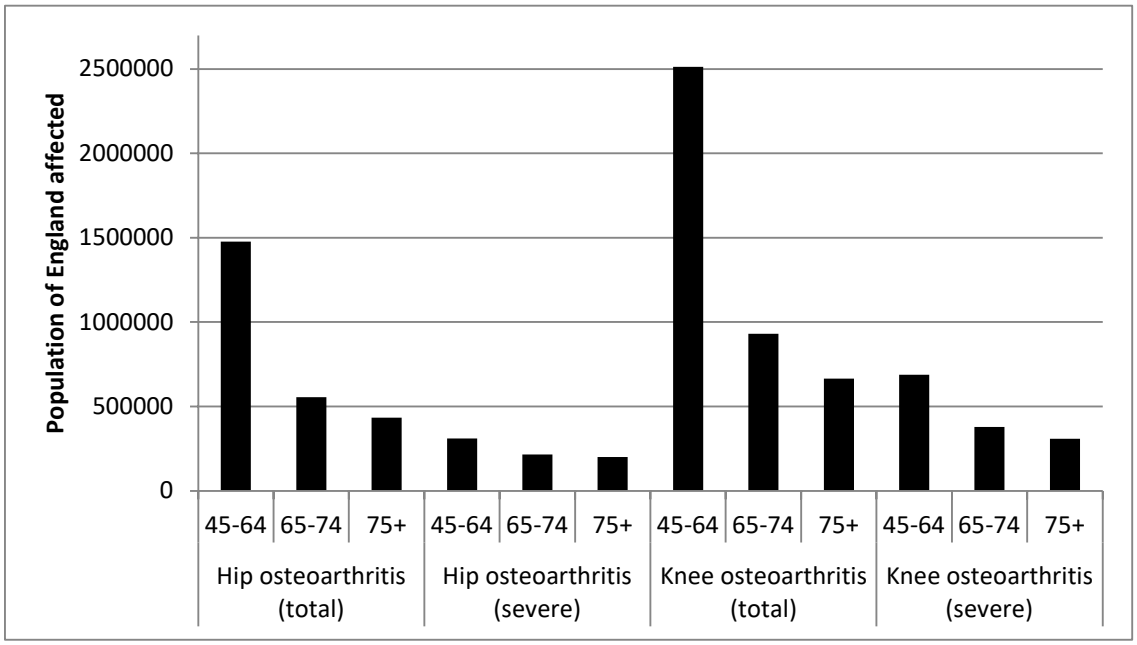

Figure 1.1.A, Data collected by Arthritis Research UK on the number of people in England affected by osteoarthritis (Arthritis Research UK, Musculoskeletal Calculator, n.d.).

The high number of people affected by the condition translates to approximately 160,000 hip and knee replacements being performed across England and Wales each year to treat the condition (NJR, 2014).

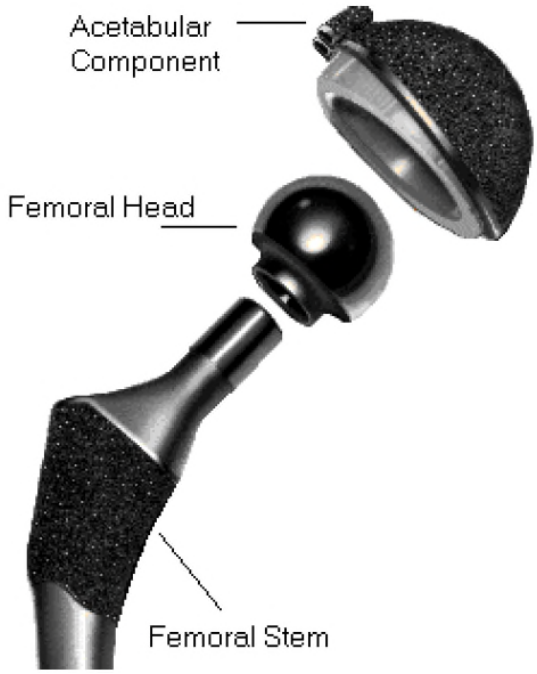

Figure 1.1.B, Labelled image of hip joint components (Zhang, Kiat, & Pramanik, 2009)

As total joint replacement involves a large section of the load bearing bone to be replaced by another material, there are side effects observed that result in the characteristics and properties of the surrounding bone changing over time. This occurs as the stresses and loads usually experienced by the bone change due to the newly implanted artificial joint taking most of the weight (Mamalis, et al., 2006). As the bone surrounding the implant changes from carrying all of the joints load to sharing that load to with the implant (often very unevenly due to mismatches in properties such as elastic modulus between the bone and implant material) the bone adapts as it no longer needs to be strong enough to take the higher weights that it once experienced. This is described by Wolff's Law which states that a reduction of stress on a bone will cause it to reduce its mass, either by thinning of the bone or internally changing structure (Huiskes, Weinans, & Reitbergen, 1992). Stress shielding has been observed in several clinical trials (Engh, Bobyn, & Glassman, 1987; Brodner, et al., 2004; McCarthy, et al., 1991) and bone loss has been reported to be as high at 50% depending on the material of the implant used. This loss of bone mass causes osteoporosis in patients, a

condition which weakens the bones of the body making them more likely to break or fracture (NHS, Osteoporosis , 2016). The condition is most likely to cause injuries such as wrist or hip fracture, making it of great importance that future hip joints minimise the acceleration of osteoporosis in an area of the body already prone to the condition.

Studies researching material properties and their effects on the body when implanted found that there were noticeable decreases in bone resorption when the elastic modulus of the material used was lower (more comparable to the elastic modulus of human bone, being 10-40GPa). This is due to the level bone resorption being heavily related to the stiffness of the implant, which is determined by the elastic modulus and the thickness of the stem. The more flexible the implant, the less bone resorption is observed in the remaining sections of the surrounding bone (Huiskes, Weinans, & Reitbergen, 1992).

In the prosthesis of human joints the most common metal components are fabricated from the alpha-beta Titanium alloy, Ti-6Al-4V. This alloy is used extensively in many fields due to its high corrosion resistance, superior specific strength and greater wear resistance when tested against other alloys previously used such as steels for cobalt chromes (Mamalis, et al., 2006). Although these properties make the alloy favoured over previous materials, there are still issues that need to be addressed. Ti-6Al-4V has an elastic modulus of 110GPa, resulting in stress shielding for long term implants. Although Titanium exhibits exceptional biocompatibility compared to other metals, the alloying elements, Aluminium and Vanadium, have also been observed to have negative biological effects when particles are released into the surrounding tissue from joint wear such as cytotoxicity and advancement of neurological disorders (Wang K. , 1996). Because of these issues there has been a large interest in finding new Titanium alloys with high levels of biocompatibility and lower elastic modulus that can be used as a replacement for Ti-6Al-4V when performing a full joint prosthesis.

Beta Titanium alloys have been suggested by many as a possible solution to this problem due to their alloying elements being less harmful to the body and their body centred cubic structure has been shown to cause lower stiffness without

compromising other properties such as mechanical strength and fatigue life of the metal (Long & Rack, 1998). Although many researchers have looked into the development of these new alloys and testing which elements may be suitable for alloying with Titanium, there is very little current knowledge on the machinability of these materials or how cost effective the manufacturing of components such as implants could potentially be.

1.2 Research Aims

- Develop an optimum matrix to test and improve the machinability of beta titanium alloy, Ti-30Nb, through micromilling.
- Test functionality of structured surfaces introduced by micromilling using tungsten carbide tools.
- Determine how suitable the micromilling of surface structures on beta titanium alloys can be for possible biomedical applications.

1.2.1 Objectives

- Design an array of machining parameters based on previous literature to use in the machining of the Titanium alloys.
- Fabricate hydrophobic features and flat surfaces on Ti-6Al-4V and Ti-30Nb through micromilling with 200µm diameter Tungsten Carbide end mills.
- Perform elemental and structural analysis on the machined surfaces and the tools used both before and after the machining process to determine any chemical interactions between tool and workpiece in the process.
- Perform roughness and form measurements on all machined features to determine the quality of part generated from the micromilling of beta titanium alloys
- Perform contact angle measurements on the substrates and compare the angles of both the flat and structured surfaces machined to determine the degree of hydrophobicity on the fabricated surfaces.

2 LITERATURE REVIEW

2.1 Titanium and Titanium Alloys

Titanium is a transition metal of silver colour with atomic number 22 and an electron configuration of $[Ar]3d^2 4s^2$. The incomplete 3d orbital enables Ti to form solid solutions with many elements, allowing many alloys to be created with Ti as a base element (Long & Rack, 1998).

2.1.1 Properties and Structure

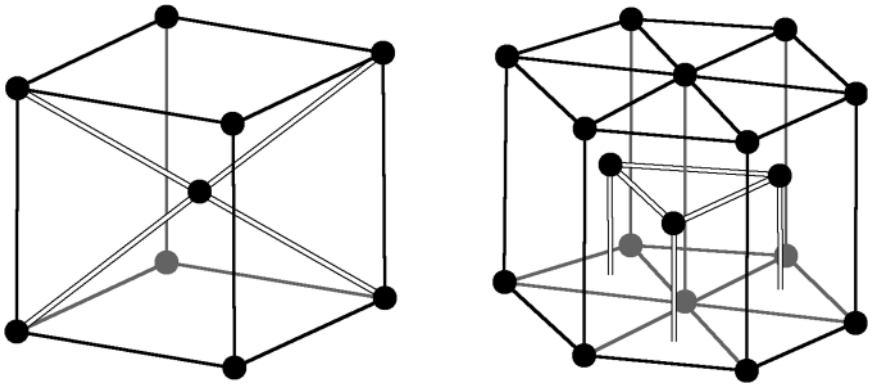

Figure 2.1.A. Crystal structure of Titanium alloys. Left: Beta structure (body centred cubic). Right: alpha structure (hexagonal close packed).

In its elemental form Titanium has a melting point of 1678°C and exhibits a hexagonal closed packed (HCP) crystal (alpha – α) structure when below 882.5°C. When the metal exceeds this temperature its microstructure transitions into a body centred cubic (BCC) crystal (beta – β) structure. This temperature is known as the "beta transus" due to this change in microstructure (Margolin & Farrar, 1969). Through the alloying of Titanium with other elements the transus temperature can be altered and an additional mixed phase (α + β) can be formed where both HCP and BCC structures are present, adding an addition "alpha transus" to the alloy. Elements that cause the transus temperatures to increase are known to be alpha stabilising, whereas elements that reduce the transus temperatures are known to be beta stabilising (Collings, 1984). Metastable beta also exist, which are alloys that retain their beta phase structure after being

quenched from above their beta transus temperature. Examples of both alpha and beta stabilising elements can be seen in Table 2.1.A.

Table 2.1.A. Examples of alpha and beta-stabilising elements when alloyed with Titanium. (Long & Rack, 1998; Kahles, Field, Eylon, & Froes, Machining of Titanium Alloys, 1985).

Alpha-stabilising elements	Beta-stabilising elements
O, Pd, Al	Mo, V, Nb, Ta, Fe, W, Cr, Si, Ni, Co, Mn, H

With this change in transus temperatures comes a change in the physical properties of the material due to the nature of these different Titanium phase structures. Generally, Ti alloys with a higher beta presence (β, metastable β, β + α) have a lower Elastic Modulus than those with a higher alpha presence (α, α + β), yet their Yield and ultimate tensile strength are often of similar magnitudes.

Titanium also exhibits a high specific strength, fracture resistance, heat resistance, biocompatibility and corrosion resistance when compared to other common metals such as steels, Aluminium or Cobalt chrome (Kahles, Field, Eylon, & Froes, Machining of Titanium Alloys, 1985; Gupta & Laubscher, 2016).

Beta titanium exhibits an extremely high tensile strength for a very low elastic modulus when compared to other metallic materials such as steels and even other titanium alloys. It has also been observed as being super elastic in nature, being able to continuously deform without dislocation mechanisms being present (Nishino, 2003).

The properties of Titanium alloys can be manipulated through certain processing methods and heat treatments to tailor them for a specific application. Meta-stable beta Titanium (near Beta Ti alloys) can have their strength and ductility balance to the desire level through the controlling the precipitation of alpha phase in the beta matrix (Kent, Wang, & Dargusch, 2010).

Table 2.1.B. Currently developed titanium alloys and their mechanical properties (Long & Rack, 1998)

Alloy	Microstructure	Elastic Modulus (GPa)	Yield Strength (MPa)	Ultimate Tensile Strength (MPa)
Ti	α	105	692	785
Ti-6Al-4V	α + β	110	850-900	960-970
Ti-6Al-7Nb	α + β	105	921	1024
Ti-5Al-2.5Fe	α + β	110	914	1033
Ti-12Mo-6Zr-2Fe	Metastable β	74-85	1000-1060	1060-1100
Ti-15Mo-5Zr-3Al	Metastable β Aged β + α	75 88-113	870-968 1087-1284	882-975 1099-1312
Ti-15Mo-2.8Nb-3Al	Metastable β Aged β + α	82 100	771 1215	812 1310
Ti-13Nb-13Zr	α' + β	79	900	1030
Ti-15Mo-3Nb-0.3O	Metastable β + silicides	82	1020	1020
Ti-35Nb-5Ta-7Zr	Metastable β	55	530	590
Ti-35Nb-5Ta-7Zr-0.4O	Metastable β	66	976	1010

The stability of the beta phase in Ti alloys is determined by which elements it has been alloyed with. These alloying elements have an effect on the deformation behaviour of the metal (Kent, Wang, & Dargusch, 2010).

Kent, et al. (2010) prepared a sample of Ti-25Nb-3Zr-3Mo-2Sn alloy by hot rolling it at 850°C to a 0.6mm thickness, followed by heat treating it under a protective Argon atmosphere. This sample was then used to test the pseudoelastic behaviour of the beta alloy with an Instron 5584 tensile testing machine. For both a solution treated and a solution treat/aged sample, significant pseudoelastic behaviour was observed, with two stage yielding being present for both. The first yield point was associated with a stress induced transformation from β phase to a martensitic α'' phase. Following this transformation, the second yield was the plastic deformation of the transformed α'' phase. Their findings also determined

that the elastic modulus of the alloy is affected by the heat treatment and prior strain of the alloy and measured this to be between 50GPa and 80GPa, making it comparable with the elastic modulus of human bone.

2.1.2 Applications

Due to the high cost of Titanium, it is mostly only used in components where other alloys do not meet the requirements in terms of mechanical properties. The alloys of Titanium are widely used in industries such as biomedical, aerospace, chemical and shipbuilding where (Kahles, Field, Eylon, & Froes, Machining of Titanium Alloys, 1985; Narutaki, Murakoshi, Motonishi, & Takeyama, 1983).

Most commonly either alpha phase or alpha-beta Titanium alloys are used, although Beta alloys are now gaining significant attention for applications in the automotive, biomedical, sporting, decorative, military and aerospace industries (Nishino, 2003). The Beta alloys properties, such as high specific strength, high corrosion resistance and biocompatibility, makes them suitable to replace alloys such as Ti-6Al-4V that is currently deemed as the preferred alloy in many of these sectors (Kent, Wang, & Dargusch, 2010).

2.1.2.1 Biomedical Applications

In the biomedical industry, Ti-6Al-4V in most common used for metallic implants. This is due its high strength to weight ratio and high wear resistance when compared to other metals such as steels or cobalt chrome alloys. Although it has desirable properties over previously used alloys in load bearing implants, there are still many issues with the use of Ti-6Al-4V for total joint prosthesis. One concern is to do with the biocompatibility of the alloying elements as Aluminium is believed to be carcinogenic and Vanadium has been shown to be cytotoxic (Wang K. , 1996).

As a result of the partial or full bone replacement that takes place in prosthesis such as with hip implants, there are side effects observed that change in the surrounding bone over time. This is caused by the stresses and loads that are usually experienced by the bone now being taken by the implant material instead (Mamalis, et al., 2006). The mismatch in mechanical properties between the

implant material and surrounding bone is what causes this imbalance of stress across the joint known as “stress shielding”. As the bone surrounding the implant is no longer carrying all of the joints load and is now sharing its load with the implant (often very unevenly due to mismatches in properties such as elastic modulus between the bone and implant material) the bone adapts as it no longer needs to be strong enough to take the increased weights it once experiences. This is described by Wolff’s Law which states that a reduction of stress on a bone will cause it to reduce its mass, either by thinning of the bone or internally changing structure (Huiskes, Weinans, & Reitbergen, 1992). Stress shielding has been observed in several clinical trials (Engh, Bobyn, & Glassman, 1987) (Brodner, et al., 2004) (McCarthy, et al., 1991) and bone loss has been reported to be as high at 50% depending on the material of the implant used. This loss of bone mass causes osteoporosis in patients, a condition which weakens the bones of the body making them more likely to break or fracture (NHS, Osteoporosis , 2016). The condition is most likely to cause injuries such as wrist or hip fracture, making it of great importance that future hip joints minimise the acceleration of osteoporosis in an area of the body already prone to the condition.

Studies researching material properties and their effects on the body when implanted found that there were noticeable decreases in bone resorption when the elastic modulus of the material used was lower (more comparable to the elastic modulus of human bone, being 10-40GPa). This is due to the level bone resorption being heavily related to the stiffness of the implant, which is determined by the elastic modulus and the thickness of the stem. The more flexible the femoral stem is, the less bone resorption is observed in the remaining sections of the femur (Huiskes, Weinans, & Reitbergen, 1992). Although the elastic modulus of Ti-6Al-4V is much lower than that of steel and cobalt alloys, it is still relatively high (~110GPa) compared to that of bone so stress shielding effects still occur (Long & Rack, 1998).

Because of this large mismatch in elastic modulus and problematic alloying elements, there is a desire to find an alternative for Ti-6Al-4V in the biomedical industry as an implant material. Beta Titanium alloys have been suggested as a

possible solution as many beta stabilising elements exhibit extremely high levels of biocompatibility and their crystal structure causes a lower elastic modulus, is some cases as low as 55GPa (Long & Rack, 1998), without any compromise in the alloys strength.

2.2 Machinability of Titanium

When discussing the machinability of a material, an important focus is not only whether or not the material can be produced to a specific standard of quality, but also the costs involved to achieve this standard. In the case of micromachining, the main factor that affects the cost of the manufacturing process is usually tool life. This is due to the wear induced on the tool by the machining process requiring frequent tool replacements if it is too high, which can become extremely expensive if the wear is occurring rapidly. Generally speaking, if the tool must be replaced so frequently to achieve desired quality that the cost of tools outweighs the value of the component being manufactured, the material is deemed not machinable for the component in question.

Although extensively used in a wide range of fields, Titanium is notoriously known to be a difficult material to machine cost effectively. The high fatigue strength exhibited by Titanium alloys and the elements high chemical affinity to Carbon cause rapid tool wear, especially in diamond tools which are commonly used for other difficult to machine materials. Titanium alloys are known to be poor conductors of heat, resulting in very high local temperatures between the tool edge and substrate due to friction. These high local temperatures result in an increased amount of chemical reaction between the tool and workpiece, furthering the ineffectiveness of Carbon based tools. The low elastic modulus of the alloys compared to materials such as steel can also result in chatter, deflection and rubbing issues during the machining process. For these reasons, diamond tools are not deemed to be cost effective in the manufacturing of titanium alloy components (Machado & Wallbank, 1990).

Because of these factors, extensive research has been carried out in the machining of Titanium and its alloys to optimise machining parameters, methods and tool compositions in an attempt to make use of the material as cost effective

as possible (Kahles, Field, Eylon, & Froes, Machining of Titanium Alloys, 1985; Narutaki & Murakoshi, Study on Machining of Titanium Alloys, 1983; Dandekar, Shin, & Barnes, 2010). These studies include all methods of machining including drilling (Cantero, Tardio, Canteli, Marcos, & Miguelez, 2005; Li, Riester, Watkins, Blau, & Shih, 2008), turning (Muhammad, et al., 2014; Jasinevicius, 2007), laser polishing (Perry, Werschmoeller, Li, Pfefferkorn, & Duffie, 2009) and milling (Sun & Guo, 2009; Zhang, Li, & Jiang, 2010; Li, Zhao, Luo, & Pei, 2012; Jawaid, Sharif, & Koksal, 2000).

The majority of current studies carried out have been performed on either pure Titanium, alpha Titanium alloys, or alpha-beta Titanium alloys, with Ti-6Al-4V being most commonly studied due to its widespread use compared to other Titanium alloys. As pure beta Titanium alloys are still relatively new and therefore not as commonly used, there is less machining literature available, although studies have been conducted on some beta alloys (Rashid, Sun, Wang, & Dargusch, Machinability of a Near Beta Titanium Alloy, 2011; The Effect of Laser Power on the Machinability of the Ti-6Cr-5Mo-5V-4Al Beta Titanium Alloy During Laser Assisted Machining, 2012; An Investigation of Cutting Forces and Cutting Temperatures During Laser-Assisted Machining of the Ti-6Cr-5Mo-5V-4Al Beta Titanium Alloy, 2012; Xi, et al., 2014). These studies have been conducted on a limited number of beta alloys compared to the number that have been suggested as potential replacements for existing alloys and generally conclude that beta alloys are more difficult to machine that others due to a higher specific strength and fracture toughness with the change in microstructure.

2.2.1 Cutting Tool Wear

Tool wear occurs during the machining process due to chemical, mechanic and thermal interactions between the tool and the workpiece that result in material also being removed from the tool, generally at a much lower rate that the workpiece. This is because, although the materials of tools are chosen to have high hardness and strength, they are not indestructible and will experience damage through extensive use. The wear of tools occurs mostly around the cutting edge where the most contact is made with the workpiece, and from this

point extends to the face either side of the cutting edge, known as the cutting or rake face and flank face. The wear amount can have a larger impact on the quality of surface that can be generated by the tool as it directly impacts the effective sharpness. As the wear volume increases and the tool becomes blunt, the surface roughness will generally increase, and form accuracy decrease (Durazo-Cardenas, et al., 2007).

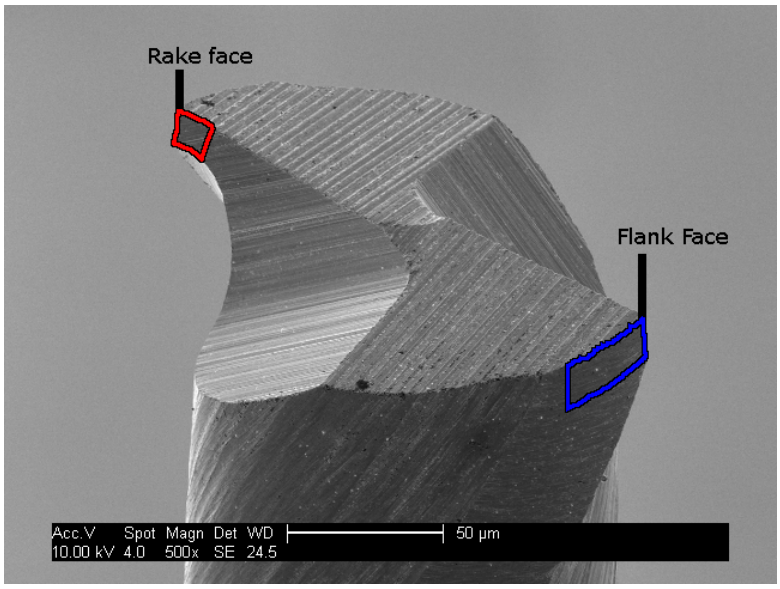

Figure 2.2.A. SEM image of an unused two flute 200µm diameter Tungsten Carbide end mill. Marked are the rake face (in red) and the flank face (in blue). These are the two areas that experience the highest levels of wear on the cutting tool and are divided by the cutting edge. As the cutting edge wears the cutting radius is reduced, making the tool blunter.

In milling the level of tool wear observed can be dependent on the number of flutes the tool has, as these effectively share the work between them. The more flutes present, in theory, the less wear on each flutes for the same amount of machining. This is a large difference from systems such a turning machines where a single cutting insert is used for all the machining done, but does provide an extra point of failure also. For example, if one of two flutes experiences some critical damage, then although the remaining flute is still in a relatively good condition, the tool will likely need to be replaced as it will then be experiencing twice the load that it was prior to the other flutes failure, and this is likely to result

in the quality of machined surface being reduced considerably. Tool wear in micromilling can occur through a variety of mechanisms. Commonly observed phenomena that affect the tools condition include delamination, adhesion, attrition, diffusion, plastic deformation and thermal cracking.

Delamination of tool coating results in increases tool wear from the tools underlying materials coming into direct contact with the work piece where the coating was previously applied as a means of prolonging the tools life. This can be especially prevalent if the coating applied is not designed to machine the substrate material (Attanasio, Gelfi, Ceretti, & Giardini, 2013; Su, He, Li, & Li, 2006).

Adhesion also results in a built up edge, where work piece material becomes attached to the cutting face. This causes issues as the tool's cutting edge is no longer the first point of contact between the tool and workpiece, causing the cutting forces to change (Attanasio, Gelfi, Ceretti, & Giardini, 2013). Adhesion can be described as a "welding" of the workpiece material to the rake and flank faces of the tool and is most likely to occur after the delamination of the tools coating and what follows is a compressing of adhered material as is collides with the substrate with each re-entry to the workpiece. This can initiate chipping in the tool itself and results in breakage at the cutting edge (Konig, Fritsch, & Kammermeier, 1991; Su, He, Li, & Li, 2006).

Attrition is described as the removal of tool material grains by adherent chips or the workpiece and is commonly indicated by an uneven level of wear across the flank face. These uneven sections are evidence that sections of the tool have been pulled away by the adherent workpiece material on impact. Damage as a result of attrition has been demonstrated to increase with machining time due to the previously chipped surfaces of the tool being more likely to further chip again (Jawaid, Sharif, & Koksal, 2000).

Diffusion occurs as a result of high thermal activity between the workpiece and tool which causes chemical diffusion of the tools material. This is especially prevalent in situations such as Titanium machining with Carbon based cutting inserts such as diamond. Diffusion wear is the most dominant mechanism of wear

in this situation and in the reason that diamond is not a viable tool choice in the machining of Titanium. Signs of diffusion can be seen through EDS analysis of both the tools built up edge and the machined workpiece where elements from the tool may be found present in the workpiece material (Jawaid, Sharif, & Koksal, 2000; Su, He, Li, & Li, 2006).

High local compressive stressed form the machining process causes plastic deformation of the tools cutting edge which reduces the tools sharpness. In plastic deformation the tool does not lose material in the same way as the other mechanisms discussed, but rather the shape of the tool tip itself is changed permanently due to the high forces it undergoes, but the same amount of material still remains. This phenomenon is found to be more severe at higher cutting speeds and can also be influenced by both the materials of the tool and workpiece and the average grain size. Generally it is found that a larger relative grain size will result in increased plastic deformation (Dearnley & Grearson, 1986). The alteration of the tools geometry from plastic deformation can result in excessive rubbing. Deformation is increased further by in situations where the workpiece maintains a high strength at high temperature and the interruptive nature of the milling process as the separate flutes take turns to clear material (Jawaid, Sharif, & Koksal, 2000).

Poor thermal conductivity of a workpiece and coating delamination can often result in micro-cracking of the tool from induced thermal stresses. These micro-cracks significantly weaken the tool, making failure and chipping more likely to occur. The propagation of these cracks can result in damage beyond just the surface interacting with the workpiece which can cause catastrophic failure of the tool (Jawaid, Sharif, & Koksal, 2000; Su, He, Li, & Li, 2006).

2.2.2 Micromilling of Titanium

The definition of micromilling as a method of machining varies form study to study, but it is generally accepted as milling processes that use tools that have a diameter of less than 0.5mm (Ozel, Thepsonthi, Ulutan, & Kaftanoglu, Experiments and Finite Element Simulations on Micro-milling of Ti-6Al-4V Alloy

with Uncoated and CBN Coated Micro-tools, 2011), although some research include diameters up to 1.5mm under the name.

Shelton and Shin (Comparative Evaluation of Laser-Assisted Micro-milling for AISI 316, AISI 422, Ti-6Al-4V and Iconel 718 in a side-cutting configuration, 2010) performed side cutting experiments on AISI 316, AIDI 422, Ti-6Al-4V and Inconel 718 alloys to compare the machinability of each through micromilling against each other using laser assisted machining. 300μm diameter end mills machined using axial depth of cuts of 150μm and 250μm. This study found that laser assisted machining gave minimal improvement in tool wear compared to conventional machining but a larger reduction in burr size was observed.

Ding et al. (Thermal and Mechanical Modelign Analysis of Laser-Assisted Micro-milling of Difficult-to-Machine Alloys, 2012) modelled the thermal and mechanical characteristics of laser assisted micromilling of a range of materials including Ti-6Al-4V. In this the power of laser was varied to test the substrate temperature changes in use with 100μm and 300μm diameter tungsten carbide tools. This work concluded that laser assisted machine can reduce the amount of built up edge on the tool generated from the milling process on difficult to machine materials.

Thepsonthi and Ozel (Multi-objective Process Optimization for Micro-end Milling of Ti-6Al-4V Titanium Alloy, 2012) analysed the size of top burrs formed in the micromilling of slots and surface roughness of machined surface to optimise machining parameters. Using 635μm diameter tools it was found that axial depth of cut is the largest contributing parameter in the formation of top burrs, whereas feed per tooth had the largest influence of surface roughness in the bottom of the slots machined.

Figure 2.2.B show plots of differ feed rates, depths of cut and spindle speeds that have been used over these studies and others (Bajpai, Kushwaha, & Singh, 2013; Thepsonthi & Ozel, Experimental and Finite Element Simulation Based Investigations on Micro-milling Ti-6Al-4V Titanium Alloy: Effects of cBN Coating on Tool Wear, 2013; Ozel, Thepsonthi, Ulutan, & Kaftanoglu, Experimental and Finite Element Simulation on Micro-milling of Ti-6Al-4V Alloy with Uncoated and

cBN Coated Micro-tools, 2011; Attanasio, Gelfi, Ceretti, & Giardini, 2013) when micromilling titanium alloys with the associated tool diameters. From these graphs it can be see than general a lower feed rate and depth of cut is preferred for the small diameter tools, but a higher spindle speed.

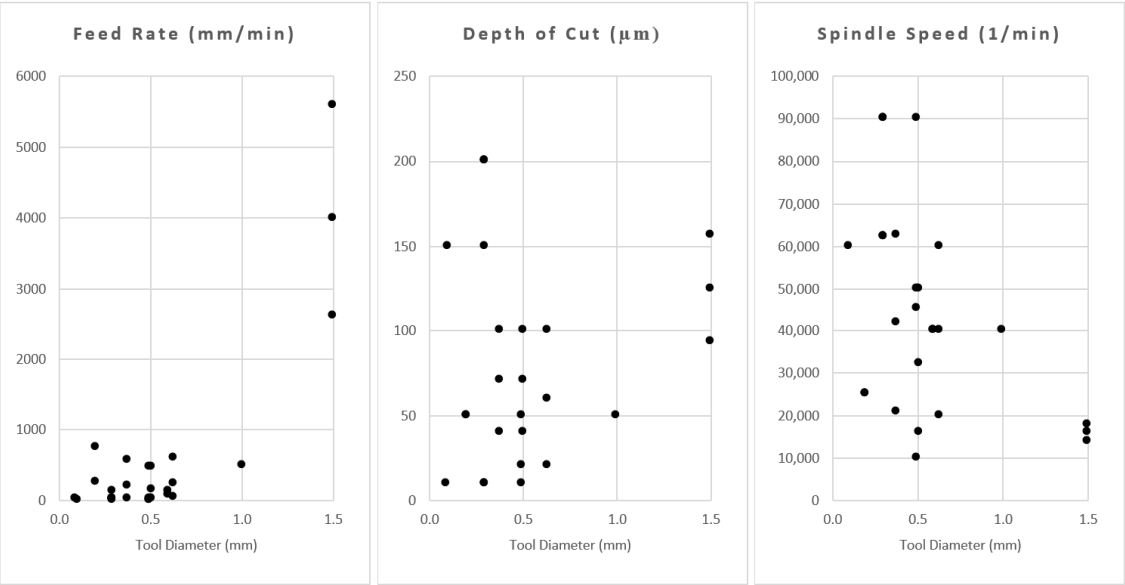

Figure 2.2.B. Milling parameters used over various different experimental and computer modelling studies performed on the micromilling of Titanium alloys.

2.3 Surface Functionality

The topography of an objects surface can have a large impact on how effectively it performs its designed function. In the world of manufacturing and engineering surface modifications range from nano structures to macro size features and come in a range of every day products, including structured tyre patterns to improve grip on the road, waterproofing on clothing or self-cleaning glass, and golf ball dimples to improve aerodynamics. Modifications such as these have been applied in many fields including to change properties that are optical, chemical, mechanical, and thermal across all fields of engineering (Evans & Bryan, 1999).

Many of these surfaces are inspired by observations made in nature. Evolution has perfected many surfaces over millions of year to assist in the survival of many species of plants and animals, and this has been the perfect place to begin when

designing a surface to have a specific function (Malshe, et al., 2013). A strong example of this comes from the gecko, a small lizard capable of climbing many surfaces through dry contact. The lizard is capable of doing this thanks to the thousands of nano scale hairs on the end of each limb. These structures allow for dry adhesion through Van de Waals forces and have been replicated by engineers in the development of “gecko tape,” a type of tape that can stick objects together without a wet adhesive. These long hair structures also allow for adhesion on rough, un-uniform surfaces as each hair can independently flex to fit the space available (Kamperman, Kroner, Campo, McMeeking, & Arzt, 2010).

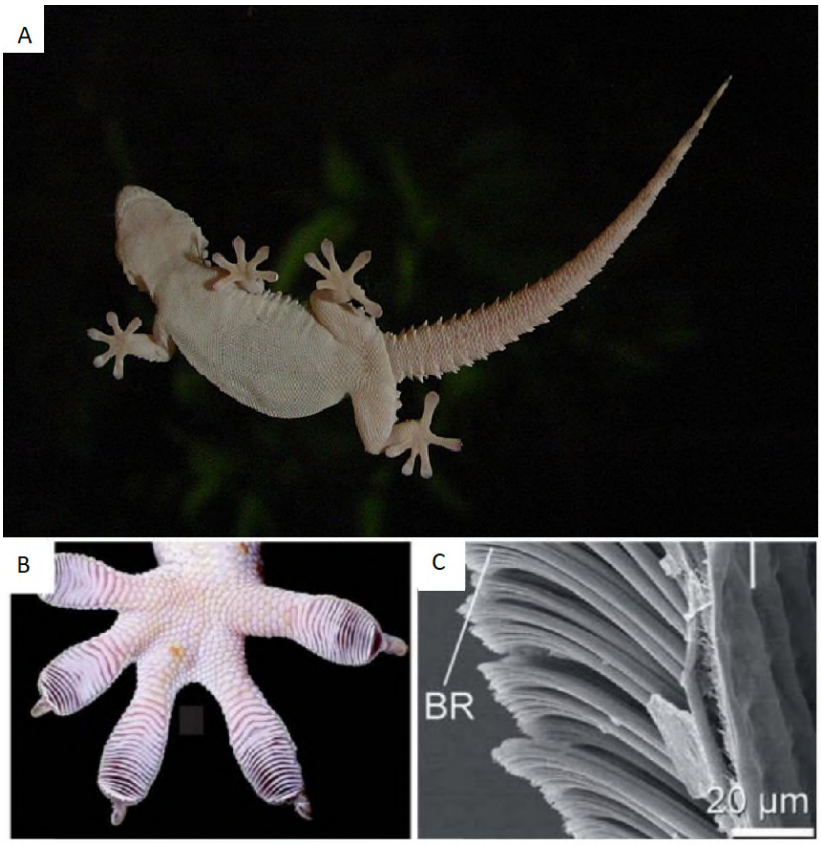

Figure 2.3.A. Images of a gecko. A) Gecko walking on a glass window. B) Magnified image of a gecko’s foot. C) SEM image of the hairs present on a Gecko’s foot that allow for dry adhesion when climbing (Kamperman, Kroner, Campo, McMeeking, & Arzt, 2010).

Inspiration has also been taken in surface design from the anti-fouling properties of shark skin which prevent microbes from adhering to the shark as well as

providing improved hydrodynamics, allowing the shark to swim easier (Malshe, et al., 2013). This phenomenon has also been observed in many other aquatic organisms such as Mussels and Crabs and has be replicated to create artificial anti-foaling surfaces that are both highly effective and non-toxic as they rely more on the surface topography rather than just the chemical interactions that may cause harm to organisms attempting to adhere to the surface (Magin, Cooper, & Brennan, 2010).

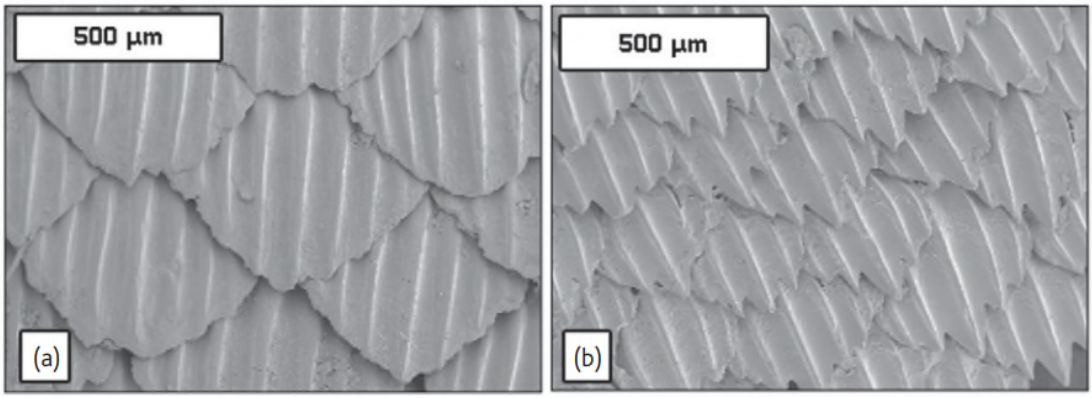

Figure 2.3.B. SEM images of shark skin which granted anti-fouling properties and increase hydrodynamics for swimming. A) Spinner shark skin. B) Galapagos shark skin (Magin, Cooper, & Brennan, 2010).

Other areas where engineers have taken inspiration in surface manipulation from nature include improved hydrodynamics from fish scales, improved cutting tool strength from the teeth of animals, self-cleaning surfaces from plant leaves and colour manipulation from chameleons and butterfly wings (Malshe, et al., 2013). Modern components are commonly designed beyond the simple macro-scale geometry that they have. Manufacturers and researchers alike have a large focus on how surfaces interact with their surroundings and how they can be manipulated to ensure maximum efficiency and performance. If modified correctly, then a surface's functionality can be varied to increase the quality of product for a range of applications (Bruzzone, Costa, Lonardo, & Lucca, 2008).

2.3.1 Surface Wettability

The surface wettability of a surface is define by how easily the surface in question can spread a liquid, and is dependent on the surface free energy of the substrate, the liquid and the atmosphere surrounding them. The level of wettability is measured commonly by contact angle measurements, where a droplet of the liquid is placed onto a sample and the angle between the liquid-atmosphere interface and the liquid-surface interface is measured. In general terms, a contact angle less than 90° is defined as a hydrophilic response, and a contact angle greater than 90° is hydrophobic. A hydrophilic surface will easily have a liquid spread over it and there will be a level of adherence, whereas on hydrophobic surfaces small liquid droplets will occur that can roll off from the surface with ease (Shirtcliffe, McHale, Arterton, & Newton, 2010).

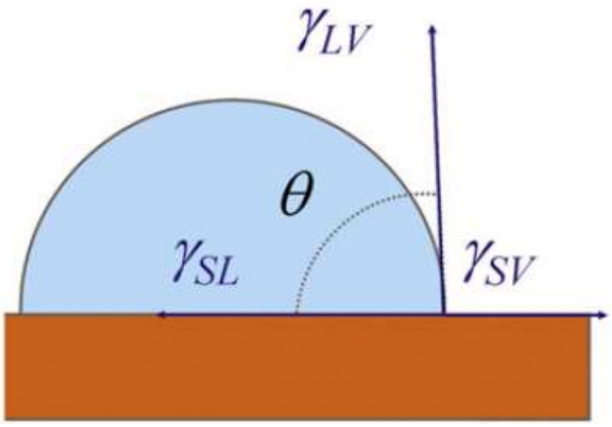

Figure 2.3.C. Diagram showing the forces at the three-phase contact line of a liquid droplet on a solid (Shirtcliffe, McHale, Arterton, & Newton, 2010).

Contact angles can be calculated as a function of the three substances surface free energies through Young's equation:

$$\gamma_{SL} + \gamma_{LV} cos\theta_e = \gamma_{SV}$$

Eq. 1

This equation can be described as a balancing of the forces present along the three different interfaces. This approach assumes a perfectly smooth solid surface when in reality other factors begin to take such as surface roughness.

Generally there are two well-known and accepted models for how water interacts with a rough surface, the Cassie-Baxter model and the Wenzel model. (Shirtcliffe, McHale, Arterton, & Newton, 2010).

Wenzel (Restistance of Solid Surfaces to Wetting by Water, 1936) proposed a model in which the liquid droplet will be in contact with the entire rough surface area beneath it, giving a very large interfacial contact area. In this situation a roughness factor, r, is introduced in the calculation of contact angle that is a factor between the total rough surface area and the area if the surface was completely flat. In this situation the following formula applies:

$$\cos\theta_W = \frac{r(\gamma_{SL} - \gamma_{SV})}{\gamma_{LV}}$$

Eq. 2

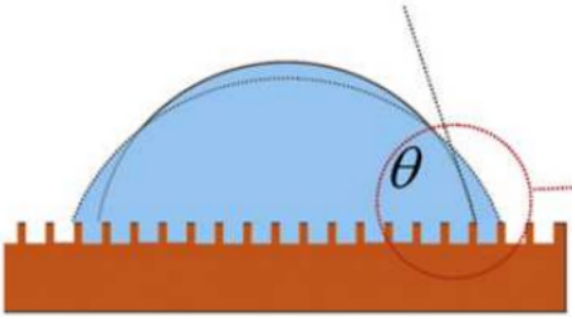

Figure 2.3.D. Diagram of Wenzel model for a droplet's interaction with a rough surface (Shirtcliffe, McHale, Arterton, & Newton, 2010).

Cassie & Baxter (Wettability of Porous Surfaces, 1944) proposed a model in which the droplet does not have complete contact with the surface, but rather there are gaps between the spikes and trenches of the rough surface where air is present, breaking contact. In this instance the true contact surface is a fraction, f_s, of the apparent surface, and the following approximation holds true:

$$\cos\theta_{CB} = \frac{f_s(\gamma_{SL} - \gamma_{SV})}{\gamma_{LV}} - (1 - f_s)$$

Eq. 3

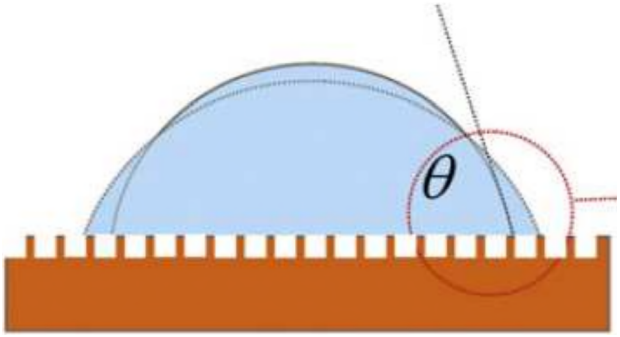

Figure 2.3.E. Diagram of Cassie-Baxter model for a droplet's interaction with a rough surface (Shirtcliffe, McHale, Arterton, & Newton, 2010).

Inspiration for wettability control of surfaces comes mostly from the Lotus leaf, which is covered is nanoscale pillars causing super-hydrophobicity which results in surface of the leaf self-cleaning. This self-cleaning property is observed in leaves of many plants in the world with many of them exhibiting different surface structures such as trichomes, cuticular folds and wax crystalloids, all to achieve the same result. The self-cleaning phenomenon allows for the plants to absorb larger amounts of light for photosynthesis as it reduces the amount of dust and dirt building up on the leaves (Barthlott & Neinhuis, 1997). Lotus leaves are particularly interesting to many researchers due to the high degree of hydrophobicity that they have, often referred to as “super-hydrophobicity.” The contact angles of water when observed on a lotus leaf can be as high as 160° (Bico, Marzolin, & Quere, 1999). This is due to a series of nanoscale pillars on the leaf’s surface that greatly reduce the contact area with the droplet.

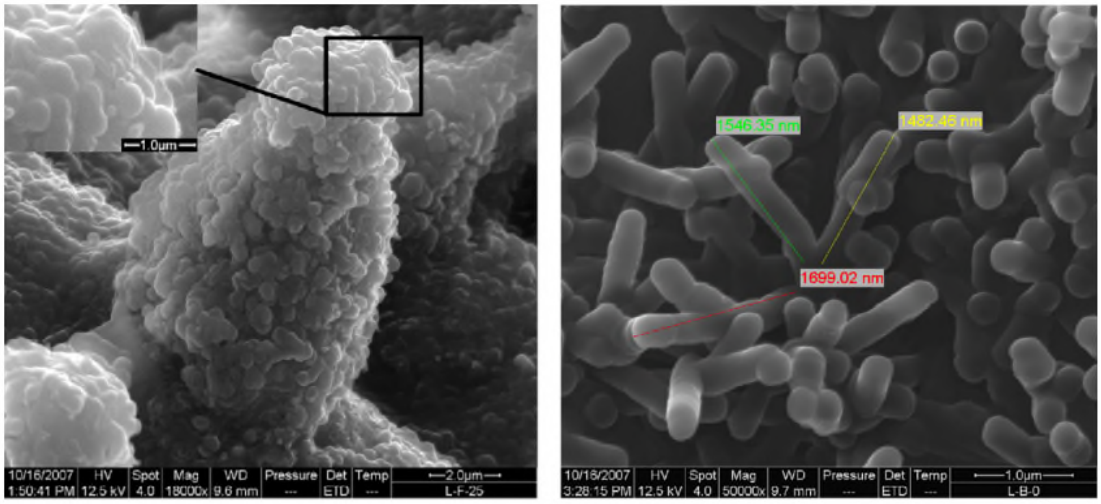

Figure 2.3.F. SEM images taken of the nanometre surface structure of the lotus leaf showing the surface structure of each micro-pillar at high magnification (left) and the project lengths of the pillars themselves (right) (Wang, Chen, Sui, Li, & Chen, 2009)

Duck feathers also show hydrophobic behaviour due to the thousands of sub-microscale hairs and thin oil layer present that cause water to easily roll off the duck's wings and breast. This alloys the duck to take flight directly from the surface of a pond without being weighed down by water trapped within its feathers (Liu, Chen, & Xin, 2008).

In the world of engineering these principles have been applied to a large variety of different purposes, including adhesion manipulation, anticorrosion, wear resistance, biocompatibility, water proofing and self-cleaning surfaces (Fai, Zhongchen, & Ting, 2017).

2.3.2 Structured Titanium Surfaces

The design and structuring of Titanium surfaces has been discussed in medical literature extensively, with a large focus on properties such as cell response and adhesion in medical implants. These commonly focus on manipulating the alloys surfaces wettability through surface roughness and micro-structuring.

Deligianni et al. (Effect of Surface Roughness of the Titanium Alloy Ti-6Al-4V on Human Bone Marrow Cell Response and on Protein Adsorprtion, 2001)

investigated how surface roughness of Ti-6Al-4V can have an impact of the cell response of bone marrow and protein adsorption. From these studies they found that rough surfaces encourage bone cell cultivation much more successfully that smooth surfaces will, meaning that as bone regrows around an implant, it would bind better to a rough implant surface.

Ponsennet et al. (Ponsonnet, et al., 2003) performed cell adhesion tests on a Nickel-Titanium alloy, commercially pure Ti, and Ti-6Al-4V with ranging surface roughness values. Contact angles were measured on these samples ranging from 36° to 80° after the droplet was left to rest for 35 seconds. It was found that the highest roughness values exhibited the largest contact angles, thus being the most hydrophobic surfaces. It was concluded that surface free energy is one of the most influential factors in cell adhesion, and that this adhesion can be manipulated through changes in roughness.

Elias et al. (Relationship Between Surfaces Properties (Roughness, Wettability and Morphology) of Titanium and Dental Implant Removal Torque, 2007), Rupp et al. (Roughness induced Dyanamic Changes of Wettability of Acid Etched Titanium Implant Modifications, 2004), Park et al. (Enhancement of Surface Wettability via the Modification of Microtextured Titanium Implant Surfaces with Polyelectrolytes, 2011) and Dahotre et al. (Wetting Behaviour of Laser Synthetic Surface Microtextures on Ti-6Al-4V for Bioapplication, 2010) also performed studies focussing on the relationship between surface roughness, micro-structuring, wettability and cell cultivation for Titanium implants such as bone replacement or dental implantation. All of these studied concluded that the surface morphology can greatly influence how the implant will interact with the host's cell, with higher wettability resulting in a greater cell adhesion and quicker healing times around the area of implant.

2.4 Knowledge gaps in the literature

In the literature there is a large focus on the machining of currently commercial Titanium alloys, with extensive research being performed on the alloy Ti-6Al-4V for a wide variety of machining methods and applications. Although there is extensive literature discussing the potential use of beta Titanium alloys,

especially for applications such as biomedical implants, there is very little information readily available about how easily beta alloys can be machined and processed. Current literature based on beta titanium alloys focusses on the alloying process of the beta stabilising elements and how their mechanical properties vary with various procedures such as heat treating and annealing, but no literature found has covered the fabrication and functional testing of components using these alloys. If beta Titanium alloys are to be utilised in the way many have hypothesised due to their superior mechanical properties, then more must be known about how well these materials can be machined, whether they are cost effective for the suggested applications, and how well components function when manufactured with a beta titanium alloy when compared to currently used materials.

In Micromilling many researchers study the generation of small grooves or side cuts on alloys such as Ti-6Al-4V, but very little research covers micromilling beyond this small level of machining. Wear mechanisms in micromilling, surface quality from single pass milling processes and capability of Ti-6Al-4V milling has been well established in the literature, but no papers discuss the application of micromilling in developing structured surfaces that require longer machining times and how viable the process is for small scale feature manufacture in Titanium alloys, both in terms of tool wear and cost effectiveness and process time for the quality of part produced.

2.4.1 Research Questions

- Can the beta Titanium alloy, Ti-30Nb, be machined cost effectively using tungsten carbide end mills in terms of tool wear and processing times?

- Can micromilling be used as a viable process to generate functional surface structures titanium alloys when compared with other processes?

- Are there any significant chemical interactions when machining Ti-30Nb that could deem the alloy not ideal for biomedical applications?

3 NANOINDENTATION

Prior to the beginning of this project the beta-Titanium alloy, Ti-30Nb, was examined through Nanoindentation to determine the mechanical properties of the material. All data was collected using a Nanoindenter XP.

Tip Information:

Name	Value
Tip Geometry	Berkovich
Area Coefficient 1	2.85
Area Coefficient 2	1

Calculation Inputs:

Name	Value	Units
Frame Stiffness Correction	0	N/m
Percent Unload In Stiffness Calculation	50	%
Perform Drift Correction	1	
Poissons Ratio	0.33	

Test Inputs:

Name	Value	Units
Allowable Drift Rate	0.1	nm/s
Load Rate Multiple For Unload Rate	1	
Peak Load	500	mN
Indent Depth	2000	nm
Number Of Times To Load	5	

Peak Hold Time	10	s
Percent To Unload	90	%
Time To Load	30	s

3.1 Introduction to Nano-indentation

Nanoindentation was initially proposed by Oliver and Pharr (1992) as an improved method of indentation capable of measuring the hardness and elastic modulus of a material through the analysis of load and displacement data obtained when probing a material. The method builds on previous work on macro or micro indentation where it was often found that the area of indent was too large and tip shapes were too varied, resulting is errors. Oliver and Pharr performed indentation with a much smaller Berkovich indenter using small loads to create the indents. The method requires the properties of the indenter being used to be known prior to the experiments so that any elastic deformation from the indenter can be accounted for in the analysis.

To perform nanoindentation, the probe tip is pressed into the surface of the material and both the load and displacement of the tip are recorded for both indentation and the release of the probe. This provides a plot with two curves, one for loading and one for unloading, as can be seen in Figure 3.1.A. From this plot the experimentally measured stiffness, S, can be calculated by taking the gradient of the unloading curve in the initial stages of unloading.

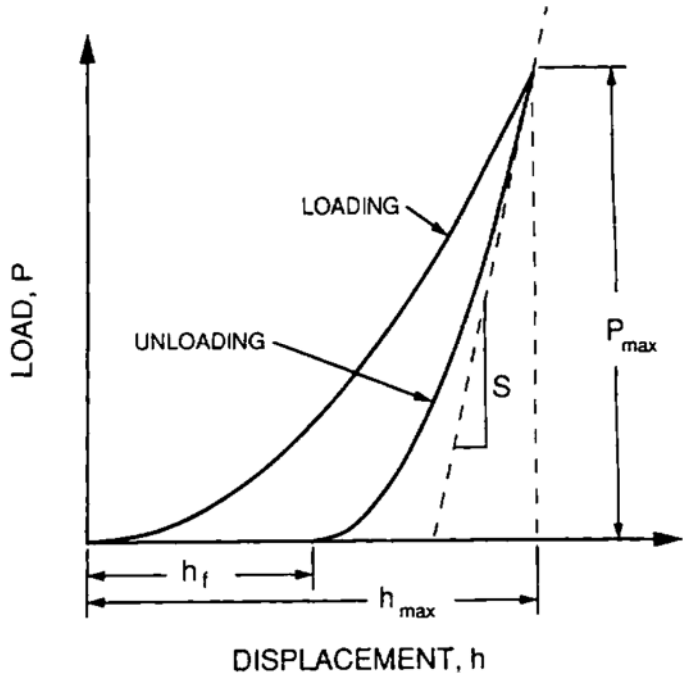

Figure 3.1.A, Example of nanoindentation load vs displacement graph (Oliver & Pharr, 1992).

If the area of indentation, A, is known for an indent, then it's possible to calculate both the Hardness, H, of the material and the reduced modulus, E_r, by using the following equations.

$$E_r = \frac{S\sqrt{\pi}}{2\sqrt{A}}$$

Eq. 4

$$H = \frac{P_{max}}{A}$$

Eq. 5

Non rigid indenters have a contribution to E_r due to the indenter also compressing partly during the loading period. This can be factored out if the modulus of the

indenter, E_i and Poisson's ratio, v, of both the indenter and the material under test using the following equation.

$$\frac{\mathbf{1}}{\boldsymbol{E_r}} = \frac{(\mathbf{1} - \boldsymbol{v^2})}{\boldsymbol{E}} + \frac{\left(\mathbf{1} - \boldsymbol{v_i^2}\right)}{\boldsymbol{E_i}}$$

Eq. 6

Where E is the elastic modulus of the material being examined. The area in these indentations were traditionally estimated through optical methods based on the surface of the material post measurement. Although the area of indentation can be described by an area function that relates the cross-sectional area of the probe to the contact depth, h_c.

$$\boldsymbol{A} = \boldsymbol{F}(\boldsymbol{h_c})$$

Eq. 7

In which F is a functional form dependent on the geometry of the indenter. For a Berkovich tip (shown in Figure 3.1.A), both used in Oliver and Pharr's research

and in the preliminary examination of the Ti-30Nb, has the following form function (Fischer-Cripps, 2009).

$$A = 3\sqrt{3}h_c^2 \tan^2 \theta$$

Eq. 8

Where θ is the angle of the indenter's tip (65.27° for Berkovich tip).

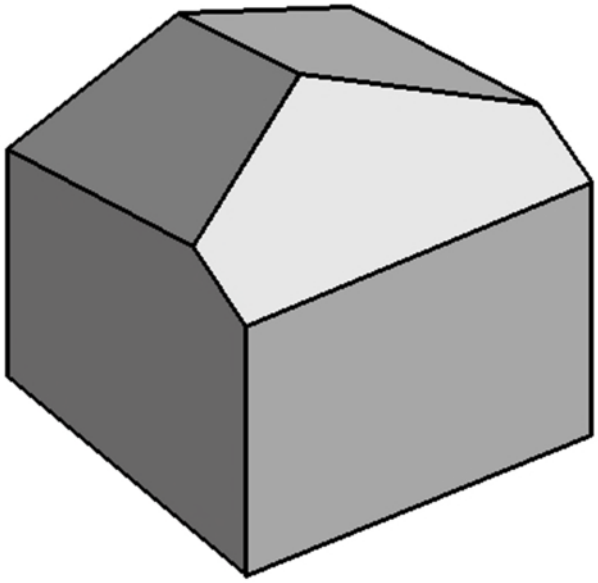

Table 3.1.A, Geometry of Berkovich indenter tip. Modified from (Berkovich Tip, n.d.)

3.2 Nano-Indentation of Ti-30Nb Beta Titanium alloy

The Ti-30Nb alloy was indented using a diamond tip Berkovich indenter with hardness of 98.07GPa, elastic modulus of 1220GPa and a Poisson's ratio of 0.2 (Spear & Dismuhes, 1994). 25 indentations were attempted with a target depth of 2000nm for each, with 22 of these successfully making contact with the surface (SEM image shown in Figure 3.2.B). During these experiments hardness vs depth, modulus vs depth and load vs depth data was recorded.

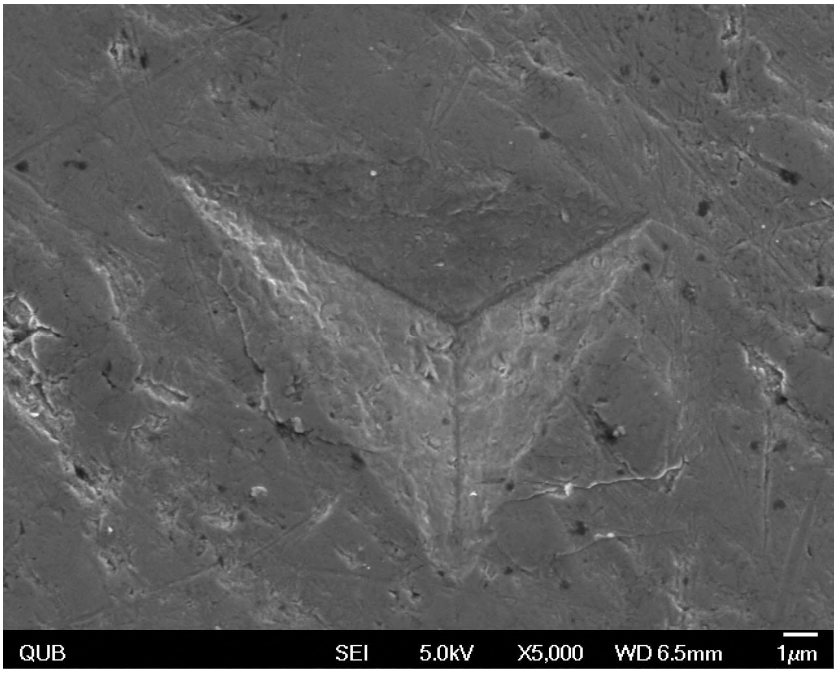

Figure 3.2.A, SEM image of indent 2 (numbering shown in Figure 3.2.B**) at x5000 magnification showing area of indentation made by Berkovich indenter.**

3.2.1 Calculation of Indentation Areas

Area of indents were calculated by two methods, the first being through image processing the SEM images of the indents and the other being the calculated estimation based on the indenter geometry used by Oliver and Pharr (1992).

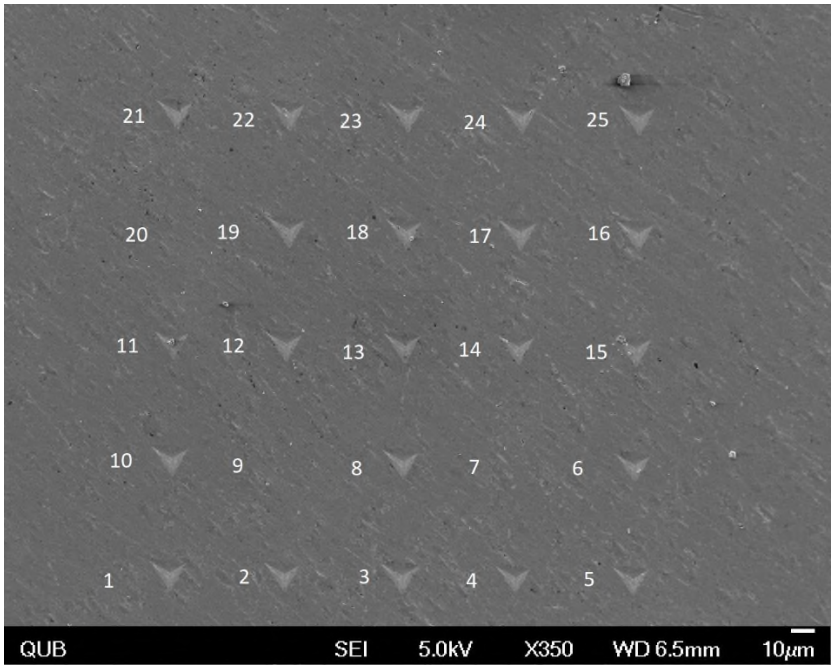

Figure 3.2.B, SEM image of indentations made on Ti-30Nb surface at x350 magnification with numbering of each indent to correspond with data. 25 total indentations were attempted with a spacing of 50μm and a target depth of 2000nm. Indentations 7, 9 and 20 did not make contact with the surface during the procedure and did therefore not leave a visible indent on the surface.

For the image processing, Figure 3.2.B was used to determine the indentation areas. The 10μm scale bar was used to determine the area of a single pixel on the image using the image processing software ImageJ. As the images scale factor was found to be 0.2778μm/px, the area of a single pixel is 7.716×10^{-14} μm^2.

The indentation areas were marked out and a threshold applied, making the indentation areas consist of purely black pixels and the rest of the material white (Figure 3.2.C).

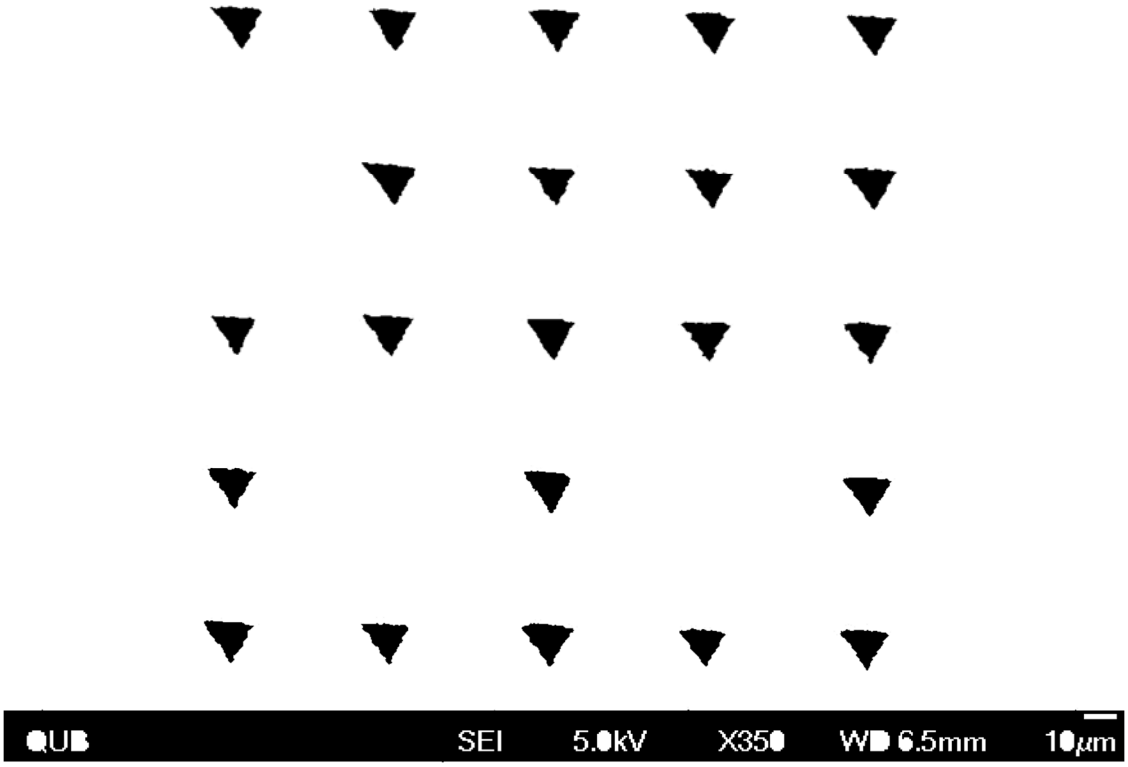

Figure 3.2.C indentation areas after threshold has been applied to Figure 3.2.B for analysis.

From this the number of pixels were measured in each indent by taking a histogram of pixel values over each area, taking all black pixel (greyscale value of 255) as being within the indentation area. Multiplying this value by the area of a single pixel provides the area of each indent in the units of μm². All areas calculated are shown in Table 3.2.A, giving an average of 1.0217 $x10^{-10}$ m² and a standard deviation of 0.0789 $x10^{-10}$ m².

Table 3.2.A, All areas calculated via image processing from the indentations shown in Figure 3.2.B.

Indent number	number of black pixels	area of indent (x10^{-10}m^2)
1	1383	1.06713
2	1289	0.99460
3	1489	1.14892
4	1162	0.89661
5	1276	0.98457
6	1302	1.00463
8	1363	1.05170
10	1279	0.98688
11	1127	0.86960
12	1377	1.06250
13	1337	1.03164
14	1264	0.97531
15	1288	0.99383
16	1502	1.15895
17	1207	0.93133
18	1217	0.93904
19	1469	1.13349
21	1389	1.07176
22	1319	1.01775
23	1420	1.09568
24	1349	1.04090
25	1323	1.02083

Figure 3.2.A was also used to calculate the indentation area as confirmation of the lesser magnified image. The threshold area in this case was determine 5 separate times with an average being take of the calculated area of each measure. This resulted in an area of 1.0121 x10^{-10} m² with a standard deviation of 0.0152 x10^{-10} m². This value aligns with the area calculated previously of all the indents but was not used for the properties calculations as it is not representative of all the indentations made.

3.3 Results of Nano-indentation

Once the unloading gradient, S, had been determined for each indent, as shown in Figure 3.3.A, the maximum load, P_{max} was determined from as average of the maximum values where the curve becomes temporarily flat. Eq. 2 was used to calculate the Hardness, H, form indent while Eq. 1 combined with Eq. 3 and the

properties of the diamond indenter were used in calculating the Elastic Modulus, E, of the Titanium alloy.

The elastic modulus was calculated using both the image processing method of area analysis and the Oliver & Pharr (1992) method. These gave an area of 1.0217 $x10^{-10}$ m^2 and 7.2760 $x10^{-11}$ m^2 respectively. Although these values different significantly, both were used in the calculation of properties to give 2 separate sets of results.

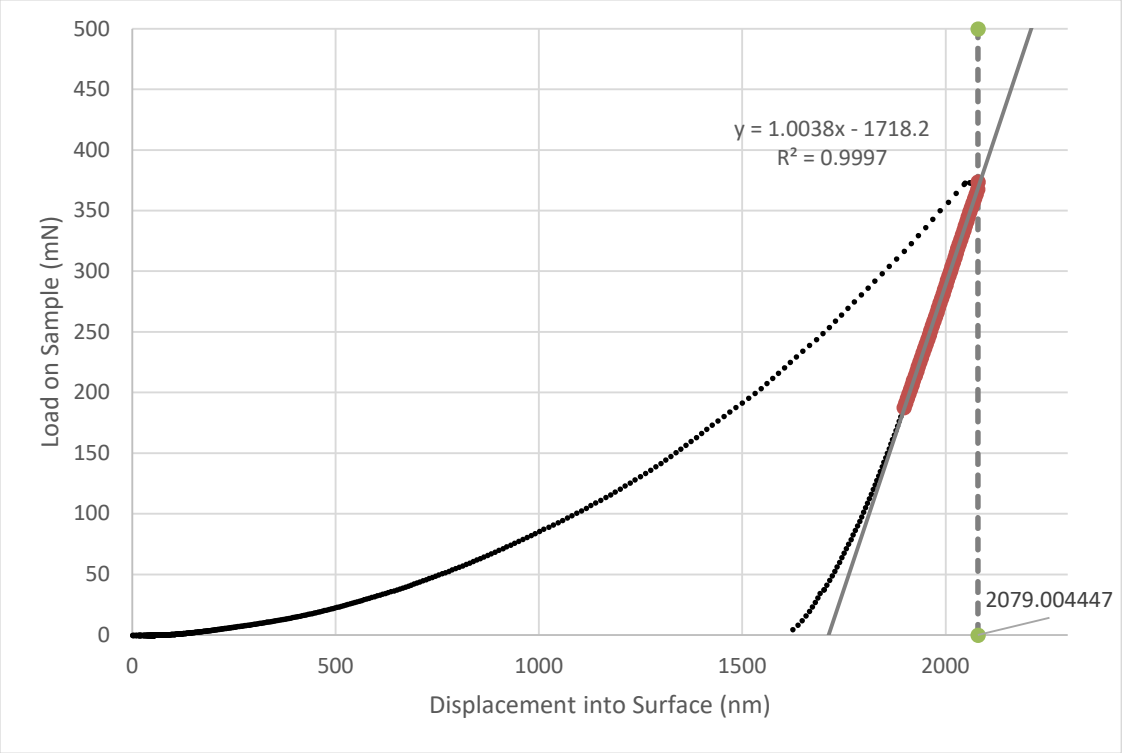

Figure 3.3.A, Plot of load vs displacement for indentation 4 made into Ti-30Nb. The red markets represent points used to calculate the gradient upon initial unloading and both the unloading gradient's equation and h_{max} are displayed on the plot. This was repeated for all indents to determine the elastic modulus.

During the nanoindentation experiments, plots of both the Hardness and Elastic Modulus were directly taken, examples of which can be shown in Figure 3.3.B. Once the plot had plateaued and stabilised, the averages of all values were taken as the Hardness and Elastic modulus determined by the indent in question. All indent properties were then averaged to provide a property value from the whole material.

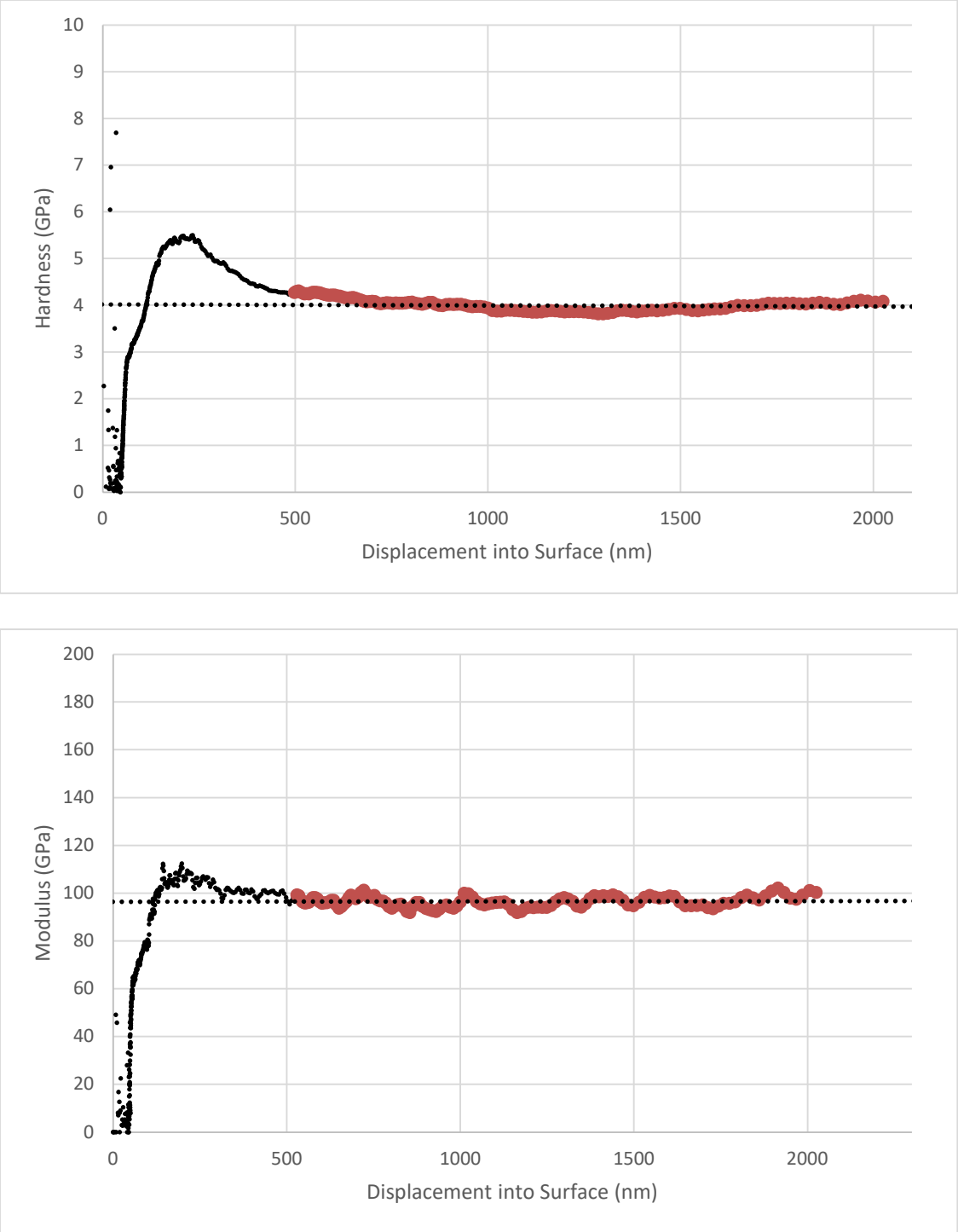

Figure 3.3.B, Above: plot of hardness against displacement, below: plot of modulus against displacement. Both sets of data are taken form indent 4. Red points on both graphs represent the section selected after the values had stabilised to calculate the properties by an average.

All final calculated values are presented in Table 3.3.A with associated errors listed as the standard deviation on the value. The maximum value for Hardness determine from this data states a value of 5.94 GPa and for Elastic Modulus is 111.94 GPa. This dictates that at a worst case scenario where the largest modulus is proven to be true that the alloy Ti-30Nb is still comparable to the currently used alloy, Ti-6Al-4V, for biomedical applications which has an elastic modulus of 110 GPa (Long & Rack, 1998). Although this would not provide any benefits in the mechanical properties that could reduce the effects of stress shielding observed in current implants, it would not cause more severe stress shielding and does provide an increased biocompatibility due to there being no presence of Vanadium or Aluminium. In the best case scenario the elastic modulus has been calculated to be as low as 93.356 GPa which, although still over twice the elatsic modulus of human bone, would still reduce the degree of stress shielding that would occur in an implant by reducing the stiffness of the joint.

Table 3.3.A, Table of material properties calculated via all methods discussed including errors determined by standard deviations of the average values.

	average	±	**standard dev.**
Hardness and Modulus vs Depth Plots:			
Hardness (GPa)	4.603257	±	0.47542
Modulus (GPa)	108.8237	±	7.415673
Load vs Depth Plots with calculated A:			
Hardness (GPa)	5.940118	±	0.559
Modulus (GPa)	111.9407	±	6.312276
Load vs Depth Plots with image x350 mag measured A:			
Hardness (GPa)	4.297091	±	0.326466
Modulus (GPa)	93.87991	±	5.17832
Load vs Depth Plots with indent 2 x5000 mag measured A:			
Hardness (GPa)	4.252914	±	0.266184
Modulus (GPa)	93.35604	±	4.335985

4 METHODOLOGY

Two samples have been machined and analysed in the course of the project. The first sample is a commonly used aerospace and biomedical alloy, Ti-6Al-4V, which has an alpha-beta type microstructure. The second is Ti-30Nb, a beta type titanium alloy that could potentially be better suited for biomedical applications than Ti-6Al-4V due to beta alloys having a lower Young's modulus that better matches that of human bone and the elements that are alloyed to the Titanium being less harmful, granting better biocompatibility.

4.1 Pre-machining Inspection and Design

Before the machining trials begin on the samples. Both the samples and tools were analysed to compare with post machining data, allowing the determination of any chemical or structural changes during the machining process.

Figure 4.1.A. Image of Ti-30Nb wafer prior to machining.

4.1.1 Workpiece Analysis

Both substrates were analysed with X-ray diffraction to verify the microstructure of the material. This was performed on a Siemens D5005 diffractometer with a copper radiation source (wavelength, λ = 1.54Å) using the settings outlined in Table 4.1.A. (Data presented in Appendix A).

Table 4.1.A. Scan settings for X-ray diffraction of pre machined samples.

Starting Angle	10º
Finishing Angle	90º
Step Size	0.02º
Number of Steps	4000
Total Scan Time	66 minutes

Energy Dispersive X-ray Spectroscopy (EDS) was performed on the sample in a Scanning Electron Microscope (SEM) with the analysis performed using INCA software. EDS was repeated on both the samples in Cranfield using an FEI XL30-SFEG running an Oxford Instruments software. For this analysis a 20.0kV electron beam was used at a magnification of 1000x and three sample areas were taken per alloy.

4.1.2 Tool Analysis

Five of the 200µm diameter tungsten carbide tools were selected prior to machining trials to give a representative example of the tools condition, elemental structure and geometry when new. This was performed on the FEI-XL30-SFEG with a 20.0kV electron beam.

Images of the tool were taken from a side view and with the tools mounted at a 45º angle to give a better view of the tools tip. Due to workspace limitations within the SEM it was not possible to acquire images of the tool tip directly as the tools were too long to places vertically in the chamber. The images taken with a 45º angle were scaled vertically by a factor of √2 (1/cos45º) to allow for the tools radius to be measured, with the assumption that the tool's 2 flute tips lie along the same 45° plane. This allowed for measurements of the tool diameter to be made using the scale bar of the images and the line measurement tool in the software, ImageJ.

EDS analysis was also performed on each of the 5 tools to determine the elemental structure. This was performed using a 20kV electron beam along to

tools cutting face to provide elemental composition of the WC tools in their new condition.

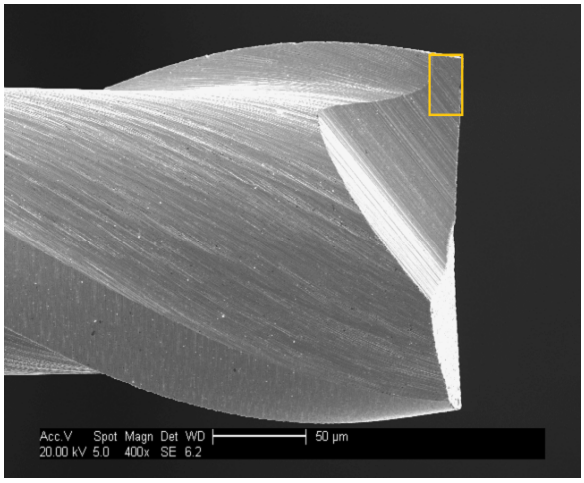

Figure 4.1.B. SEM image of the WC cutting tools prior to machining. Marked in the square is the cutting face where EDS analysis was performed.

4.1.3 Design of experiment and preparation

The trials for the machining experiments were decided based on a Taguchi method, which is a statistical method designed for quality optimisation (Agrawal, Goel, Rashid, & Price, 2015). For the experiments, 3 different levels of each parameter is chosen to give a model of how the variation of each parameter impacts the output without the need to test thousands of different values. These levels are then input into an orthogonal array that allows for full analysis of each parameter's influence using a minimum number of trials. In these experiments the variable parameters are spindle speed, feed rate, axial depth of cut and tool pass overlap. These parameters are selected as they constitute the main inputs that affect the quality of surface when milling a component. For 4 variable parameters being tested at 3 different levels an L9 orthogonal array may be utilised, meaning that a minimum of 9 trials can provide the data required to analyse all 4 parameters influence on the outcome.

Table 4.1.B. Orthogonal array example to be used in machining trials of both Titanium alloys.

Experiment	Variable 1	Variable 2	Variable 3	Variable 4	Measurable
1	Level 1	Level 1	Level 1	Level 3	M1
2	Level 1	Level 2	Level 2	Level 2	M2
3	Level 1	Level 3	Level 3	Level 1	M3
4	Level 2	Level 1	Level 2	Level 1	M4
5	Level 2	Level 2	Level 3	Level 3	M5
6	Level 2	Level 3	Level 1	Level 2	M6
7	Level 3	Level 1	Level 3	Level 2	M7
8	Level 3	Level 2	Level 1	Level 1	M8
9	Level 3	Level 3	Level 2	Level 3	M9

Due to the samples in use being larger than the Kistler minidyn dynamometer being used to record force measurements during machine, a mounting panel had to be designed and manufactured that is capable of securely fixing both of the samples onto the Kistler. Assembly drawings of the panel manufactured can be seen in Figure 4.1.C. The panel is a 150mm x 80mm steel panel of 12mm thickness. 4 through holes allow for the panel to be attached to the Kistler and a further 4 threaded holes are present for the mounting of each of the samples.

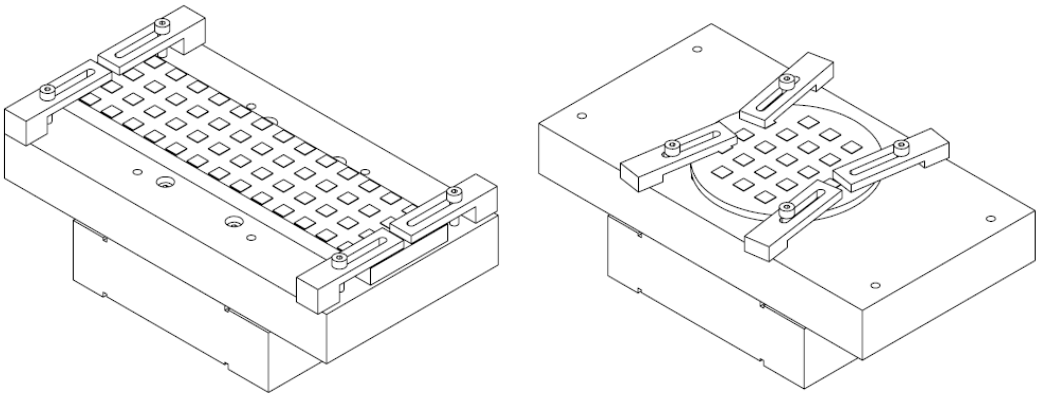

Figure 4.1.C. Assembly of the Kistler mounts manufactured for the mounting of the samples onto the Kistler. Including Kistler, samples and clamps.

4.1.4 Screening of Machining Parameters

Based on the literature discussed previously in 2.2.2 Micromilling of Titanium, three levels were decided for each of the parameters being tested. These can be viewed in Table 4.1.C.

Table 4.1.C. Parameter levels decided for the machining trials of both samples.

parameter	level 1	level 2	level 3
Spindle speed (rpm)	20000	30000	40000
Feed rate (mm/min)	50	150	250
Depth of cut (um)	5	10	15
Step over factor	1.0	1.5	1.99

The spindle speed was decided to be tested for high values due to it being common in literature that values up to 90,000 RPM are used for smaller radius tools but, due the KERN EVO Micromilling machine having a maximum spindle speed of 50,000rpm, this could not be achieved. A maximum of 40,000rpm was used through these trials to avoid overheating of the spindles ball bearings in the machining process. In addition to the three parameters tested in the literature previously reviewed, being spindle speed, feed rate and depth of cut, a tool step

over factor was included to determine the impact of machining areas larger or more complex than a simple linear groove. Although a larger flat milled area is likely to be machined using a larger diameter end mill, some other more complex surface patterns may require the tool to make several passes that overlap with previously machined regions, which will in turn has an impact on the quality of fabrication.

Step over factor was introduced in addition to parameters seen in literature to test the manufacture of flat sections using micro mills. This is a value that is multiplied by the tools radius to determine how far across the tool with move with each pass. Originally this was decided to have a level 3 of 2, but this was changed to 1.99 as the interface would only allow values between 0.01 and 1.99 to be input for this parameter.

4.2 Machining Trials

Both titanium alloys are machined using the KERN EVO Micromilling machine running on Heidenhain machine code. In the machining of both the grooves and flat surfaces cutting chips were collected and all machining trials were performed without any coolant being applied to the substrate or tool to avoid the loss of cutting chips in the machining process.

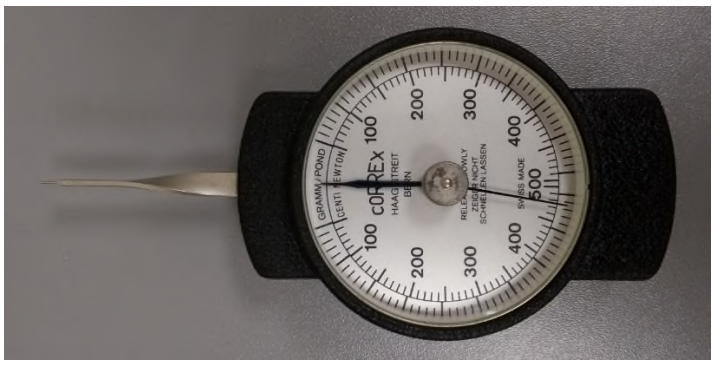

Figure 4.2.A. Strain gage used in the calibration of X and Y axis of dynamometer when measuring forces data.

Once the samples were set onto the mount and the parametric blanks had been machined, a calibration graph for each axis of the Kistler was generated. This was done in the Z axis by placing known weights of 0.5kg and 1.0kg on top of the

substrate. In the X and Y axis a strain gage (Figure 4.2.D) was used to apply forces of 250mN and 500mN to the sides of the manufactured mount. These forces were measured during in both the loading and unloading process.

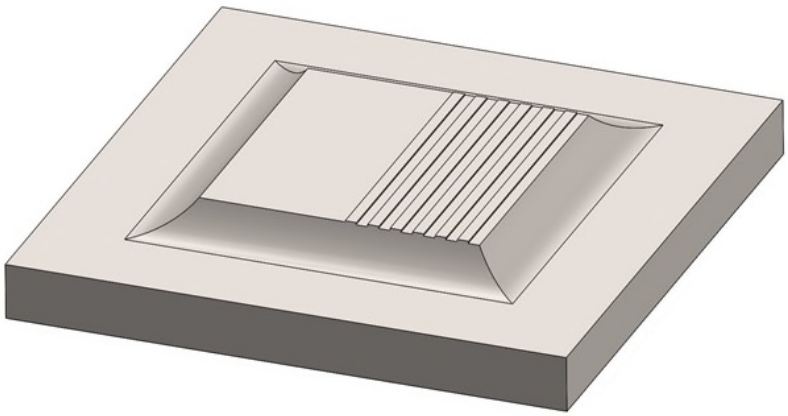

Figure 4.2.B. Model of machined test surface with a single pass flat surface milled at either 5µ, 10µm or 15µm and 6 grooves cut to be 30µm depth and the width of the tools diameter (nominally 200µm)

4.2.1 Parametric blank machining

To generate test surfaces on each of the titanium alloys, blank squares that are 5mm x 5mm in size were machined onto the alloys surface. 5mm end mill was used in the manufacture of these parametric blank surfaces. Due to the 1.2mm cutting radius on this end mill, calculations were carried out to determine effective cutting radius for a 0.5mm depth of cut to ensure each square was fabricated accurately in terms of dimensional size.

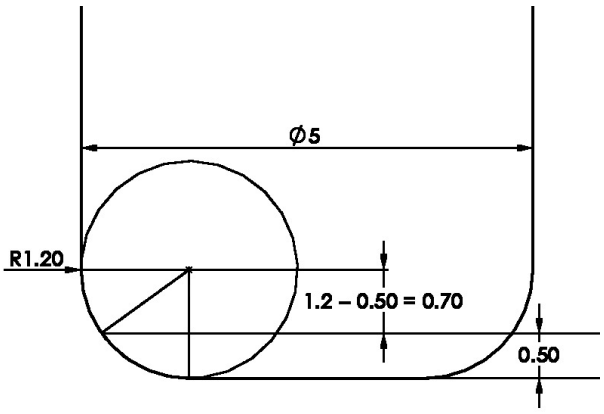

Figure 4.2.C. Schematic of cutting tool dimensions for the machining of parametric blanks. Showing cutting radius, tool diameter and depth of cut.

Simple trigonometry is used in the calculation of the effective cutting diameter, shown in Figure 4.2.C, Figure 4.2.D and Figure 4.2.E.

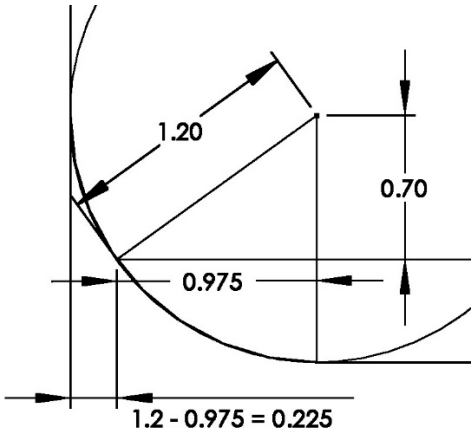

Figure 4.2.D. Schematic of cutting radius. Showing the portion of the radius that is not in contact with the substrate for a 0.5mm depth of cut.

A triangle is determined in which the cutting radius is the hypotenuse, allowing for the horizontal length of 0.975mm to be calculated via Pythagoras theorem. From this is it found that 0.225mm is the effective loss in tool radius on either side of the tool due to the low depth of cut, resulting in an effective cutting diameter of 4.55mm.

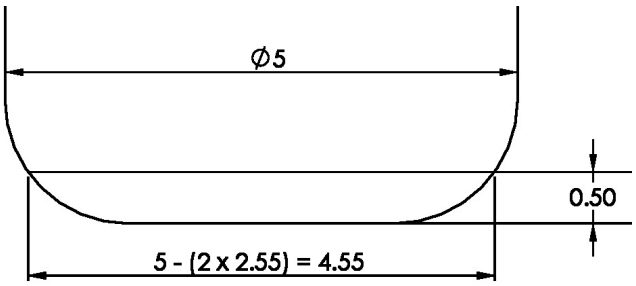

Figure 4.2.E. Schematic of 5mm end mill. Showing the effective cutting diameters in the machining of parametric blanks.

Each channel between the parametric blanks is machined in a single pass with the tool being moved 9.55mm from one pass to the next. This results in 4.55mm slots being machined that lie between 5mm wide lands. With this repeated in both the X and Y axis, 5mm squares are formed on the surfaces.

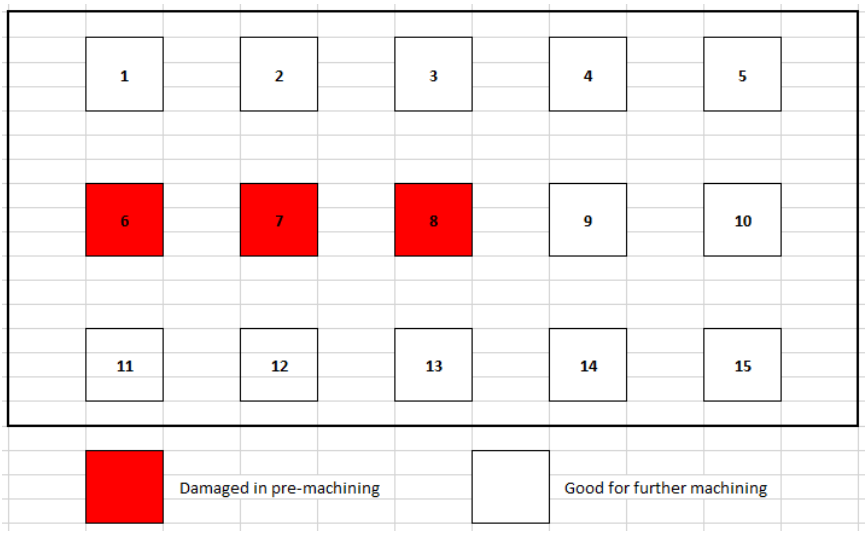

Figure 4.2.F. Layout of 15 5mm x 5mm squares machined onto surface of Ti-6Al-4V sample.

Table 4.2.A. Position of the centre of each square shown in Figure 4.2.F according to the machines co-ordinate system.

Square	X	Y	Z
1	-19.775	9.55	0
2	-9.775	9.55	0
3	0.255	9.55	0
4	9.775	9.55	0
5	19.325	9.55	0
6	-19.775	0	0
7	-9.775	0	0
8	0.255	0	0
9	9.775	0	0
10	19.325	0	0
11	-19.775	-9.55	0
12	-9.775	-9.55	0
13	0.255	-9.55	0
14	9.775	-9.55	0
15	19.325	-9.55	0

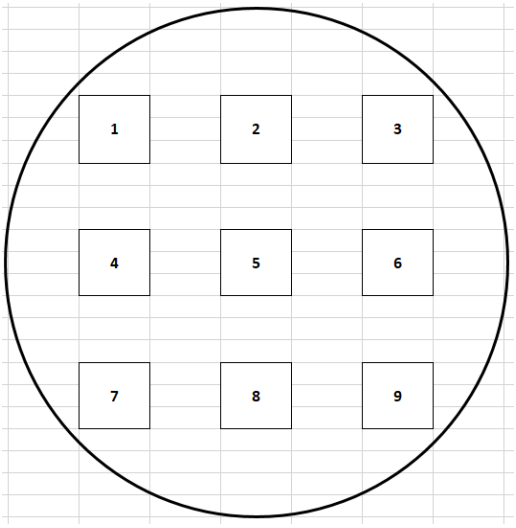

Figure 4.2.G. Layout of 9 5mm x 5mm squares machined onto surface of Ti-30Nb sample.

Table 4.2.B. Position of the centre of each square shown in Figure 4.2.G according to the machines co-ordinate system.

Square	X	Y	Z
1	-9.55	9.55	0
2	0	9.55	0
3	9.55	9.55	0
4	-9.55	0	0
5	0	0	0
6	9.55	0	0
7	-9.55	-9.55	0
8	0	-9.55	0
9	9.55	-9.55	0

In the machining of the parametric blanks the channels were machined first followed by a surface skimming to ensure that test surfaces are machined flat, removing any form curvature. This order was chosen so that any burrs generated by the channels are also machined off during the surface skim, making the micro-

end mills less likely to encounter a large piece of debris remaining from the machining of the blanks that could potentially cause damage to the tool.

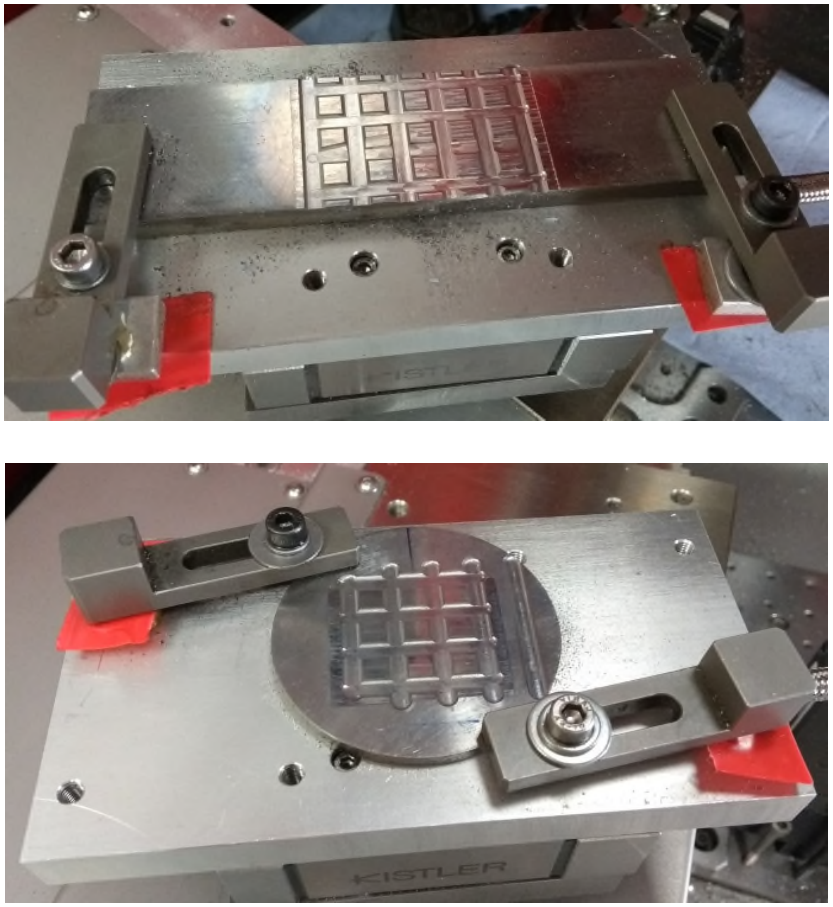

Figure 4.2.H. Ti-6Al-4V (top) and Ti-30Nb (bottom) samples mounted onto the Kistler Minidyn using mounting panel designed.

4.2.2 Flat machining

For each of the squares, the rear 2.5mm is machined using a flat surface milling program. This runs the end mill across the surface at a set depth with all input parameters shown in Table 4.2.C and Table 4.2.D. The machining strategy chosen for the surface milling was Q389 = 2, which can be seen in Figure 4.2.I.

Table 4.2.C. Orthogonal array of parameters used in machining trials with associated Q-codes to create the surface milling program 232 in Heidenhain code.

Experiment	Tool	Q202 Q386	Q370	Q207	
number	number	Depth of cut	Overlap	Feed rate	Spindle speed
1	1	0.005	1.99	50	20,000
2	2	0.010	1.50	150	20,000
3	3	0.015	1.00	250	20,000
4	4	0.010	1.00	50	30,000
5	5	0.015	1.99	150	30,000
6	6	0.005	1.50	250	30,000
7	7	0.015	1.50	50	40,000
8	8	0.005	1.00	150	40,000
9	9	0.010	1.99	250	40,000

Table 4.2.D. Q-code values that remain constant throughout surface flat machining of samples. Codes listed in red represent values which must be added to the squares centre position to be input, and are not the actually Q code values alone.

Q389	machining strategy	2
Q225	X start point relative to centre	-2.5
Q226	Y start point relative to centre	0
Q227	Z start point relative to centre	0
Q218	X axis length	5
Q219	Y axis length	2.6
Q369	allowance for floor	0
Q385	feed rate for finishing	0
Q253	feed rate for positioning	250
Q200	set up clearance	5
Q204	2nd set up clearance	50
Q357	clearance to side	2

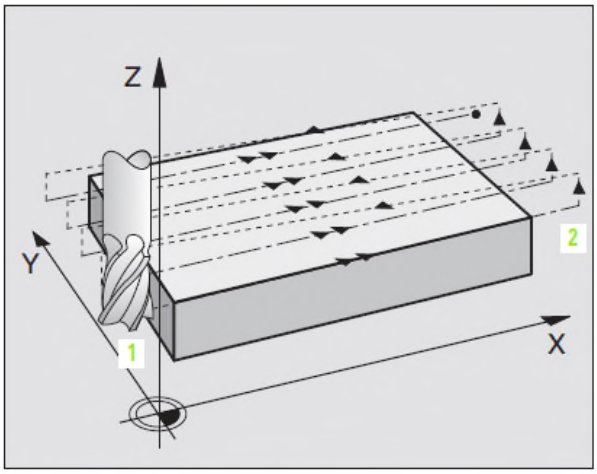

Figure 4.2.I. Machining strategy Q389 = 2 for surface milling program 232 in Heidenhain code.

For each surface the total machining time was simulated and recorded. This time was then used to input the recording time for the force measurements using the Kistler.

4.2.3 Groove machining

The front half of each square was machined using 6 separate slot milling programs, each with a different starting position. The slots are spaced to have a pitch of 0.4mm and are all aligned parallel to each other. The same parameters are used as in the surface milling with the exclusion of the overlap factor.

Table 4.2.E. Orthogonal array of parameters used in machining trials with associated Q-codes to create the slot milling program 253 in Heidenhain code.

Experiment	Tool	Q202	Q207	
number	number	Depth of Cut	Feed rate	Spindle speed
1	11	0.005	50	20,000
2	22	0.010	150	20,000
3	33	0.015	250	20,000
4	44	0.010	50	30,000
5	55	0.015	150	30,000
6	66	0.005	250	30,000
7	77	0.015	50	40,000
8	88	0.005	150	40,000
9	99	0.010	250	40,000

Table 4.2.F. Q-code values that remain constant throughout slot machining of samples. Codes listed in red represent values which must be added to the squares centre position to be input, and are not the actually Q code values alone. The 6 different Y starting values are representative of the 6 separate slots milled.

Q215	Machining Operation	1
	X start relative to centre	-3.5
	1st Y start relative to centre	-2.3
	2nd Y start relative to centre	-1.9
	3rd Y start relative to centre	-1.5
	4th Y start relative to centre	-1.1
	5th Y start relative to centre	-0.7
	6th Y start relative to centre	-0.3
Q203	workpiece surface co-ord. (Z)	0
Q218	Slot length	7
Q219	Slot width	0.2
Q368	finishing allowance	0
Q224	Angle of rotation	0
Q367	Slot position	1
Q351	Climb or up-cut milling	.+1
Q201	Total depth	0.03
Q369	finishing allowance for floor	0
Q206	Feed rate for plunging	100
Q338	Infeed for finishing	0
Q200	set up clearance	5
Q204	2nd set up clearance	50
Q366	Plunge strategy (90° plunge)	0

The X and Y starting positions for this program are not defined by the Q values and are instead dictated by the tools position when the cycle begins. For each slot the machining time was simulated and recorded. This time was then used to input the recording time for the force measurements using the Kistler. For each slots a separate set of forces data was acquired, creating six different force graphs for the machining of the slots.

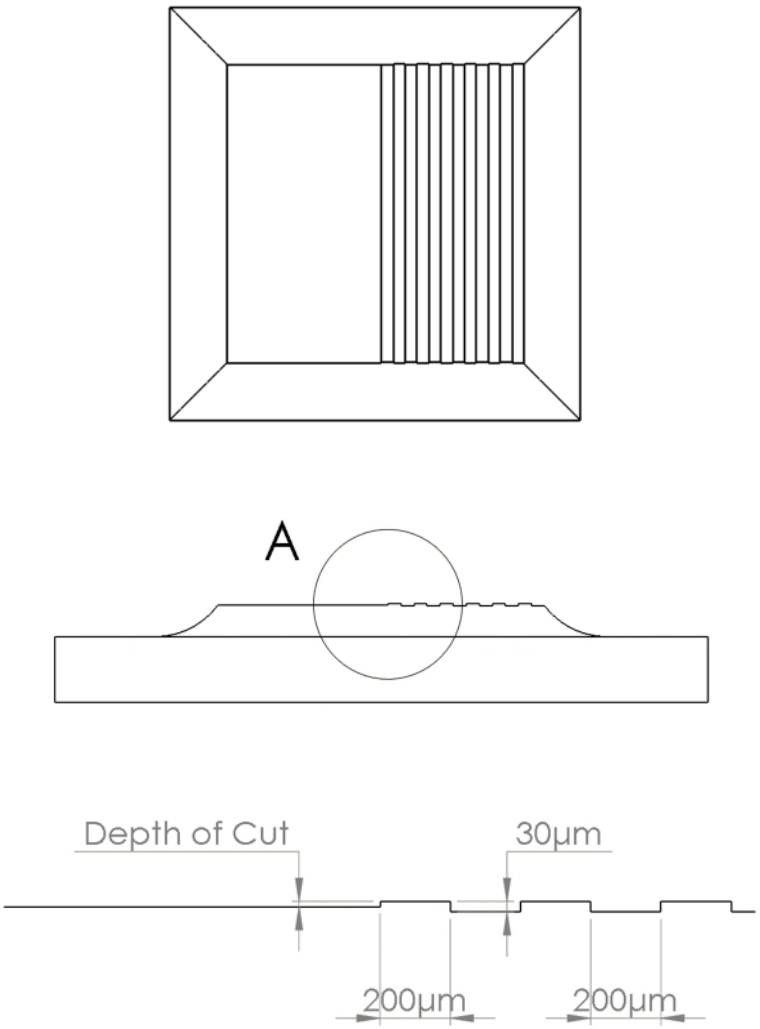

Figure 4.2.J. Drawing of machined features fabricated on each of the test blanks. Top image shows the above view of the surface, Centre shows the side view with detail A marked where the surface features can be seen. Bottom shows detail A at a higher magnification with dimensions for the machining defined. For the flat machining on the left the depth of cut is that of the trial in question, whereas the groove depth of 30µm remains constant for all pillars.

4.3 Post Machining Analysis

Measurements were taken post machining of both the surfaces and tools to characterise the surfaces made, determine any chemical interaction during the machining process and test the functionality of surfaces generated.

4.3.1 Profilometry of Machined Surfaces

To measure the surfaces structures compared to the ideal geometry that was designed for each square, surface measurement equipment was used.

The Dektak ST3 surface profilometer with a 12.5µm radius and 60º cone angle diamond tip probe was used to conduct 2D profile measurements perpendicular to the tools direction of travel in machining. These were run at both the left and right side of each square to show the surface amplitudes at either side of the features, with the left side being where the tool started its pass and the right side being where each cut finishes. A 4.8mm scan length was used to cover the majority of each square with a high resolution and range of 1310kA to ensure all of the grooves are fully measured vertically. Data is recorded every 0.625µm with each scan taking 50 seconds to take 8000 data points.

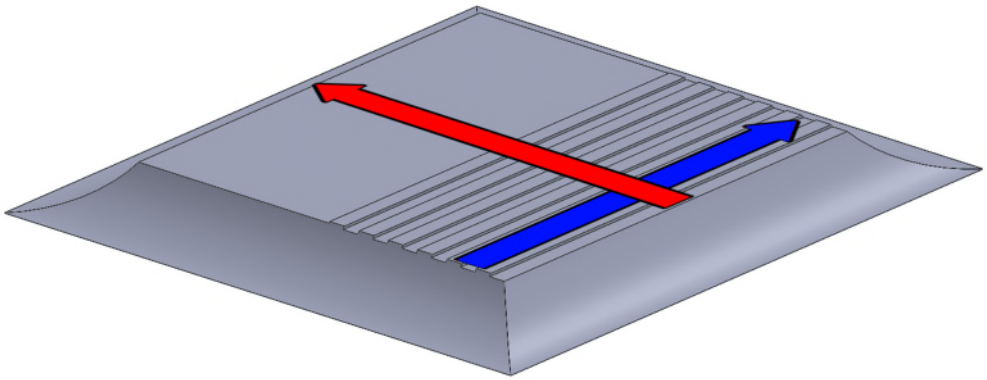

Figure 4.3.A. Model of the structured pillars with Dektak scan directions marked. The red arrow shows the direction of scans taken across the features to demonstrate groove depths and form and the blue arrow shows the direction of scans taken across the bottom of machined grooves to determine the roughness of the groove floor.

From the Data acquired using the Dektak surface profilometer the form of the grooves and flat machined surface was analysed from two scans, one either side of the square, in the direction represented by the red arrow in Figure 4.3.A. Surface roughness was taken along the bottom grooves parallel to the tool direction in machining in the direction of the blue arrow.

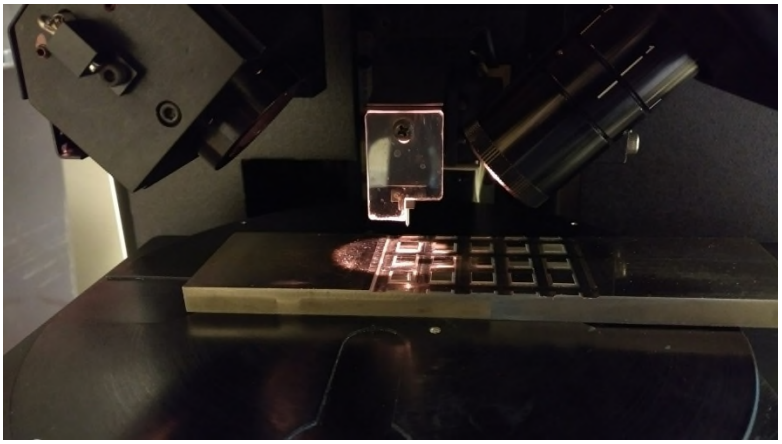

Figure 4.3.B. Ti-6Al-4V sample under analysis in the Dektak ST3 surface profilometer.

4.3.2 Scanning Electron Microscopy

An Environmental Scanning Electron Microscope (ESEM) was used post machining to image both the surfaces and end mills. EDS was also performed on all samples to determine any elemental differences when compared to pre-machining.

4.3.2.1 SEM of Workpiece

On the workpiece 3 images were acquired on each flat surface and 3 of the grooves on each pillar was imaged at 200x magnification. This was repeated for each of the machined pillars with EDS analysis being performed on a section of each image taken. These images were followed by EDS mapping on areas of interest where significant artefacts were identified, allowing the distribution of detected elements to be seen.

4.3.2.2 SEM of End Mills

The 200µm tungsten carbide end mills are imaged under SEM also to view any potential swarf or tool damage present from the machining process. The tools are imaged both flat and at a 45º angle, as with the pre machining measurements. EDS is performed on the cutting face of the tool to check for chemical changes as this is the section with the most workpiece interaction. Any significant amounts of debris left present on the tool are also analysed to confirm their composition.

From the 45° images the tool diameter was also measured with the same method used before machining to determine any significant reduction as a result of wear.

4.3.2.3 SEM of Cutting Chips

Cutting chips that were collected during the machining process were applied to a carbon tape and imaged under the SEM to view their morphology and elemental composition. Images were taken where cutting chips appeared to be at an angle that allowed the identification of any shear band formation in the machining process.

4.4 Measurement of Contact Angle

The measure the functionality of the hydrophobic grooves designed, the software OneAttension was used with a contact angle set up to measure how effective the surfaces are.

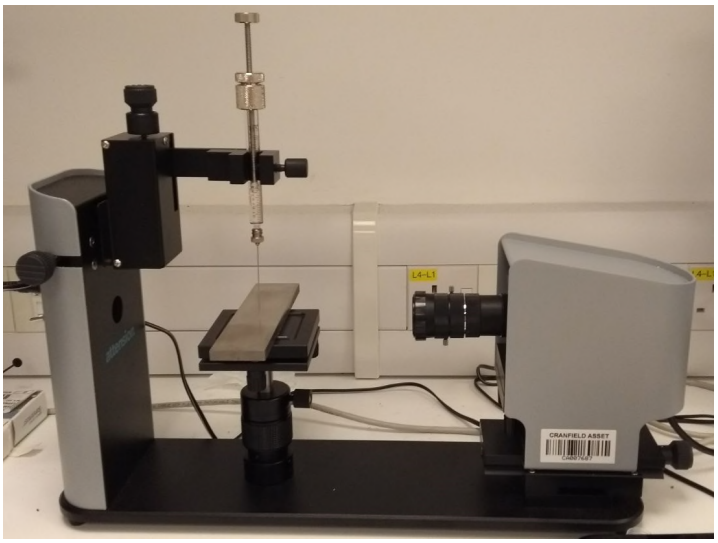

Figure 4.4.A. Contact angle measurement equipment with Ti-6Al-4V in position as substrate.

Before the squares were imaged with water droplets, the reverse un-machined surface of each sample was measured with both alloys using both distilled water and ethylene glycol. By measuring the contact angle using both a polarised and unpolarised liquid it is possible to calculated the surface free energy of the substrate using the OneAttension software. Both water and ethylene glycol have

their properties stored in the software's data base. Prior to every measurement taken the table it first balanced as shown in Figure 4.4.B.This is so that the surface being measured is as level as possible, minimising any potential imbalance due to gravity on the angles either side of the droplet.

Figure 4.4.B. Working surface being balanced using a spirit level to ensure the surface is horizontal when a water droplet is applied.

Contact angles were measured on each of the squares, once on the grooved surface and once on the flat machined surface. For each of these measurements the recording was set to a 30 second pause followed by a 30 second recording at 3 frames per second. This 30 second pause is to allow the droplet to stabilise before measurements begin. Contact angles are measured by the software using the Young-Laplace model and droplet sizes were kept to similar volumes to achieve comparable results. For each experiment all of the calculated angles are saved along with an image taken from the CCD on the equipment. Images were acquired with the camera's line of sight parallel to the groove direction and also with the line of site perpendicular to the groove direction.

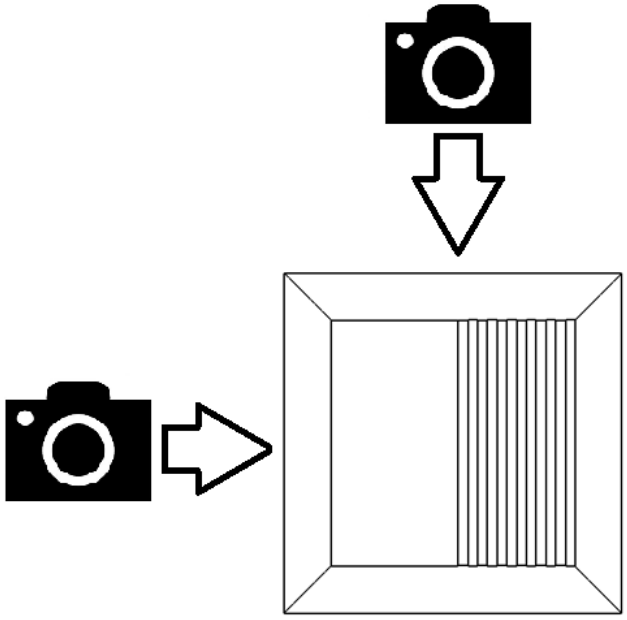

Figure 4.4.C. Top view drawing of the machined features with arrows demonstrating the direction images were taken from during contact angle measurements.

5 RESULTS

5.1 Surface Profilometry

Surface profilometry data was collect for both the form, with a scanning direction perpendicular to the grooves, for both alloys and groove roughness data along the groove bottoms was only collected for the Ti-30Nb alloy.

5.1.1 Form Analysis

Profiles taken perpendicular to the grooves showed that the desired depth of 30µm was not achieved in most cases. Groove depths actually ranged from approximately 21µm and 32µm for different trials on the Ti-30Nb sample, with some showing a consistent depth across all grooves machined, and others varying greatly even over the same square.

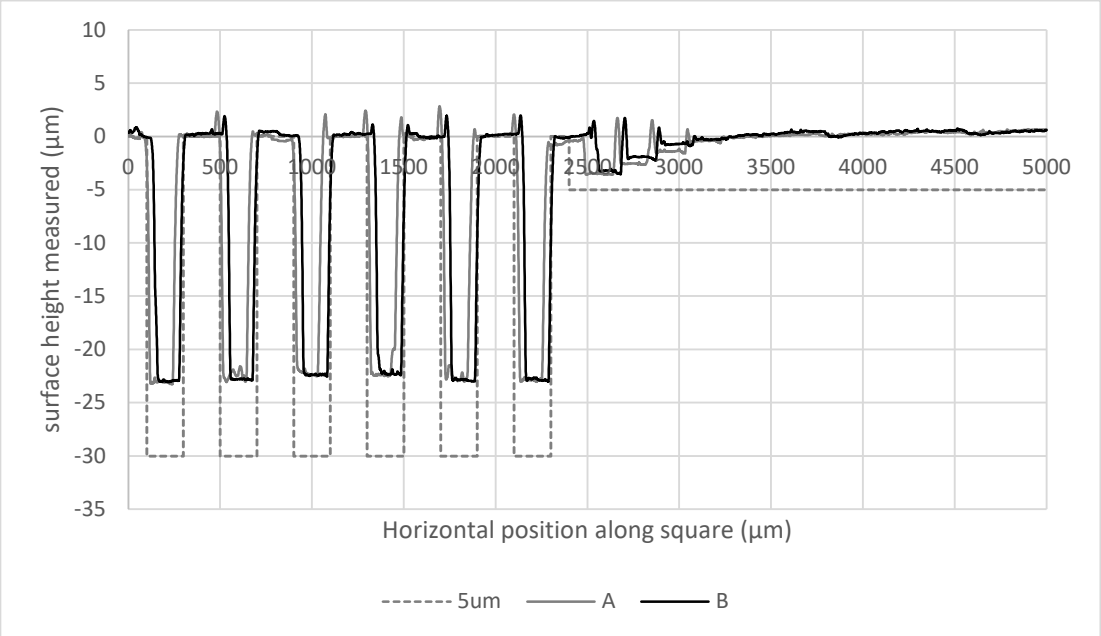

Figure 5.1.A. Form profile of Ti-30Nb square 1. Line A is from the left of the square, line B is from the right and the dashed line represents the targeted profile in the machining process.

Figure 5.1.A shows an example when the groove depths were fabricated consistently at a 22-23µm depth. In contrast, square 3, shown in Figure 5.1.B,

has a gradual decrease in groove depth, ranging from 27μm to 32μm. These depth variations changed with each square.

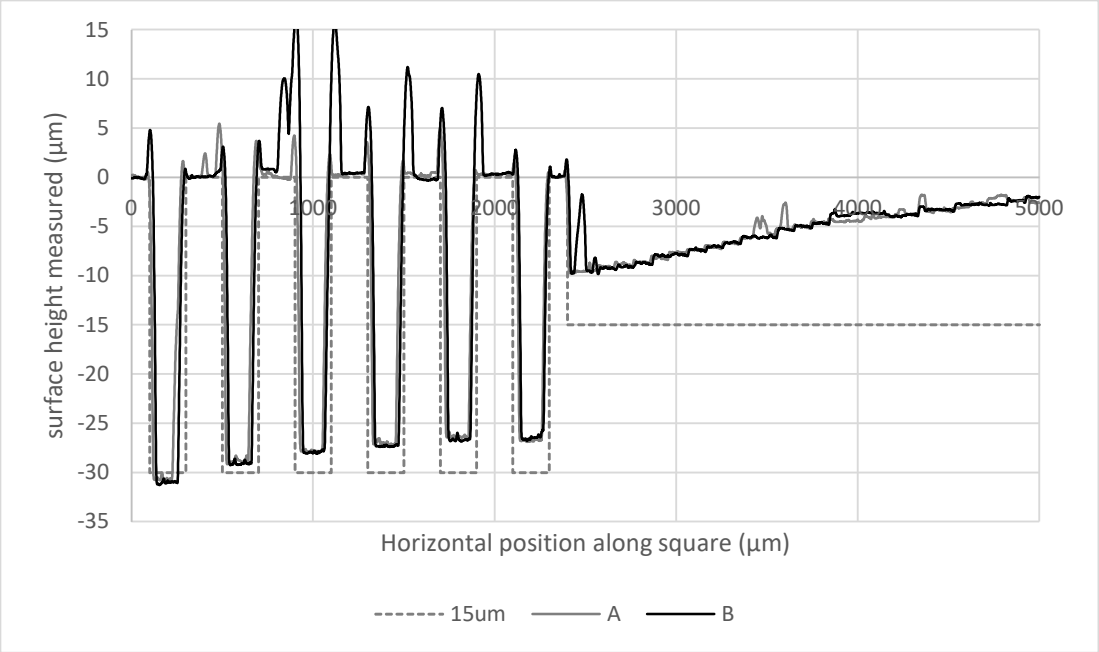

Figure 5.1.B. Form profile of Ti-30Nb square 3. Line A is from the left of the square, line B is from the right and the dashed line represents the targeted profile in the machining process.

Burr formation was very high for some of the squares machined but varied greatly across the samples. In the extreme cases heights such as 16μm and 19μm occurred. In this analysis it appears that the material removal rate (MMR) has a large impact on the level of burr formation observed. The MMR expected in each trial is calculated as follows:

$$MMR = \frac{DOC * d * f}{60}$$

Eq. 9

Where DOC is depth of cut (mm), d is tool diameter (mm) and f is feedrate (mm/min).

Table 5.1.A. Table giving the Ti-30Nb values for groove depths and maximum burr height observed for each square machined with associated theoretical MMR.

Square number	Range of groove depths (μm)	Maximum burr height (μm)	MMR of trial ($x10^{-3}$ mm^3/s)
1	22-23	3	1
2	26-31	10	5
3	27-32	16	12.5
4	20-22	6	2
5	24-26	19	7.5
6	27-28	3	4
7	23-24	2	2.5
8	21-23	7	2.5
9	25-27	19	8

Figure 5.1.A demonstrated a correlation between the size of burrs formed and the material removal rate with the three largest burr sized observed, being 16μm, 19μm and 19μm having MMRs of 12.5mm^3/s, 7.5mm^3/s and 8mm^3/s respectively. Where the smaller burrs all occur when the MMR is significantly low.

The profiles of the flat surfaces of the Ti-30Nb presented some unusual patterns, with all surfaces appearing to have a gradual decrease in depth of cut with each pass of the end mill. When a low depth of cut was used, as in Figure 5.1.A, this quick decline in machining depth resulted in only a small portion of each flat being machined. This could be observed visually on both titanium alloys for squares 1, 6 and 8, the three squares with 5μm depth of cut.

For the Samples machined with a 1.99 tool radius step over large burrs were formed between each pass due to there being no overlap of the tool from the previous pass. This left removed material built up in a small un-machined section between each of the tools pass on squares 1, 5 and 9. This can be seen partially in Figure 5.1.A before the low depth of cut resulted in no contact between the tool

and workpiece, but is much more defined in Figure 5.1.C where the depth of cut was higher, and the higher MMR resulted in increased burr formation.

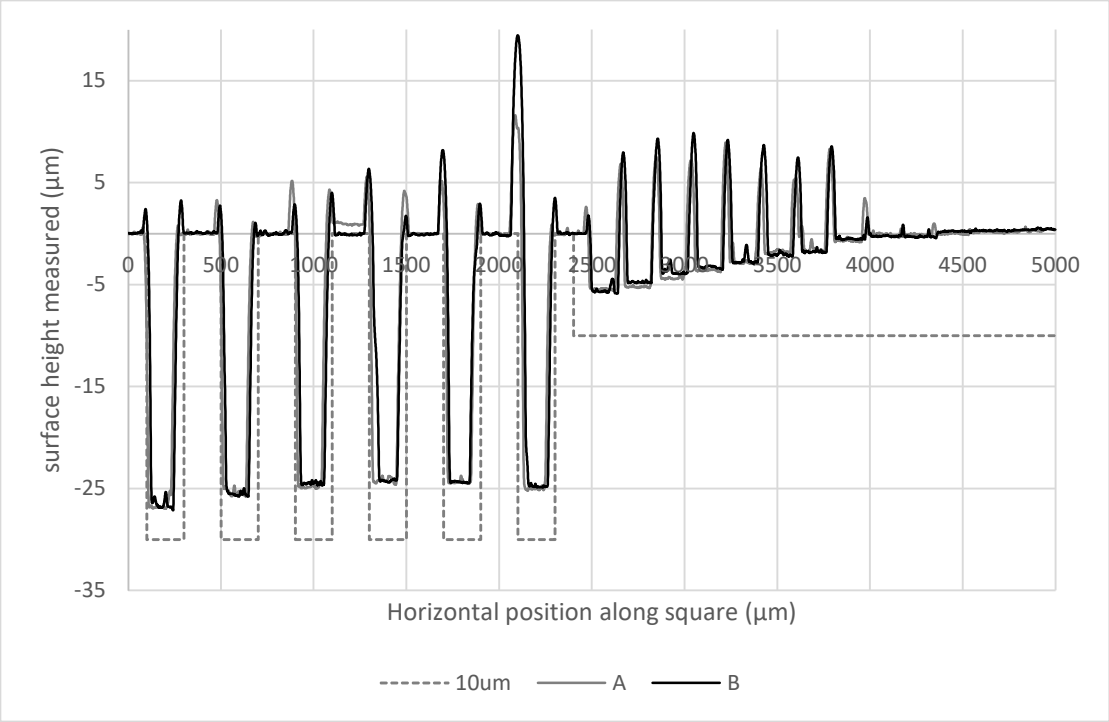

Figure 5.1.C. Form profile of Ti-30Nb square 9. Line A is from the left of the square, line B is from the right and the dashed line represents the targeted profile in the machining process.

The patterns of decrease depth of cut and large burrs forming between each tool pass for the 1.99 radius overlap trials were also observed on the data acquired from the Ti-6Al-4V sample.

5.1.2 Groove Roughness Analysis

Groove roughness analysis for all grooves on the Ti-30Nb alloy is presented in Table 5.1.B.

Table 5.1.B. Surface roughness (Ra) and Peak to Valley (P-V) values extracted form profiles taken across the bottom of each groove on the Ti-30Nb alloy. Average Ra for each square is presented in the bottom row of the table.

		Sq 1	Sq 2	Sq 3	Sq 4	Sq 5	Sq 6	Sq 7	Sq 8	Sq 9
Gr 1										
	Ra (µm)	0.275	0.233	0.164	0.224	0.456	0.182	0.201	0.466	0.367
	P-V (µm)	5.99	3.35	3.67	5.16	15.76	4.03	2.65	11.27	11.30
Gr 2										
	Ra (µm)	0.206	0.136	0.163	0.160	0.436	0.229	0.165	0.365	0.222
	P-V (µm)	3.71	1.44	2.48	5.59	12.38	3.27	2.17	8.95	3.28
Gr 3										
	Ra (µm)	0.194	0.122	0.173	0.126	0.279	0.312	0.271	0.299	0.318
	P-V (µm)	6.14	2.16	3.11	2.16	8.23	97.92	6.56	4.90	5.25
Gr 4										
	Ra (µm)	0.133	0.118	0.277	0.157	0.403	0.482	0.168	0.281	0.240
	P-V (µm)	4.66	2.09	3.58	3.76	10.18	17.21	2.21	6.95	4.07
Gr 5										
	Ra (µm)	0.152	0.148	0.200	0.356	0.339	0.414	0.539	0.296	0.181
	P-V (µm)	2.12	2.09	3.65	13.73	6.06	8.93	18.99	4.51	3.01
Gr 6										
	Ra (µm)	0.170	0.158	0.237	0.160	0.524	0.285	0.426	0.234	0.310
	P-V (µm)	3.03	1.82	4.05	5.37	13.21	8.48	8.92	2.82	5.26
Average Ra (µm)		**0.188**	**0.152**	**0.203**	**0.197**	**0.406**	**0.317**	**0.295**	**0.323**	**0.273**

The trials with minimal roughness occurred on squares 1, 2 and 4, all being under 0.2µm Ra, significantly lower than the majority, which have Ra higher than 0.3µm.

Running a Taguchi designing of experiments analysis using Minitab for an L9 orthogonal array finds that the optimum settings to achieve a low surface roughness in the bottom of the grooves machined are a low spindle speed, low feed right and a medium value depth of cut. Signal to noise ratio plots from the analysis are shown in Figure 5.1.D.

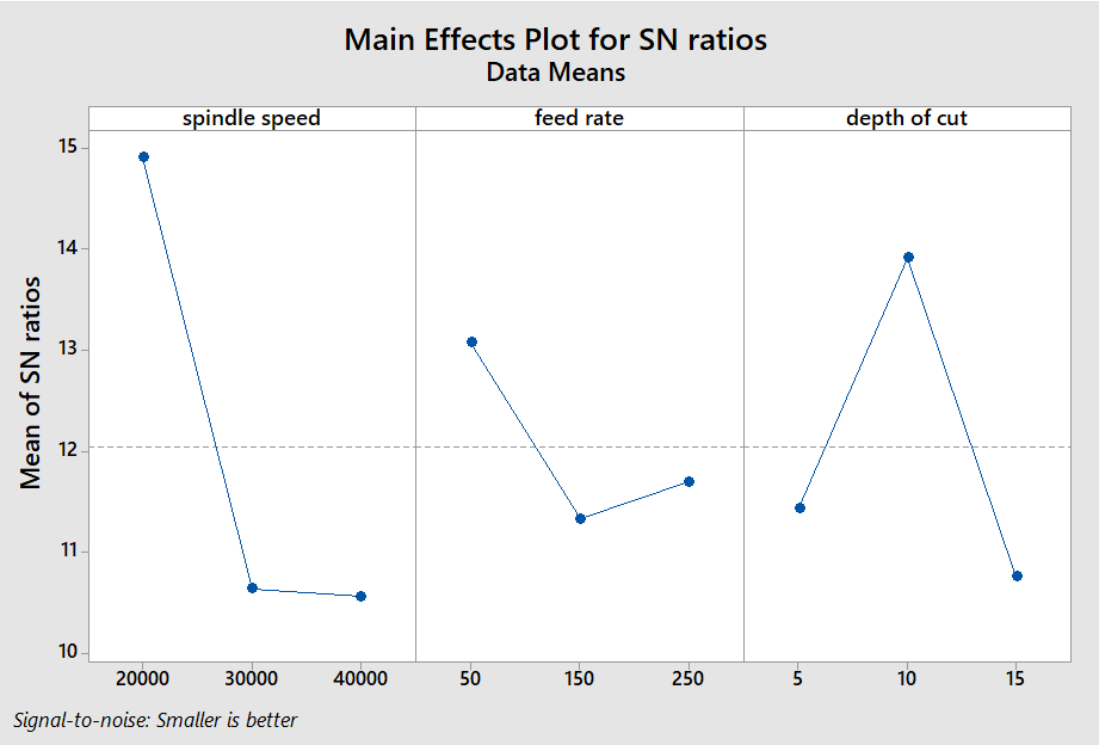

Figure 5.1.D. Signal to noise ratios for spindle speed, feed rate and depth of cut on the Surface roughness in the milling of 30µm deep groove on Ti-30Nb alloy. Higher signal to noise ratio represents a more ideal value for achieving a lower surface Ra.

Although a lower feed rate will provide a higher level of surface quality, there is also machining time to take into account as a trade-off. For the example of a 50mm/min feedrate and a 10µm depth of cut (shown to be the most ideal combination for better surface finish) the machining time was 69 seconds to fabricate a single groove of 30µm depth, whereas the quickest trial being 250mm/min feed rate and a 15µm depth of cut took only 9 seconds to machine the same feature.

5.2 Scanning Electron Microscopy

Scanning Electron Microscopy was performed on the Ti-30Nb alloy post machining as well as all tools used to machine this alloy. Pre machining both alloys were imaged and tested.

Pre-machining EDS analysis determined the Ti-30Nb and Ti-6Al-4V alloys to have compositions shown in Table 5.2.A below as well as the composition of the tools prior to the machining process.

Table 5.2.A. Average elemental compositions by percentage of mass through EDS analysis performed on both titanium alloys and tools before machining. Images shown in 7Appendix B.

Ti-6Al-4V	**Ti**	90.08	%	**Al**	5.69	%	**V**	4.23 %
Ti-30Nb	**Ti**	72.89	%	**Nb**	27.11	%		
WC Tools	**W**	85.64	%	**C**	7.73	%	**Co**	6.63 %

As in the machining of the Ti-30Nb sample the elements present during the interaction of tool and workpiece are Ti, Nb, W, C and Co these were the main focus of all EDS analysis performed on both surface and tools under the SEM. Due to Titanium's high affinity to Oxygen it was also including in all analysis as a default element to search for. All other elements were automatically searched for from the EDS software but only appear in trace amounts and were not consistent between different areas measured, therefore they were deemed negligible.

5.2.1 Titanium Surfaces

5.2.1.1 Ti-30Nb Groove Structures

Across all of the squares, debris has been deposited along the grooves from the machining process. Figure 5.2.A shows surfaces where the debris is most abundant. Debris is left mostly within the grooves themselves near the groove walls, with smaller amounts being left on the top surface around the burrs shown.

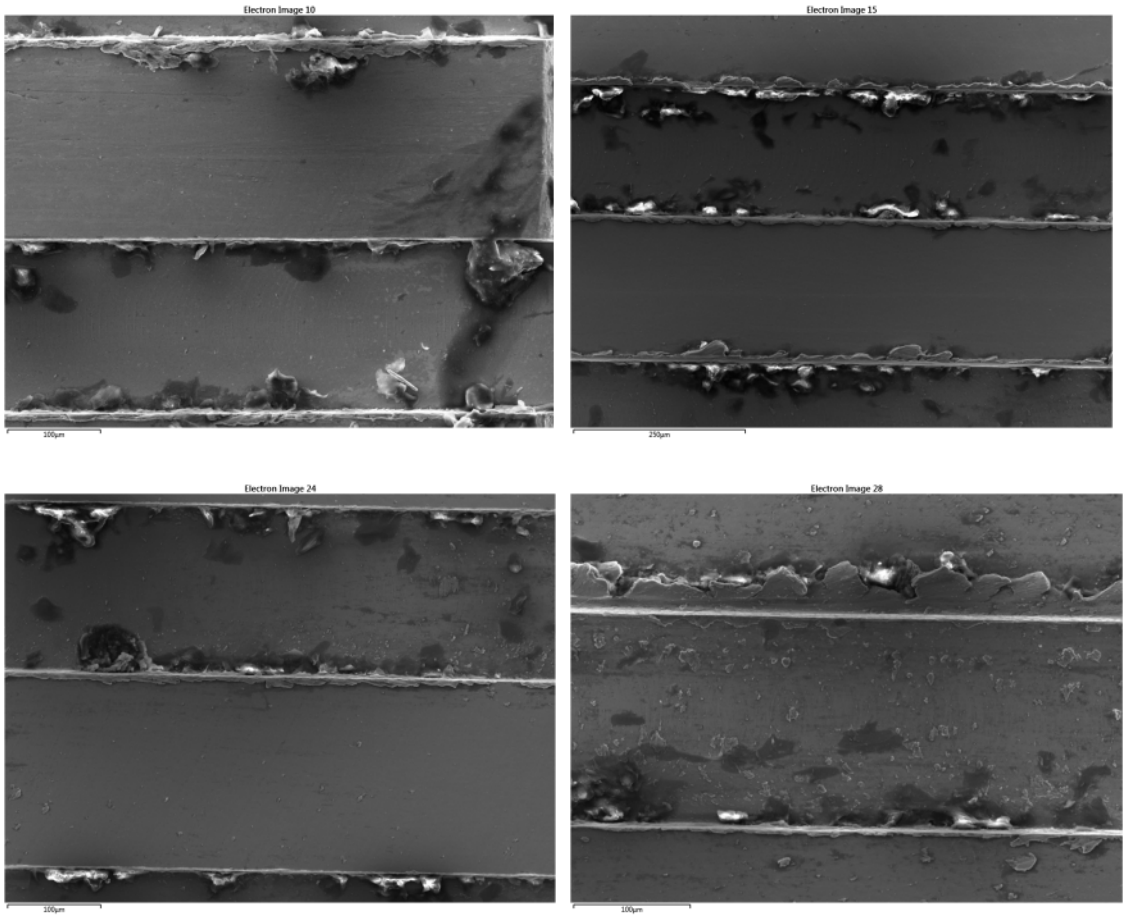

Figure 5.2.A. SEM images of grooves on squares 2 (top left), 3 (top right), 7 (bottom left) and 9 (bottom right). Large levels of debris from the machining process can be seen on all examples shown.

Debris was deposited to a lesser degree on some of the other squares but is still present across all of the samples. EDS mapping performed across the areas where burrs and debris were present revealed a high content of carbon and oxygen in these pieces of material. As shown in the EDS map data in Figure 5.2.C.

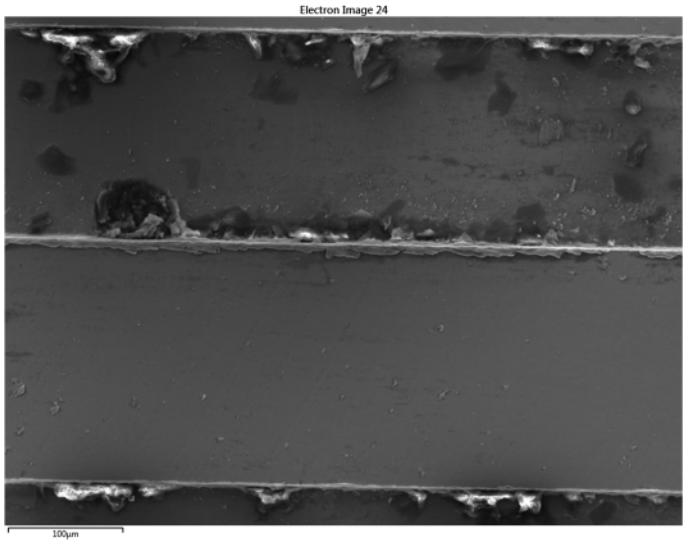

Figure 5.2.B. SEM image of groove machined on square 7 of the Ti-30Nb alloy.

This EDS map shows not only that there are high levels of Carbon and Oxygen present in the debris left on the surface, but also an absence of Titanium and Niobium for these regions. This suggests that the majority of the debris formed on the surface during the machining process could be pure Carbon rather than a reaction having occurred between Carbon, Oxygen and the alloy. Over the remaining areas, such as the bottom of each groove and the top surface above the grooves, there appears to be only Titanium and Niobium present still as these are the regions with minimum interaction with the end mills cutting edge. Tungsten and Cobalt were seen in trace amounts and were not particularly localised to any region, therefore they are not considered to have any significant reaction with the surface during the machining process. These observations proved true for all EDS groove analysis where debris was imaged, with the debris appearing to be pieces of Carbon and Oxygen deposited on the surface.

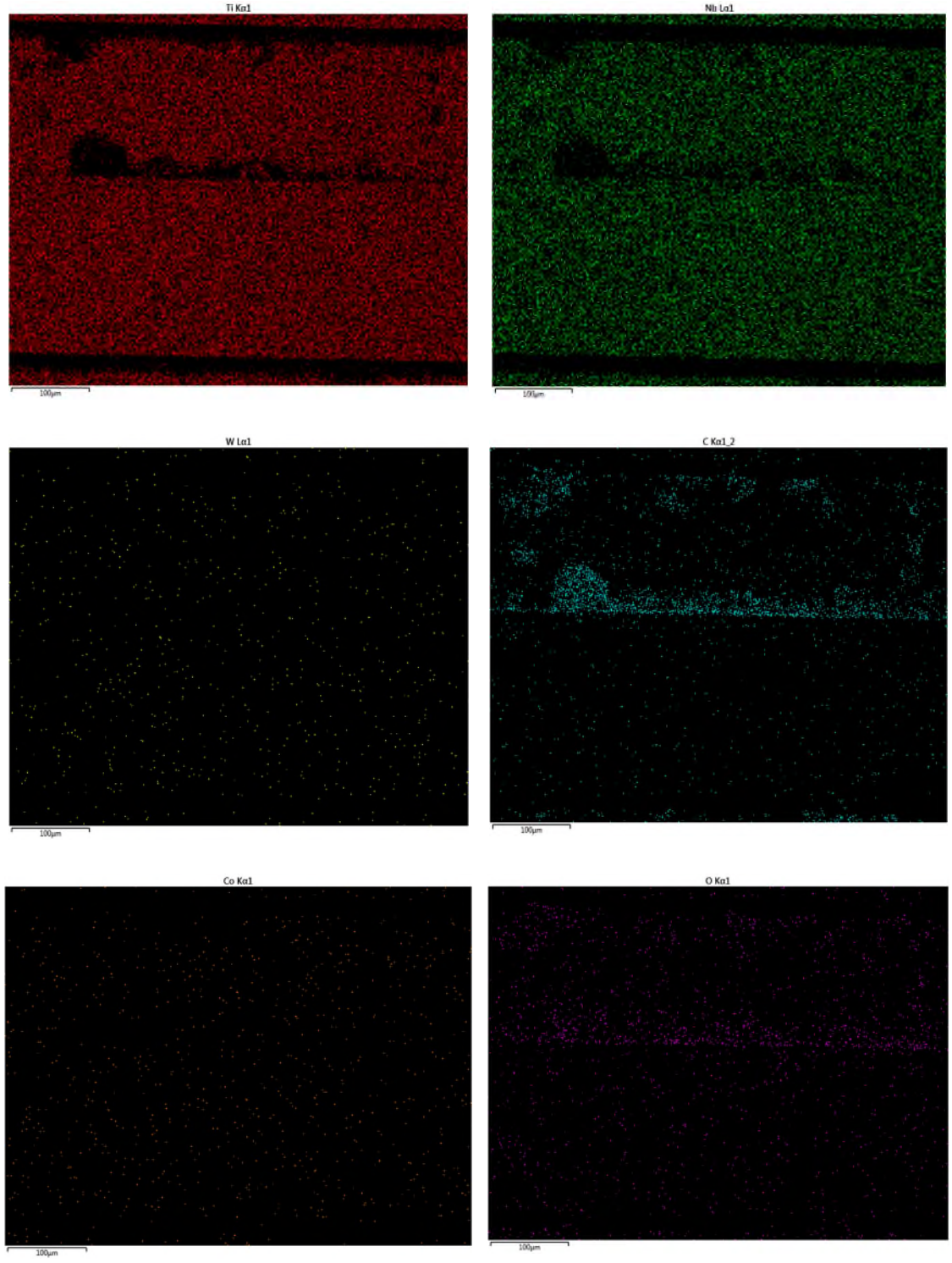

Figure 5.2.C. EDS mapping data of the image shown in Figure 5.2.B showing elemental distribution across sample. Top left: Titanium. Top right: Niobium. Centre left: Tungsten. Centre right: Carbon. Bottom left: Cobalt. Bottom right: Oxygen.

5.2.1.2 Ti-30Nb Flat Surfaces

On the flat surfaces the majority of the EDS mapping returned only showing Titanium and Niobium on the surfaces. This is because as the entire surface is being machined rather than a single groove the majority of the alloy that has interacted with the cutting edge is being removed from the surface, including the majority of debris that was observed in the groove machining. Exceptions did occur to this where smaller sections of debris were left of the surface though but to a lesser degree.

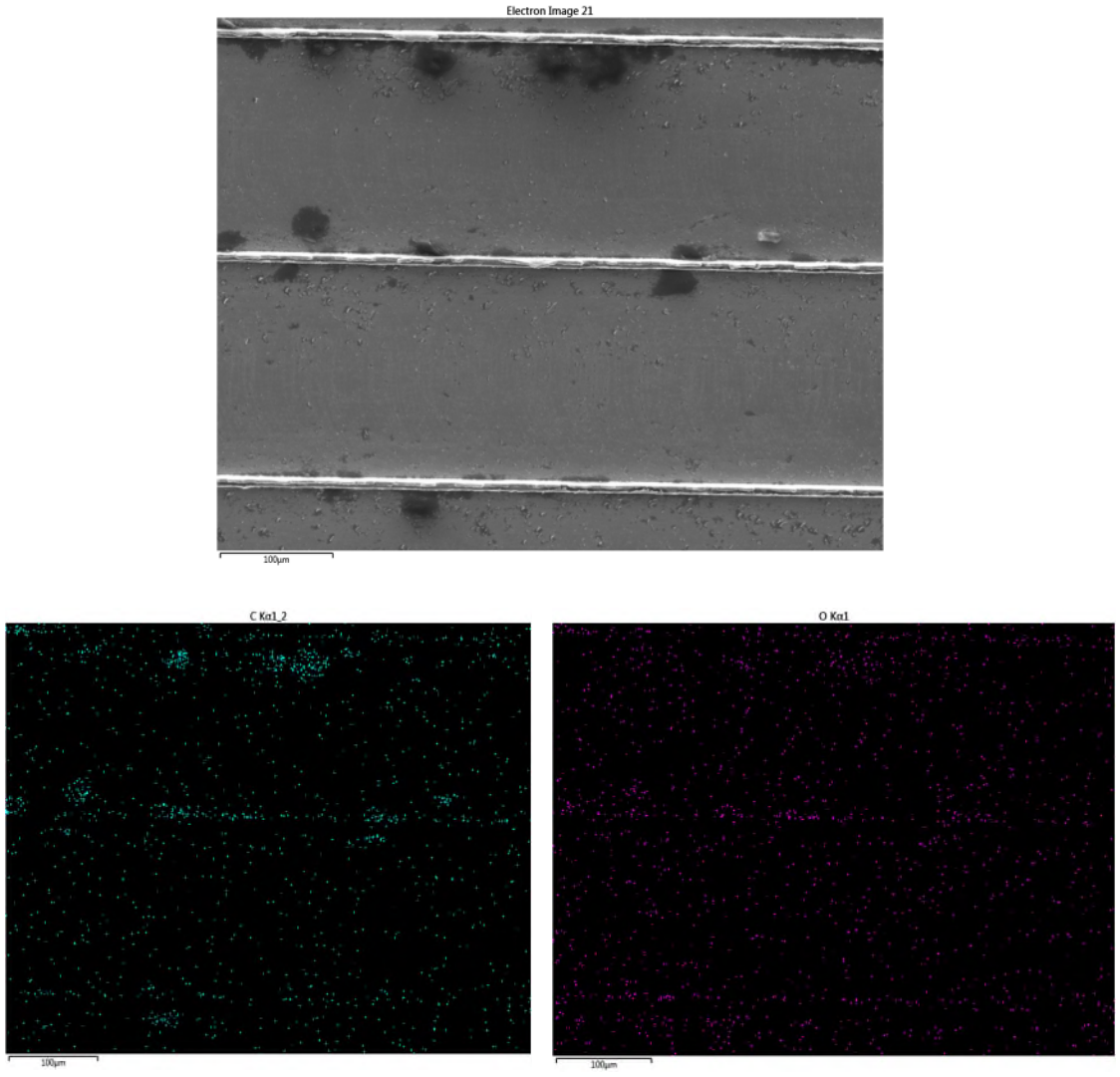

Figure 5.2.D. Top: Image of flat machined surface of square 5 of Ti-30Nb. Bottom left: Carbon distribution across image. Bottom right: Oxygen distribution across image.

One of the reasons for exception occurred to the 1.99 overlap in the machining of squares 1, 5 and 9. As discussed in Profilometry of Machined Surfaces, large structures running parallel to the direction of machining were generated due to there being a thin section of alloy that was not contacted by the tool between adjacent passes. This can be seen in Figure 5.2.D, where the EDs maps show that along these lines Carbon and Oxygen are present, as with the debris left in the machining of the grooves.

Another Exception to this occurred due to the effect shown in Profilometry of Machined Surfaces where the flat surfaces machined depth gradually decreased in steps with each pass of the tool. SEM images of these flat surfaces clearly show small ledges that correspond to the plot profiles for each pass the tool has made, with the tooling marks clearly visible on each ledge.

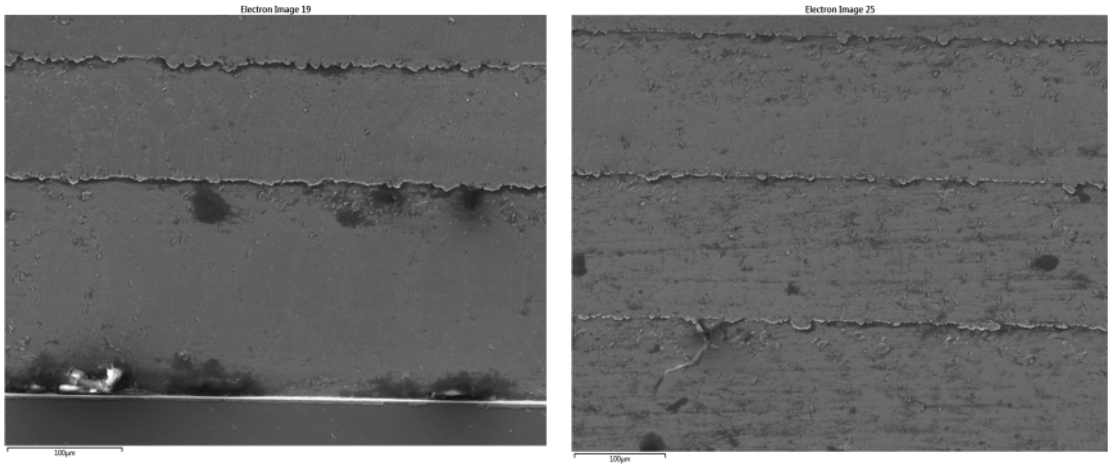

Figure 5.2.E. SEM images of the flat machined surfaces for square 4 (left) and square 7 (right) demonstrating the generation of small ledges with each machine pass as a result of the machining depth decreasing over the surface.

In Figure 5.2.E above, these ledges can be clearly seen where it is expected that the surface would be flat from the machining program. The edges of these passes results in minor amounts of debris and burring which shows the presence of Carbon and Oxygen also. This stepping affect was visible across all squares to some extent, as seen in the surface profilometry.

5.2.2 Milling Tools

5.2.2.1 Diameter Measurements

Pre machining diameter measurements from the SEM images gave the values for the 5 tools measured that are presented in Table 5.2.B. Measurements of diameter taken on 5 tools pre-machining. This data gives an average diameter across all tools measurements of 174.91 ± 4.39μm. This value is significantly less that the specification for the tools which is a diameter of 200μm, which could be to allow for coatings to be applied to the tools while remaining below the 200μm diameter. As in this case the tools are uncoated there is just a decreased diameter.

This decrease in diameter also explains further why there is the fabrication of features between each pass of the trials with 1.99 overlap occurred. This is because with this decreases diameter there is on average a 25μm strip for each tool pass that has no direct contact with the milling tool. Resulting in features approximately 25μm in width.

Table 5.2.B. Measurements of diameter taken on 5 tools pre-machining.

Tool	Diameter, D [um]		ΔD [um]
A	171.77	±	1.90
B	175.69	±	1.94
C	179.69	±	2.02
D	176.69	±	1.99
E	170.69	±	1.96

Post machining measurements performed in the same manor revealed an average of 180.31 ± 10.82μm. Although the post machining average appears to be higher than the pre machining diameters, the errors associated with the measurements do provide a large region of overlap. It would appear from these results that the tools diameter did not decrease through the machining process but with the large range of diameters between the tools measured it could be possible that the average values in this case were not representative of the actual diameters of the tools. Difficulties in measuring the post machining tools also arose due to the ESEM being used rather than the higher resolution FSEG as it

was not available as the time and also as there was significant swarf build up on some of the tools post machining.

Table 5.2.C. Measurements of the diameter taken on the 9 tools used in the machining of Ti-30Nb alloys post machining trials.

Tool	Diameter, D [um]		ΔD [um]
11	179.5074	±	3.48554
22	177.5743	±	3.073739
33	178.9899	±	4.420052
44	178.7192	±	3.884854
55	181.0448	±	3.934722
66	181.3065	±	2.73501
77	182.8718	±	3.816974
88	182.3881	±	3.470841
99	180.402	±	3.344951

5.2.2.2 Imaging and EDS Analysis

SEM images of the tools revealed that the WC end mills were reasonably effective in the machining of Ti-30Nb with minimal visible wear in all cases and no clear decrease in size.

Although there was no large wear volumes observed there were factors of wear visible on several of the tools. On tool 33 (**Figure 5.2.G**) there's a clear adhering of alloy to the cutting face of the milling tool that has built up from the cutting edge. As well as some minor marking appearing down the side of the tool that could possibly be a result of swarf being moved up the flutes as the materials is being removed. Any wear as a result of this build up edge appears to be minimal as the geometry of the tool has no significant change from the nominal that was imaged previous to machining. Adhering of the alloy was also visible to some degree on all tools as can be seen from **Figure 5.2.H**, Figure 5.2.I and Figure 5.2.J where smaller amounts of material remain on the tool. Built up edge was observed more clearly on tools 22, 44, 55, 66, 88 and 99 where small amounts of material appear to be strongly adhered to the cutting edge itself as seen in Figure 5.2.F.

Figure 5.2.F. Tool 88 imaged at a higher magnification, showing clear built up edge down the cutting edge to the left of the marked area. EDS in this region confirmed the presence of both Titanium and Niobium adhering to the surface.

Wear due to attrition is not common at a visible scale on all of the tools used, although it can be seen on tool 44 in the form of chipping along the tools end. Although this section of the tool is fairly removed from the cutting edge of the tool itself it still has some contact with the bottom surface and swarf will pass this section as it is removed, possibly being the reason for the chipping if a larger section of swarf was to adhere to this surface or impact it in some way (This chipping can be seen in Figure 5.2.H).

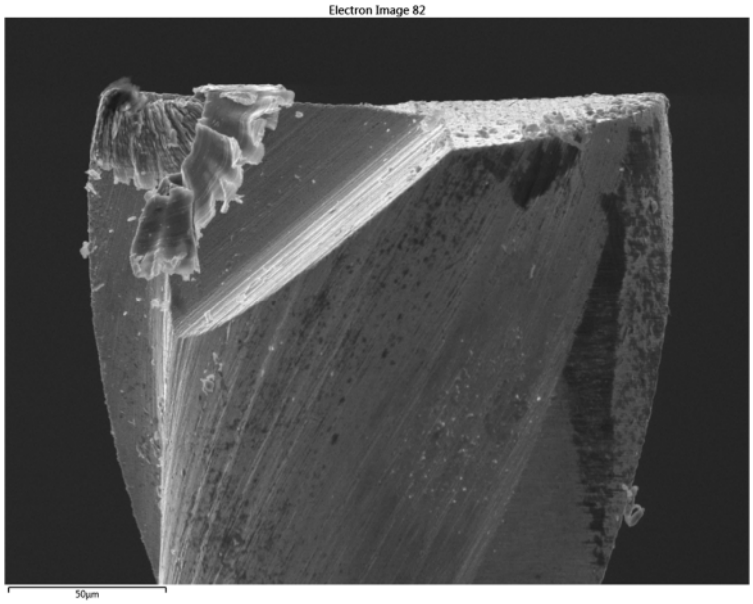

Figure 5.2.G. SEM image of tool 33 use in the machining of square 3 on the Ti-30Nb alloy after trials.

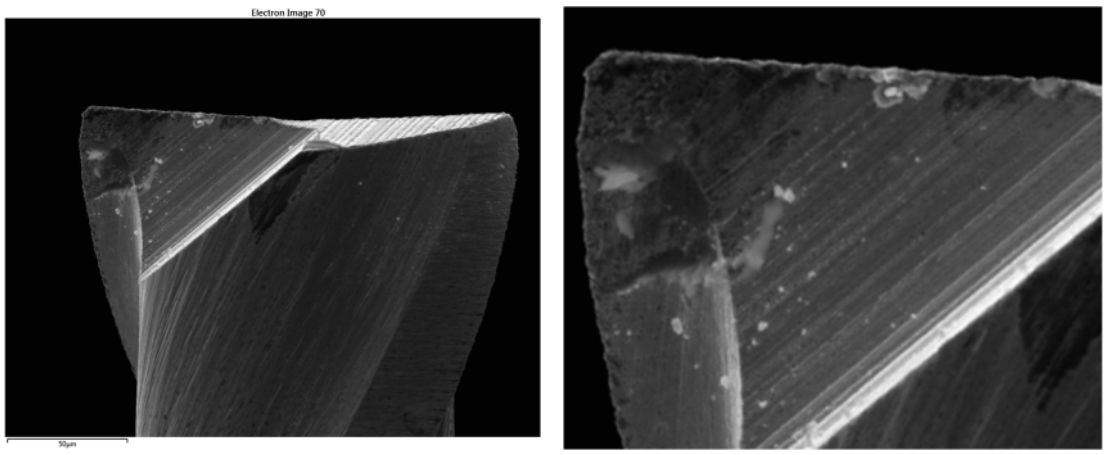

Figure 5.2.H. SEM image of tool 44 use in the machining of square 4 on the Ti-30Nb alloy after trials. Right image is a higher magnification of left image showing damage to tool edge.

Although there is signs of Carbon on the surface of the alloys, it appears unlikely this is due to diffusion from the tool itself. The edges of the tools appear to remain comparable in sharpness to the pre-machining tool measurements. If diffusion had been a significant factor as a reason for the Carbon deposits it would seem likely observations would be made where the tool had lost significant volumes of material from the interacting edge, especially for the abundance of Carbon

observed on the machining surface. It's possible that diffusion has occurred in the process but if so then it is believed to be at a minimum and not the leading mechanism of wear in this situation. This also appears to be true for plastic deformation of the tool as the tools do not appear to have suffered any significant geometrical changes in the machining process.

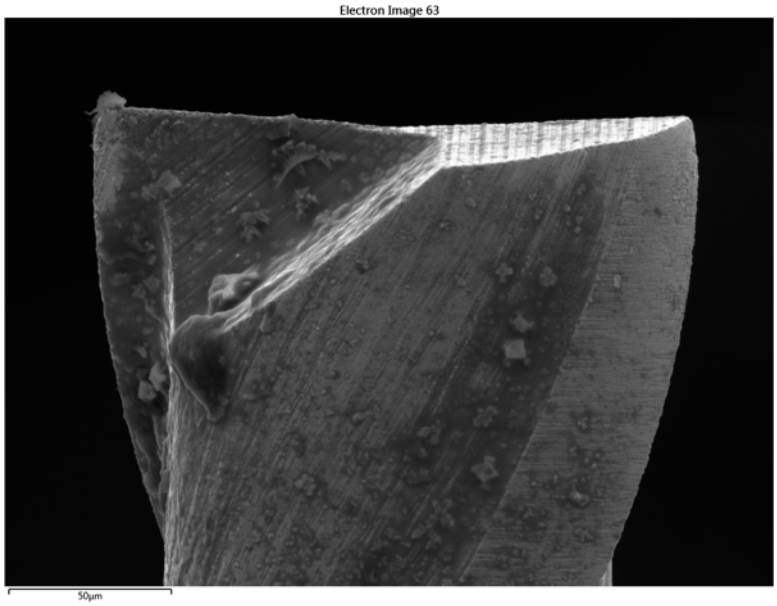

Figure 5.2.I. SEM image of tool 11 use in the machining of square 1 on the Ti-30Nb alloy after trials.

Although thermal cracking is not clearly visible form the mages acquired, it could still be a possibility on a smaller scale that isn't visible on the ESEM used in post machining imaging. Potentially with the FSEG SEM imaging at a higher resolution it could be possible to view some cracks along the tool edges. If this was the case then it would be partially expected due to the low thermal conductivity of Titanium alloys creating a large temperature gradients between the workpiece surface and the cutting tool. It is also likely that at this minimum depth of cutting and extremely low material removal rates there is not a high enough level of interaction between the tool and workpiece for temperatures to increase to a degree where damage through thermal cracking could occur.

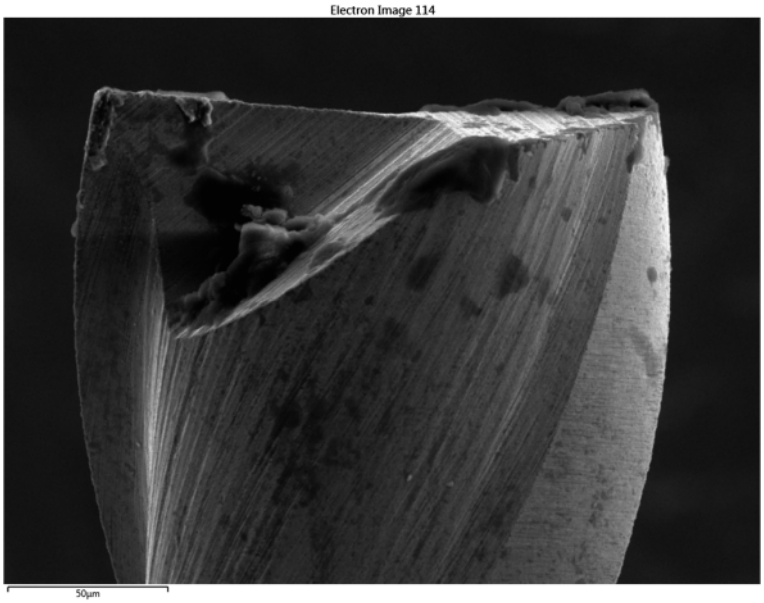

Figure 5.2.J. SEM image of tool 88 use in the machining of square 8 on the Ti-30Nb alloy after trials.

5.2.3 Cutting Chips

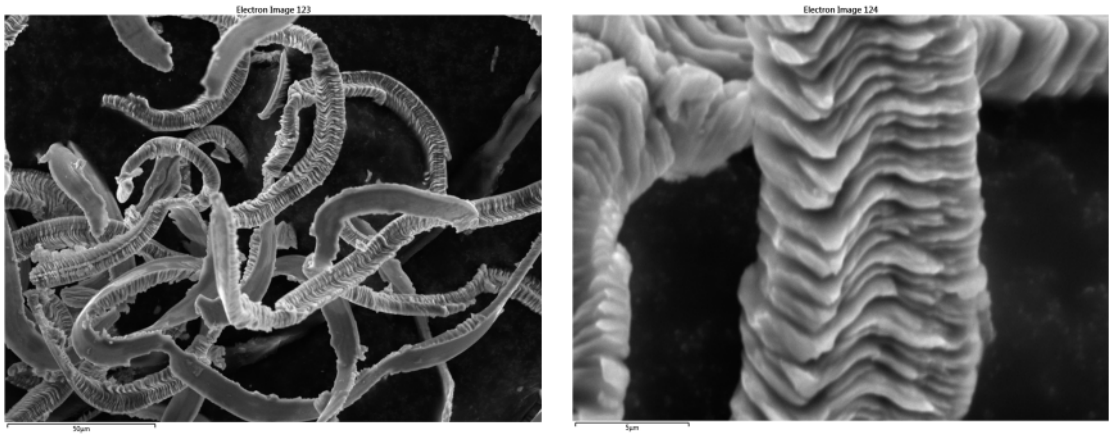

Figure 5.2.K. SEM images of the Ti-30Nb cutting chips collected from the machining process. Right image is of a higher magnification showing in greater detail the chip morphology.

Cutting chips imaged under SEM were of great difficulty to view in high detail due to resolution limitations of the ESEM. As seen in Figure 5.2.K the cutting chips were only approximately 5µm in width. At this scale a high level of sharpness is

difficult to obtain through the ESEM and the FSEG would have been a more appropriate piece of equipment to use if it was available.

Regardless of these limitations, the cutting chips observed all appear to follow a similar morphology that is characteristic of Titanium alloys when machined. On all chips there are two clearly defined sides, one which appears to be a smooth surface, and the reverse which appears as a series of periodic strips across the cutting chip known as shear bands.

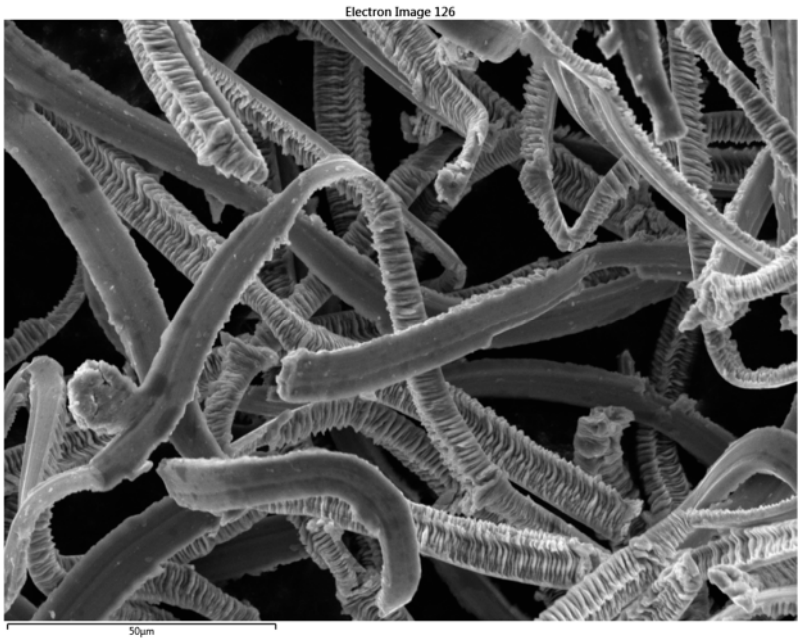

Figure 5.2.L. Ti-30Nb cutting chips under SEM imaging.

When viewed from a side angle this periodic roughness appears similar to that of a saw tooth pattern, which has been observed commonly in the machining of Titanium alloys through many different methods, particularly in turning processes. This phenomenon is referred to as shear band deformation and are a result of compressive stress on the alloy as it is removed from the substrate.

5.3 Contact Angles

Contact angle data was collected for only the structured surfaces on the Ti-30Nb alloy. Both alloys were measured to determine the surface free energy.

5.3.1 Groove Direction Perpendicular to the line of site

Perpendicular data for the contact angle and droplet volumes for each square over both the grooved and flat surfaces can be seen in Table 5.3.A and Table 5.3.B. These contact angles across all squares gave a mean contact angle of 32.81 ± 6.91° for the grooved surfaces and 24.93 ± 4.39° for the flat surfaces.

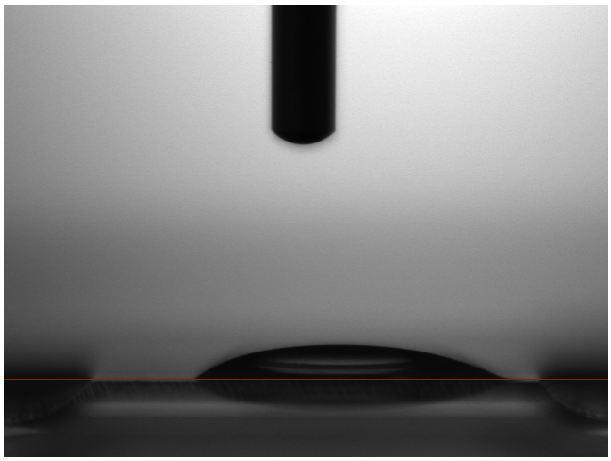

Figure 5.3.A. Image of water droplet on grooved surface of square 1, imaged from a line of sight perpendicular to the direction of grooves.

Table 5.3.A. Contact angle measurements taken on machined grooves, imaged from a line of sight perpendicular to the direction of grooves.

Square	Mean Contact Angle (°)	standard deviation	Droplet Volume (µL)	standard deviation
1	31.44	2.35	1.731	0.137
2	42.66	0.62	1.148	0.029
3	31.94	2.50	1.344	0.224
4	41.93	0.75	1.083	0.031
5	36.40	1.35	1.279	0.056
6	34.65	0.75	1.345	0.032
7	26.92	0.72	1.073	0.033
8	27.47	0.77	1.012	0.036
9	21.88	0.64	0.923	0.045

Table 5.3.B. Contact angle measurements taken on flat machined surface, imaged from a line of sight perpendicular to the direction of tool feed in machining.

Square	Mean Contact Angle (°)	standard deviation	Droplet Volume (µL)	standard deviation
1	22.51	4.16	0.695	0.038
2	29.06	1.81	3.221	1.303
3	31.72	0.66	0.901	0.022
4	27.29	0.85	0.801	0.030
5	23.28	1.04	0.792	0.224
6	20.17	0.33	1.470	0.031
7	17.97	0.44	1.090	0.060
8	25.80	0.52	0.780	0.019
9	26.58	1.57	1.342	0.196

This presents an average contact angle difference of 7.88° between the grooves and flat surfaces where the groove structures exhibit the higher hydrophobicity, as to be expected.

The exception to this observation occurs on square 9 from this perspective, where the contact angle for the flat machined surface in 4.70° higher on the flat surface than the grooved of the same square. This could be potentially the result of the 1.99 tool radius step over in the machining of this surface, which generated large structures between each pass of the end mill between 5 and 15 microns in height. These unintentional structures, shown in Figure 5.3.B, greatly increase the surface roughness of the flat surface, which would in turn increase the hydrophobicity.

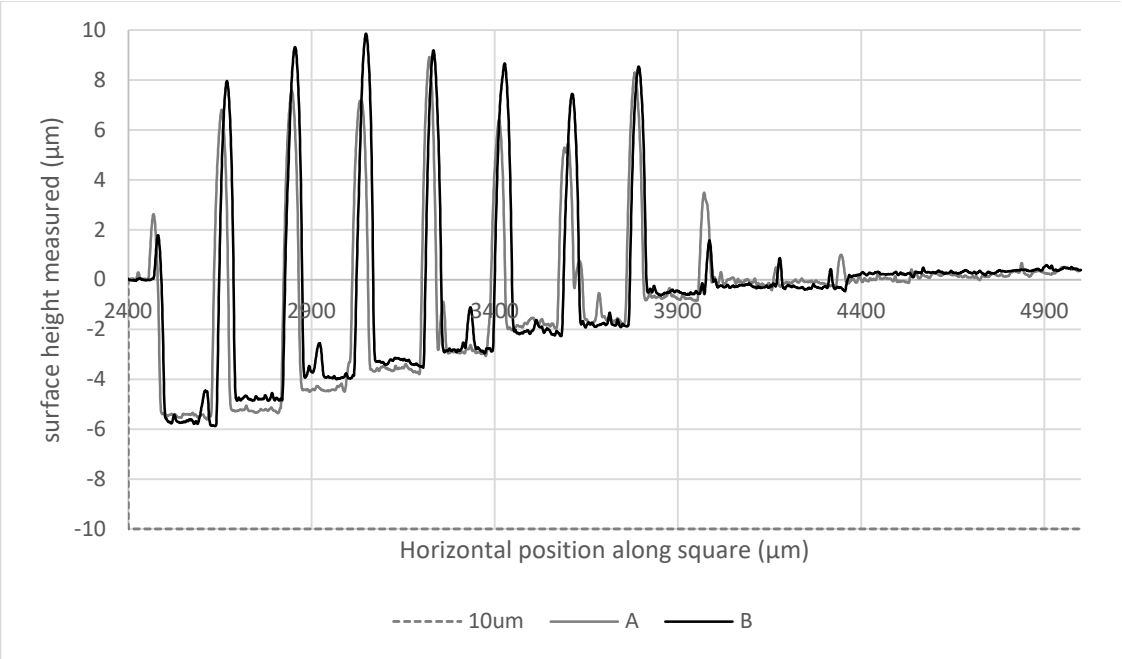

Figure 5.3.B. Surface profile of the flat machined surface on square 9, showing tall structures generated between tool passes as a result of there being no tool overlap with each pass of the end mill.

5.3.2 Groove Direction Parallel to the line of site

Parallel data for the contact angle and droplet volumes for each square over both the grooved and flat surfaces can be seen in Table 5.3.A and Table 5.3.B. These contact angles across all squares gave a mean contact angle of 42.47 ± 19.38° for the grooved surfaces and 29.42 ± 16.82° for the flat surfaces.

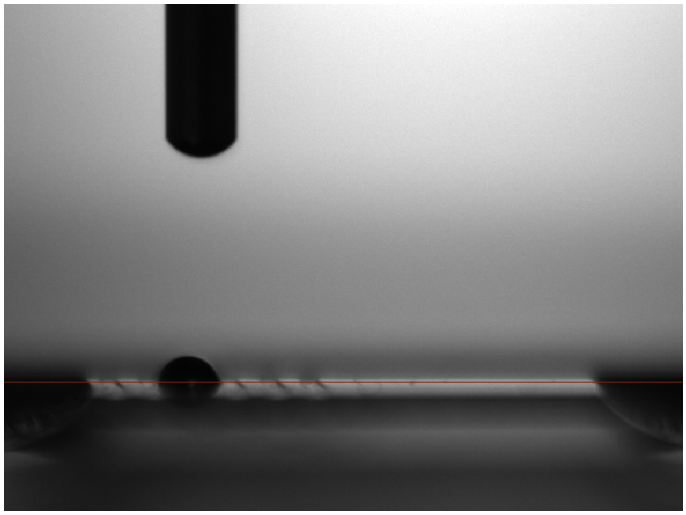

Figure 5.3.C. Image of water droplet on grooved surface of square 1, imaged from a line of sight parallel to the direction of grooves.

Table 5.3.C. Contact angle measurements taken on machined grooves, imaged from a line of sight parallel to the direction of grooves.

Square	Mean Contact Angle (°)	standard deviation	Droplet Volume (µL)	standard deviation
1	83.85	8.53	0.055	0.017
2	46.84	6.89	0.133	0.016
3	40.43	17.86	0.213	1.137
4	43.36	9.27	`0.060	0.017
5	30.19	5.89	0.056	0.011
6	25.76	21.45	0.195	1.040
7	19.53	2.81	0.032	0.008
8	58.06	15.96	0.098	0.011
9	34.19	2.74	0.110	0.013

Table 5.3.D. Contact angle measurements taken on flat machined surface, imaged from a line of sight parallel to the direction of tool feed in machining.

Square	Mean Contact Angle (°)	standard deviation	Droplet Volume (µL)	standard deviation
1	21.56	2.22	0.165	0.013
2	20.79	1.88	0.183	0.013
3	20.54	1.29	0.227	0.013
4	11.83	1.02	0.082	0.012
5	28.01	1.84	0.101	0.008
6	21.52	1.33	0.253	0.018
7	24.33	14.81	0.325	0.171
8	56.24	4.08	0.179	0.010
9	59.93	2.84	0.105	0.021

When viewed from this angle, the difference in angle is a much greater value of 13.05°, but once again the grooved surfaces prove to provide the higher level of hydrophobicity. Standard deviation of the angle values were much greater and depended heavily on whether or not the water droplet was able to break past the barriers of the features on the surface. With the period being a comparable size to the water droplet in some cases, as in Figure 5.3.C where the droplet remained only as wide as 1.5 groove periods (approximately 600µm), if the droplet did break past the barrier as these feature edges then it would rapidly spread until met by the next significant feature. This meant that for the same surface the drop could occasionally hold a small width and a high contact angle but then suddenly spread much wider, resulting in a lower angle as seen for square 7 as an example.

For the images taken from this perspective there are more anomalies where the flat surface appears to have a higher level of hydrophobicity than the grooves. Again as with the previous view square 9 has a significantly higher contact angle on the flat surface, but this also occurs for square 7, where the grooves contact angle is abnormally low, and in square 8 where the flat surface appears unusually high at 56.24°, less than 2° lower than for the groove structures. For squares 7 and 8 there is less obvious reasoning for this occurring than previously explained with square 9 from the data collected. Further geometric features not observed in the data could be the reason for these adjustments in hydrophobicity, or

potentially the initial interaction between the water droplet and the surface induced a higher level of wetting than expected from external energy input being too high.

6 DISCUSSION

6.1 Accuracy of Manufacture

This project experienced many issues with inaccuracy in the manufacture of the features designed across all trials tested.

The first of which presented itself as the machining began with the alignment of the milling tool in the KERN EVO. Although the inbuilt CMM probe was used to determine a zero point in the z direction on the surface as a reference for all depths of cuts to be made from, there was some level of error in either this measurement or the measured tool length that resulted in no contact being made when the programs were run. The tool had to be lowered in increments to determine the first point of contact after the Z offset calibration which meant that the targeted depth of cut on the flat and the depth of grooves was not accurate to what was desired. Typically this misalignment was at first between 10μm and 20μm and after this gap was closed a final error of less than 10μm was observed on the depths in machining.

Secondly the flat surface machining occurring with a gradually declining depth of cut caused large inaccuracies to the target geometry, which was expected to be a horizontal surface with an even depth across. It is unsure what the cause for these observations was, however a likely factor could be the machines calibration and alignment as it has not been frequently used and calibrated with the CMM probe for a long period prior to use. It could be worth repeating similar geometrical tests after a full calibration of the entire system to determine if these same issues are observed.

Another factor affect the accuracy of geometry was the tools diameters, which were measured to be lower than expected from the specification. This could be adjusted for by measuring each tool individually and then taking each tools true diameter into account, repeating a secondary pass with a small step over of the tool to fill the full 200μm target. These would all be serious factors in the fabrication of structured surfaces where geometrical accuracy is of high importance.

6.2 Machining Outcomes

Force measurements performed in the machining of these features were not reported on in this thesis as the data acquired had an extremely high signal to noise ratio. It is possible that for cuts as small as those performed, the forces are either too low to be noticeable by the background noise of the machine such as the spindle, whose bearings are likely a source of vibration, or that the Kistler MiniDyn was not capable of distinguishing forces of such a small level from other signals from the machine. If to be repeated in an attempt to acquire force data it would be sensible to either measure using a more sensitive dynamometer capable of picking up smaller forces, although due to the high noise observed this is unlikely to improve the results. Alternatively performing force measurements on a run of the program when the alloy is not in contact with the tool could provide a base level of noise and expected forces from machine movement in the program that would allow for noise filtering and comparison between when the alloy is being machined and when it isn't.

Surface roughness measured in the groove bottoms was found to be as less than 1μm Ra for all samples, with the minimum values being below 0.2μm Ra. This presents a high level of surface quality within the grooves even though the form of the groove was not ideal due to alignment issues, tool geometry and the formation of burrs. The Taguchi method determined that for the highest level of surface quality it is better to use a low spindle speed and low feedrate with a depth of cut around 10μm being optimum. Although the low feed rate results in a drastic increase in machining time which could be very important to be used for manufacturing of multiple textured surfaces. Burr formation also appears to have a strong correlation to material removal rate, controlled by the feedrate and depth of cut. Again lowering these too factors also increases the machining times so for reasonable manufacture speed a trade of would need to be made between part quality and accuracy and machining time desired.

Tool wear was observed in a minimal amount through this project although from the images observed it appears that the most significant factor in any wear present was a result of built up edge. It's possible that if machining times were

extended so that the tools were used until a higher degree of wear occurred that the adhering of workpiece material would be the highest contributor to the wearing of the tool. Although the surface analysis showed high levels of Carbon on the surface it seems unlikely that diffusion is an active contributor due to the good condition the tools remained in. It is possible that this Carbon an Oxygen that was deposited on the surface came from atmospheric reactions with workpiece in process. This would depend on machining temperatures reached and would require further investigation to confirm that diffusion is not the reason for these Carbon deposits.

6.3 Surface Functionality

The contact angle measurements did show that the structured surface granted an increase in hydrophobicity to some degree, although it wasn't completely consistent. The increase of hydrophobicity was only a minor improvement in most cases, this is likely due to the relatively large features that were fabricated due to 200µm diameter tools being the smallest available at the time of the project. Typically in literature the sizes of hydrophobic features manufactured and test are on the scale of 50µm or less, with some even being below 1µm per feature. If smaller tools would have been available then it would have been possible to test smaller feature sizes for hydrophobicity, but this would have also resulted in machining times being drastically large for the same area of machining and would have given further difficulties with the alignment of the tool and machine.

6.4 Conclusions

In the optimum machining of Ti-30Nb in terms of surface finish it is better to use a minimal material removal rate, especially taking into consideration a lower feed rate over a lower depth of cut. If high quality is desired then this will also result in long machining times as a result so this much be considered when determining process parameters. In terms of tool wear the optimum parameters could not be determined as wear of the micromilling tools was not observed at a high enough level to perform quantitative analysis.

Micromilling can be used as a process to create functional surfaces when using Tungsten carbide tools. Although possible to manufacture successfully, it would not be recommended for micron scale features due to long machining times and limited accuracy in the process. For applications such as hydrophobicity it is more time effective to use laser sintering methods to texture the surface. Laser technologies would not grant the same degree of geometrical accuracy due to variations in the melt pool of the laser but for hydrophobicity this is not so important and the induced surface roughness will still grant anti-wetting properties on Titanium alloys. Micromilling could be a more valuable method in the texture of millimetre scale features onto a surface. In this scale the accuracy and machining times will be more preferable against other methods depending on the surface geometries desired.

From the experiments performed it seems that the beta titanium alloy Ti-30Nb is machinable to a reasonable degree through micromilling as minimal tool wear was observed over all samples. It is possible that through more extended periods of machining this could not hold true though as the volumes removed in these trials was extremely small compared to what a tool would be expected to machine in an industrial setting.

6.5 Recommendations for Future Work

To further determine the machinability of Ti-30Nb alloy through micromilling it could be suggested that the alloy is machined for longer durations until critical failure is observed in the tools or significant and measurable wear volumes have been observed on the end mills. This would grant greater insight into how viable the process is in industry from an economic perspective rather than a component accuracy perspective. Arguably the degree of accuracy desired could be confirmed once the cost effectiveness of the process has been better investigated to optimised manufacture for both expense and quality.

Further completion of this work could be performed to validate any data acquired and presented here. Due to time and equipment limitations, not all of the measurements that were hoped for could be completed. This may be apparent from the lack of data presented from measuring the Ti-6Al-4V sample. Having the

same analysis performed on the Ti-6Al-4V sample and comparing data against the Ti-30Nb alloy would better determine if the alloy a potential replacement by providing a quantitative comparison on how cost effective and successful the same process is on each alloy. Also further measurements could be taken on the Ti-30Nb sample. Confocal microscopy was planned to be performed for surface topography measurements as well and contact profilometry using a Talysurf touch probe of a smaller probe tip than that available on the Dektak, but this equipment was not functional at the time measurements were being taken so this was not possible. Further measurements on these equipment would allow for more reliable and accurate data.

Microstructural changes during the machining process of beta titanium alloys would be a greatly beneficial direction to take this research as to date there is very little data present on how well the BCC microstructure of beta titanium alloys remains when exposed to the high stress of machining processes. It could possibly revert back to a HCP structure like pure Titanium or possibly maintain its BCC structure, and as a result it’s preferential mechanical properties.

7 REFERENCES

Agrawal, A., Goel, S., Rashid, W., & Price, M. (2015). Prediction of Surface Roughness During Hard Turning of AISI 4340 Steel (69 HRC). *Applied Soft Computing, 30*(1), 279-286.

Arthritis Research UK. (n.d.). *Musculoskeletal Calculator*. Retrieved April 18, 2017, from https://www.arthritisresearchuk.org/arthritis-information/data-and-statistics/musculoskeletal-calculator/analysis.aspx?ConditionType=1,2,3,4&ChartType=2&Region-0=all&AgeBracket=2,3,4#

Arthritis Research UK. (n.d.). *Musculoskeletal Calculator*. Retrieved April 18, 2017, from https://www.arthritisresearchuk.org/arthritis-information/data-and-statistics/musculoskeletal-calculator/analysis.aspx?ConditionType=1,2,3,4&ChartType=2&Region-0=all&AgeBracket=2,3,4#

Attanasio, A., Gelfi, M., Ceretti, E., & Giardini, C. (2013). Influence of MAterial Microstructures in Micromilling of Ti6Al4V Alloy. *Materials, 6*, 4268-4283.

Bajpai, V., Kushwaha, a., & Singh, R. (2013). Burr Formation and Surface Quality in High Speed Micromilling of Titanium Alloy (Ti6Al4V). *ASME 2013 International Manufacturing Science and Engineering Conference collocated with the 41st North American Manufacturing Research Conference*.

Barthlott, W., & Neinhuis, C. (1997). Purity of the Sacred Lotus, or Escape from the Contamination in Biological Surfaces. *Planta, 202*(1), 1-8.

Berkovich Tip. (n.d.). Retrieved from Wikipedia: https://en.wikipedia.org/wiki/Berkovich_tip

Bico, J., Marzolin, C., & Quere, D. (1999). Pearl Drops. *Europhysics Letters, 47*(2), 220-226.

Brodner, W., Bitzan, P., Lomoschitz, F., Krepler, P., Jankovsky, R., Lehr, S., . . . Gottsauuner-Wolf, F. (2004). Cahnges in Bone Mineral Density in the Proximal Femur After Cementless Total Hip Arthroplasty: A Five Year Logitudinal Study. *The Journal of Bone & Joint Surgery, 86-B*(1), 20-26.

Bruzzone, A., Costa, H., Lonardo, P., & Lucca, D. (2008). Advances in Engineered Surfaces for Functional Performance. *CIRP Annals - Manufacturing Technology*, 57.

Cantero, J., Tardio, M., Canteli, J., Marcos, M., & Miguelez, M. (2005). Dry Drilling of Alloy Ti-6Al-4V. *International Journal of Machine Tools & Manufacture, 45*(11), 1249-1255.

Cassie, A., & Baxter, S. (1944). Wettability of Porous Surfaces. *Transactions of the Faraday Society, 40*, 546-551.

Collings, E. (1984). The Physical Metallurgy of Titanium Alloys, ASM Series in Metal Processing. *American Society for Metals*.

Dahotre, N., Paital, S., Samant, A., & Daniel, C. (2010). Wetting Behaviour of Laser Synthetic Surface Microtextures on Ti-6Al-4V for Bioapplication. *Philosophicalk Transactions of the Royal Society: A, 368*(1917), 1863-1889.

Dandekar, C., Shin, Y., & Barnes, J. (2010). Machinability Improvement of Titanium Alloys (Ti-6Al-4V) via LAM and Hybrid Machining. *International Journal of Machine Tools & Manufacture, 50*(2), 174-182.

Dearnley, P., & Grearson, A. (1986). Evaluation of Principal Wear Mechanisms of Cemented Carbide and Ceramics used for Machining Titanium Alloy IMI 318. *Material Science and Technology, 2*(1), 47-58.

Deligianni, D., Katsala, N., Ladas, S., Sotiropoulou, D., Amedee, J., & Missirlis, Y. (2001). Effect of Surface Roughness of the Titanium Alloy Ti-6Al-4V on Human Bone Marrow Cell Response and on Protein Adsorprtion. *Biomaterials, 22*(11), 1241-1251.

Ding, H., Shen, N., & Shin, Y. (2012). Thermal and Mechanical Modelign Analysis of Laser-Assisted Micro-milling of Difficult-to-Machine Alloys. *Journal of Materials Processing Technology, 212*(3), 301-313.

Durazo-Cardenas, I., Shore, P., Luo, X., Jacklin, T., Impey, S., & Cox, A. (2007). 3D Characterisation of Tool Wear Whilst Diamond Turning Silicon. *Wear, 262*, 340-349.

Elias, C., Oshida, Y., Lima, J., & Muller, C. (2007). Relationship Between Surfaces Properties (Roughness, Wettability and Morphology) of Titanium and Dental Implant Removal Torque. *Journal of the mechanical behaviour of biomedical materials, 12*(2), 234-242.

Engh, C., Bobyn, J., & Glassman, A. (1987). Porous-Coated Hip Replacement. *The Bone & Joint Journal, 69*(1), 45-55.

Fai, C., Zhongchen, C., & Ting, H. (2017). An Investigation of Surface Generation in Swing Precess Bonnet Polishing of 3D-Structured Surfaces Processing High Wettability. *Euspen's 17th International Conference & Exhibition Proceedings*, 213-214.

Fischer-Cripps, A. (2009). The IBIS Handbook of Indentation. *Fischer-Cripps Laboratories Pty Ltd*.

Gupta, K., & Laubscher, R. (2016). Sustainable Machining of Titanium Alloys: A Critical Review. *Proceedings of the Institution of Mechanical Engineers Part B Journal of Engineering Manufacture*.

Huiskes, R., Weinans, H., & Reitbergen, B. (1992). The Relationship Between Stress Sheilding and Bone Resorption Around Total Hip Stems and the Effects of Flexible Materials. *Clinical Orthopaedics and Related Research, 274*, 124-134.

Jasinevicius, R. (2007). Surface Integrity of Ultra-Precision Diamond Turned Ti (Comercially Pure) and Ti alloy (Ti6Al4V). *Proceedings of the Institution of Mechanical Engineers Part B Journal of Engineering Manufacture, 221*(6), 999-1006.

Jawaid, A., Sharif, S., & Koksal, S. (2000). Evaluation of Wear Mechanisms of Coated Carbide Tools When Face Milling Titanium Alloy. *Journal of Materials Processing Technology, 99*(1-3), 266-274.

Kahles, J., Field, M., Eylon, D., & Froes, F. (1985). Machining of Titanium Alloys. *Journal of Metals, 37*(4), 27-35.

Kahles, J., Field, M., Eylon, D., & Froes, P. (1985). Machining of Titanium Alloys. *Journal of Metals*, 27-35.

Kamperman, M., Kroner, E., Campo, A., McMeeking, R., & Arzt, E. (2010). Functional Adhesive Surfaces with "Gecko" Effect: The Concept of Contact Splitting. *Advanced Engineering Materials , 12*(5), 333-422.

Kent, D., Wang, G., & Dargusch, M. (2010). Psedoelastic Behaviour of a β Ti-25Nb-3Zr-3Mo-2Sn Alloy. *Materials Science and Engineering: A, 527*(9), 2246-2252.

Konig, W., Fritsch, R., & Kammermeier, D. (1991). Physically Vapor Deposited Coatings on Tools: Performance and Wear Phenomena. *Surface and Coatings Technology, 49*(1-3), 316-324.

Li, A., Zhao, J., Luo, H., & Pei, Z. (2012). Progressive Tool Failure in High-Speed Dry Milling of Ti-6Al-4V Alloy with Coated Carbide Tools. *The International Journal of Advanced Manufacturing Technology, 58*(5-8), 465-478.

Li, R., Riester, L., Watkins, T., Blau, P., & Shih, A. (2008). Metallurgical Analysis and Nanoindentation Characterization of Ti-6Al-4V Workpiece and Chips in High-Throughput Drilling. *Materials Science and Engineering: A, 472*(1-2), 115-124.

Liu, Y., Chen, X., & Xin, J. (2008). Hydrophobic Dick Feathers and Their Simulation on Textile Substrates for Water Repellent Treatment. *Bioinspiration & Biomitrics, 3*(4), 1-8.

Long, M., & Rack, H. (1998). Titanium Alloys in Total Joint Replacement - A Material Science Perspective. *Biomaterials, 19*(18), 1621-1639.

Machado, A., & Wallbank, J. (1990). Machining of Titanium and its Alloys - A Review. *Part B: Journal of Engineering Manufacture, 204*, 53-60.

Magin, C., Cooper, S., & Brennan, A. (2010). Non-toxic Antifouling Strategies. *Materials Today, 13*(4), 36-44.

Malshe, A., Rajurkar, K., Samant, A., Hansen, H., Bapat, S., & Jiang, W. (2013). Bio-inspired Functional Surfaces for Advanced Applications. *CIRP Annals - Manufacturing Technology, 62*(2), 607-628.

Mamalis, A., Ramsdem, J., Grabchenko, A., Lytvynov, L., Filipenko, V., & Lavrynenko, S. (2006). A Novel Concept for the Manufacture of Individual Sapphire-Metallic Hip Joint Endoprosthesis. *Journal of Biological Physics and Chemistry, 6*(1), 113-117.

Margolin, H., & Farrar, P. (1969). The Physical Metallurgy of Titanium Alloys. *Ocean Engineering, 1*(3), 329-345.

McCarthy, C., Steinberg, G., Agren, M., Leahey, D., Wyman, E., & Baran, D. (1991). Quantifying Bone Loss From the Proximal Femur After Total Hip Arthroplasty. *The journal of bone and joint surgery, 73-B*(5), 774-778.

Muhammad, R., Hussain, M., Maurotto, A., Siemers, C., Roy, A., & Silberschmidt, V. (2014). Analysis of a free Machining alpha-beta Titanium Alloys Using Conventional and Ultrasonically Assisted Turning. *Journals of Materials Processing Technology, 214*, 906-915.

Narutaki, N., & Murakoshi, A. (1983). Study on Machining of Titanium Alloys. *CIRP Annals, 32*(1), 65-69.

Narutaki, N., Murakoshi, A., Motonishi, S., & Takeyama, H. (1983). Study on Machining of Titanium Alloys. *CIRP Annals - Manufacturing Technology, 32*(1), 65-69.

NHS. (2016). *Osteoarthritis*. Retrieved April 18, 2017, from http://www.nhs.uk/conditions/osteoarthritis/Pages/Introduction.aspx

NHS. (2016). *Osteoporosis* . Retrieved May 1, 2017, from http://www.nhs.uk/conditions/Osteoporosis/Pages/Introduction.aspx

NICE. (2014). Total Hip Replacement and Resurfacing Arthroplasty for End-stage Arthritis of the Hip. *National Institute for Health and Care Excellence Guidance*, 1-60.

Nishino, K. (2003). Super Multifunctional Alloy "GUM METAL". *R&D Review of Toyota CRDL, 38*(3), 50.

NJR. (2014). *National Joint Registry - Joint Replacement Statistics*. Retrieved April 18, 2017, from http://www.njrcentre.org.uk/njrcentre/Patients/Jointreplacementstatistics

Oliver, M., & Pharr, G. (1992). An Improved Technique for Determining Hardness and Elastic Modulus Using Load Displacement Sensing Indentation Experiments. *Journal of Materials Research, 7*(6), 1564-1583.

Ozel, T., Thepsonthi, T., Ulutan, D., & Kaftanoglu, B. (2011). Experimental and Finite Element Simulation on Micro-milling of Ti-6Al-4V Alloy with Uncoated and cBN Coated Micro-tools. *CIRP Annals - Manufacturing Technology, 60*, 85-88.

Ozel, T., Thepsonthi, T., Ulutan, D., & Kaftanoglu, B. (2011). Experiments and Finite Element Simulations on Micro-milling of Ti-6Al-4V Alloy with Uncoated and CBN Coated Micro-tools. *CIRPS Annals, 60*(1), 85-88.

Park, J., Scwartz, Z., Olivares-Navarrete, R., Boyan, B., & Tannenbaum, R. (2011). Enhancement of Surface Wettability via the Modification of Microtextured Titanium Implant Surfaces with Polyelectrolytes. *Langmuir, 27*(10), 5976-5985.

Perry, T., Werschmoeller, D., Li, X., Pfefferkorn, F., & Duffie, N. (2009). Pulsed Laser Polsihing of Micro-milled Ti6Al4V Samples. *Journal of Manufacturing Processes, 11*(2), 74-81.

Ponsonnet, L., Reybier, K., Jaffrezic, N., Comte, V., Lagneau, C., Lissac, M., & Martlet, C. (2003). Relationship Between Surface Properties (Roughness, Wettability) of Titanium and Titanium Alloys and Cell Behaviour. *Materials Science and Engineering: C, 23*(4), 551-560.

Rashid, R., Sun, S., Wang, G., & Dargusch, M. (2011). Machinability of a Near Beta Titanium Alloy. *Proceedings of the Institution of Mechanical Engineers, Part B: Journal of Engineering Manufacture*, 2151-2162.

Rashid, R., Sun, S., Wang, G., & Dargusch, M. (2012). An Investigation of Cutting Forces and Cutting Temperatures During Laser-Assisted Machining of the Ti-6Cr-5Mo-5V-4Al Beta Titanium Alloy. *International Journal of Machine Tools and Manufacture, 63*(1), 58-69.

Rashid, R., Sun, S., Wang, G., & Dargusch, M. (2012). The Effect of Laser Power on the Machinability of the Ti-6Cr-5Mo-5V-4Al Beta Titanium Alloy During Laser Assisted Machining. *International Journal of Machine Tools and Manufacture, 63*(1), 41-43.

Rupp, F., Scheideler, L., Rehbein, D., Axmann, D., & Geis-Gerstorfer, J. (2004). Roughness induced Dyanamic Changes of Wettability of Acid Etched Titanium Implant Modifications. *Biomaterials , 25*(7-8), 1429-1438.

Shelton, J., & Shin, Y. (2010). Comparative Evaluation of Laser-Assisted Micro-milling for AISI 316, AISI 422, Ti-6Al-4V and Iconel 718 in a side-cutting configuration. *Journal of Micromechanics and Microengineering, 20*(7), 1-12.

Shirtcliffe, N., McHale, G., Arterton, S., & Newton, M. (2010). An Introduction to Superhydrophobicity. *Advances in Colloid and Interface Science, 161*(1-2), 124-138.

Spear, H., & Dismuhes, J. (1994). Synthetic Diamond: Emerging CVD Science and Technology. *Electrochemical Society*.

Su, Y., He, N., Li, L., & Li, X. (2006). An Experimental Investigation of Effects of Cooling/Lubrication Conditions on Tool Wear in High-Speed End Milling of Ti-6Al-4V. *Wear, 261*(7-8), 760-766.

Sun, J., & Guo, Y. (2009). A Comprehensive Experimental Study on Surface Integrity by End Milling Ti-6Al-4V. *Journal of Materials Processing Technology, 209*(8), 4036-4042.

Thepsonthi, T., & Ozel, T. (2012). Multi-objective Process Optimization for Micro-end Milling of Ti-6Al-4V Titanium Alloy. *The International Journal of Advanced Manufacturing Technology, 63*(9-12), 903-914.

Thepsonthi, T., & Ozel, T. (2013). Experimental and Finite Element Simulation Based Investigations on Micro-milling Ti-6Al-4V Titanium Alloy: Effects of cBN Coating on Tool Wear. *Journal of Materials Processing Technology, 213*(4), 532-542.

Wang, J., Chen, H., Sui, T., Li, A., & Chen, D. (2009). Investigation on Hydrophobicity of Lotus Leaf: Experiement and Theory. *Plant Science, 176*(5), 687-695.

Wang, K. (1996). The Use of Titanium for Medical Applications in the USA. *Materials Science and Engineering: A, 213*(1-2), 134-137.

Wenzel, R. (1936). Restistance of Solid Surfaces to Wetting by Water. *Industrial & Engineering Chemistry, 28*(8), 988-994.

Xi, Y., Zhan, H., Rashid, R., Wang, G., Sun, S., & Dargusch, M. (2014). Numerical Modeling of LAser Assisted Machining of a Beta Titanium Alloy. *Computational Materials Science, 92*(1), 149-156.

Zhang, L., Kiat, E., & Pramanik, A. (2009). A Briefing on the Manufacture of Hip Joint Prosthesis. *Advanced Materials Research, 76-78*(1), 212-216.

Zhang, S., Li, J., & Jiang, F. (2010). Tool Wear and Cutting Forces Variation in High-Speed End-Milling Ti-6Al-4V Alloy. *The International Journal of Advanced Manufacturing Technology, 46*(1-4), 69-78.

Appendix A X-Ray Diffraction

The pre-machined Ti-30Nb sample showed peaks at around angles of 39°, 51°, 56°, 70° and 79° from the XRD measurements. This showed on the database to be representative of a body centred cubic sample of both Titanium and Niobium.

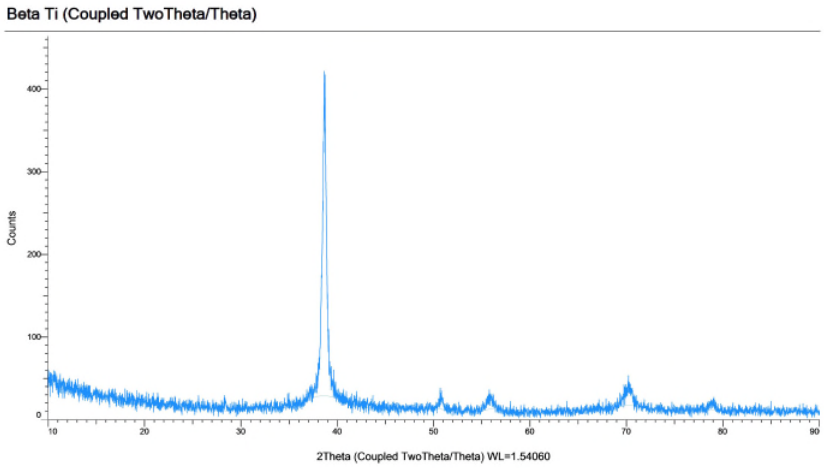

Figure A-A. XRD spectrum of pre-machined Ti-30Nb sample.

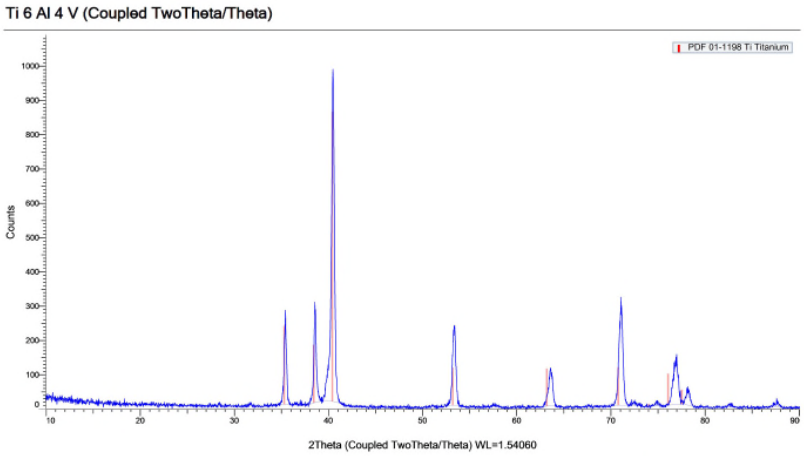

Figure A-B. XRD spectrum of pre-machined Ti-30Nb sample.

The pre-machined Ti-6Al-4V sample show peaks present as 35°, 38°, 40°, 53°, 64°, 71°, 77° and 78° with strong data base matches to close packed hexagonal Titanium.

Appendix B EDS Data

B.1 Pre-Machined Images

B.1.1 Ti-30Nb Alloy

Pre-machined EDS analysis of the Beta Titanium Alloy was performed to confirm that the metal being machined was Ti-30Nb.

Tabel_Apx B-A. Table of pre-machined EDS data of Ti-30Nb.

Image number	Percentage by Weight (%)	
	Ti	Nb
1	72.78	27.22
2	72.60	27.40
3	73.30	26.70

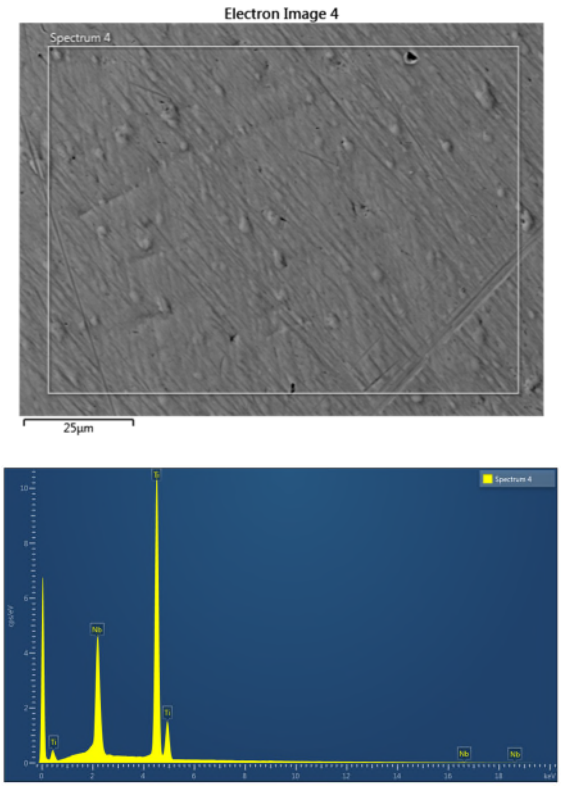

Figure B-A. Image 1 of pre-machined Ti-30Nb surface with EDS spectrum.

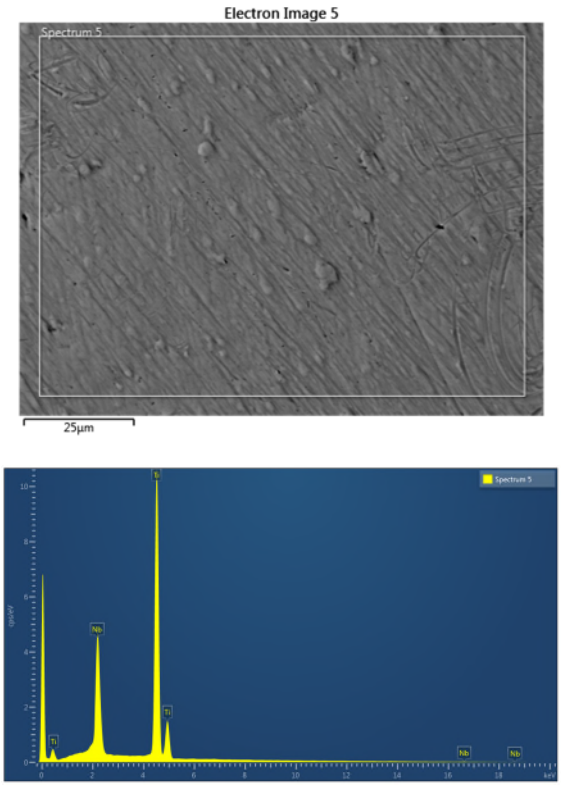

Figure B-B. Image 2 of pre-machined Ti-30Nb surface with EDS spectrum.

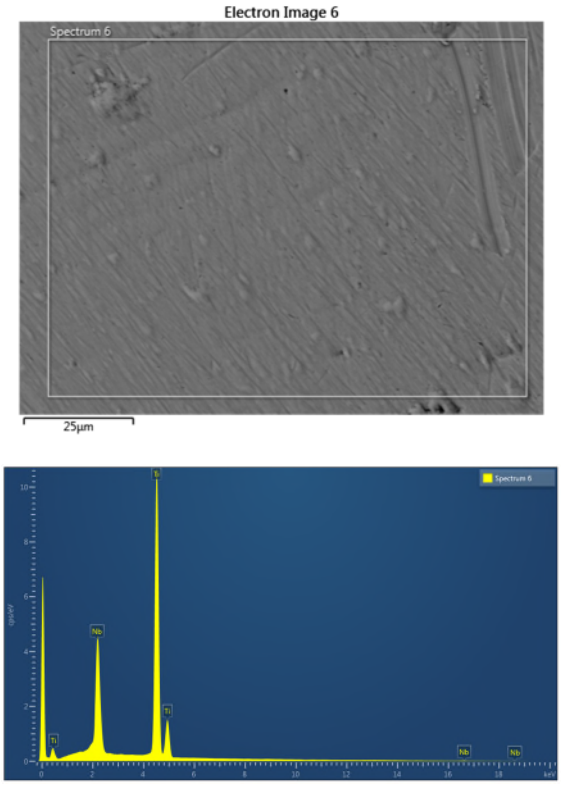

Figure B-C. Image 2 of pre-machined Ti-30Nb surface with EDS spectrum.

B.1.2 Ti6Al42V Alloy

Pre-machined EDS analysis of the alpha-beta Titanium Alloy was performed to confirm that the metal being machined was Ti-6Al-4V

Tabel_Apx B-B. Table of pre-machined EDS data of Ti-6Al-4V.

Image number	Percentage by Weight (%)		
	Ti	Al	V
1	90.02	5.71	4.27
2	89.98	5.69	4.34
3	90.23	5.68	4.09

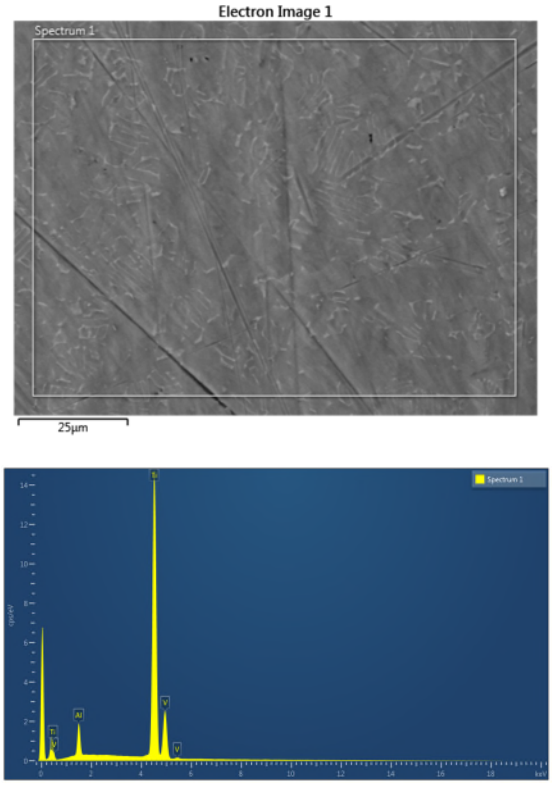

Figure B-D. Image 1 of pre-machined Ti-6Al-4V surface with EDS spectrum.

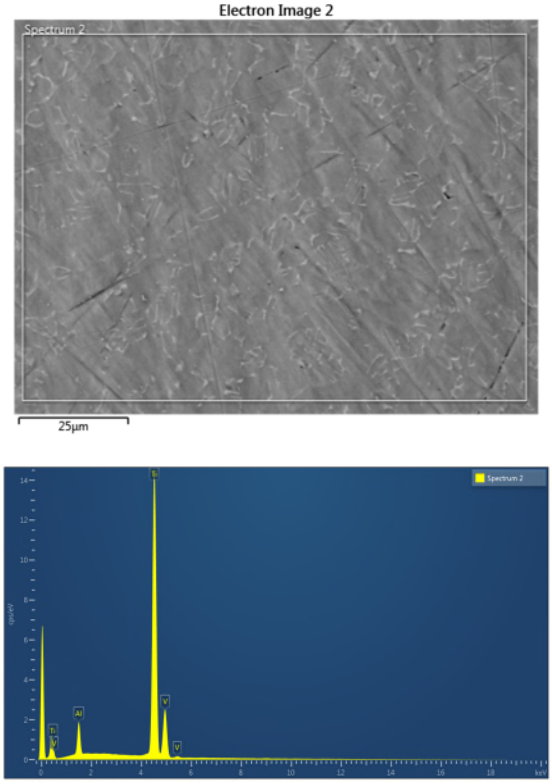

Figure B-E. Image 2 of pre-machined Ti-6Al-4V surface with EDS spectrum.

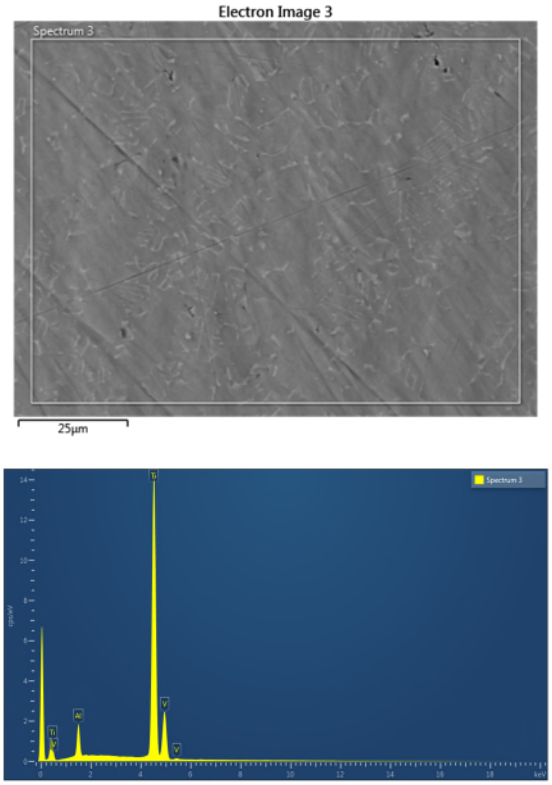

Figure B-F. Image 2 of pre-machined Ti-6Al-4V surface with EDS spectrum.

Appendix C Surface Free Energy of Alloys

Contact angle measurements to calculate the surface free energy were performed on the unmachined underside of each alloy using polarised water and unpolarised ethylene glycol. All values presented were calculated internally through the OneAttension software after a baseline and contact angle had been confirmed through measurement.

Tabel C-A. Properties of substances used in the surface free energy analysis from the OneAttension internal database.

Name	γtot [mN/m]	γd [mN/m]	γ+ [mN/m]	γ- [mN/m]	ρ [g/cm³]	η [mPa.s]	Temp. [°C]	Mol. weight [g/mol]
Air					0.0012		20	0.029
Water	72.8	21.8	25.5	25.5	0.998	1.002	20	18.01
Ethylene glycol	48	29	3	30.1	1.1132	16.1	20	62.07

C.1 Ti-30Nb Surface Free Energy

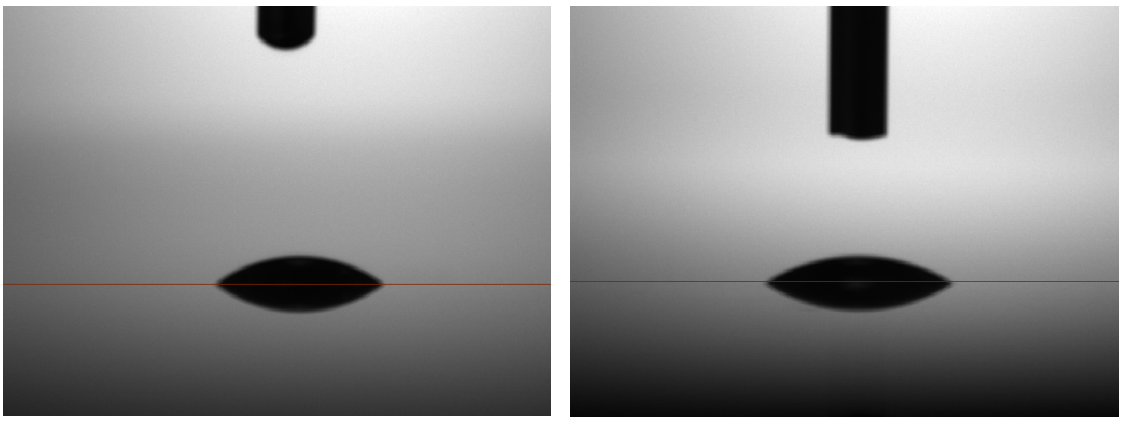

Figure C-A Ti-30Nb sample under contact angle testing. Left is testing with water and right is testing with ethylene glycol.

Tabel C-B. Results of Ti-30Nb alloy calculated from OneAttension Software for both Water and Ethylene Glycol measurements.

Measurement	θ [°]	γtot [mN/m]	γd [mN/m]	γ+ [mN/m]	γ- [mN/m]
Ti-30Nb - water	31.412	72.8	21.8	25.5	25.5
Ti-30Nb - ethylene glycol	36.456	48	29	3	30.1

Tabel C-C. Surface Tension Values for Ti-30Nb calculated through four different methods, presented by the OneAttension software.

Method	γtot [mN/m]	γd [mN/m]	γp [mN/m]
Equation of State	53.508	53.508	
OWRK/Fowkes	79.895	0.703	79.193
Wu	66.884	9.945	56.939
Zisman	146.794		

C.2 Ti-6Al-4V Surface Free Energy

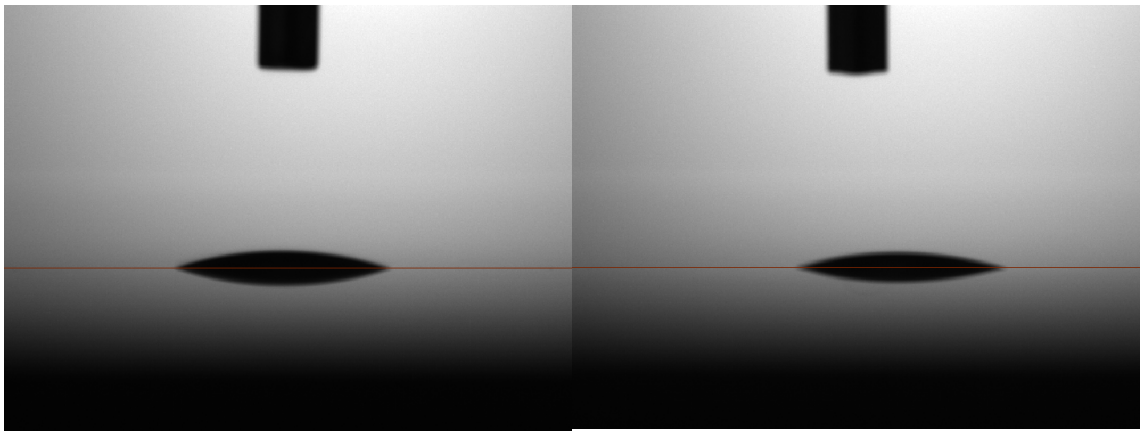

Figure C-B Ti-6Al-4V sample under contact angle testing. Left is testing with water and right is testing with ethylene glycol.

Tabel C-D. Results of Ti-6Al-4V alloy calculated from OneAttension Software for both Water and Ethylene Glycol measurements.

Measurement	θ [°]	γtot [mN/m]	γd [mN/m]	γ+ [mN/m]	γ- [mN/m]
Ti-6Al-4V - water	18.467	72.8	21.8	25.5	25.5
Ti-6Al-4V - ethylene glycol	18.789	48	29	3	30.1

Tabel C-E Surface Tension Values for Ti-6Al-4V calculated through four different methods, presented by the OneAttension software.

Method	γtot [mN/m]	γd [mN/m]	γp [mN/m]
Equation of State	109.36	109.36	
OWRK/Fowkes	83.678	1.831	81.848
Wu	71.786	13.061	58.725
Zisman	784.411		